AD-A163 053 THIN FILM TECHNOLOGY OF HIGH-CRITICAL-TEMPERATURE SUPERCONDUCTING ELECTRO (U) WESTINGHOUSE RESEARCH AND DEVELOPMENT CENTER PITTSBURGH PA J TALVACCHIO ET AL 1/2

UNCLASSIFIED 11 DEC 85 85-9C9-TUDEV-R1 N00014-82-C-0617 F/G 9/5 NL

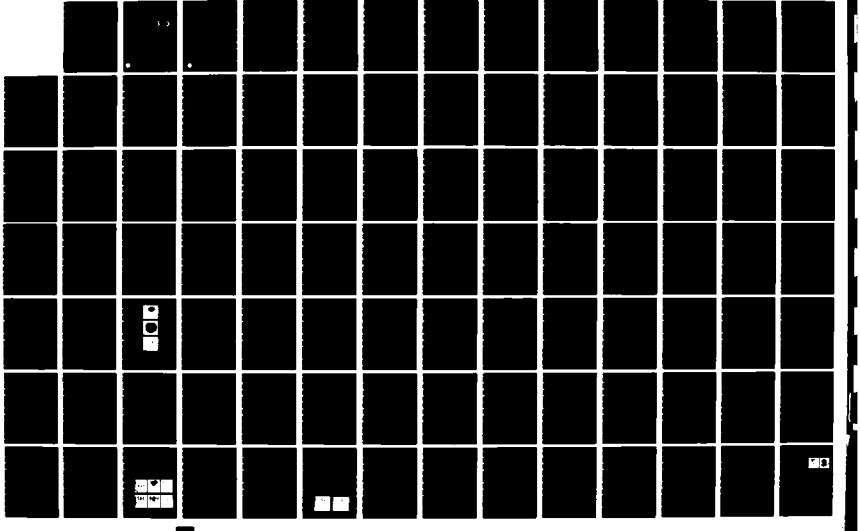

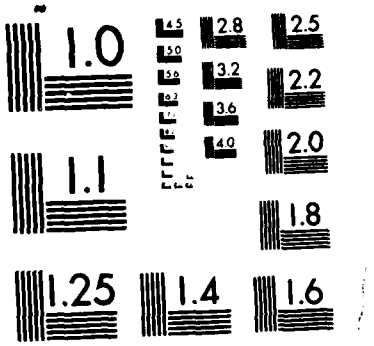

Final Report

12

THIN FILM TECHNOLOGY OF HIGH-CRITICAL-TEMPERATURE SUPERCONDUCTING ELECTRONICS

August 1, 1982 to September 30, 1985

By

J. Talvacchio, A. I. Braginski,
J. R. Gavaler and M. A. Janocko

Westinghouse Electric Corporation
Research and Development Center
Pittsburgh, Pennsylvania 15235

Office of Naval Research Contract No. N00014-82-C-0617

Final Report

THIN FILM TECHNOLOGY OF HIGH-CRITICAL-TEMPERATURE SUPERCONDUCTING ELECTRONICS

August 1, 1982 to September 30, 1985

By

J. Talvacchio, A. I. Braginski,
J. R. Gavaler and M. A. Janocko

Westinghouse Electric Corporation
Research and Development Center
Pittsburgh, Pennsylvania 15235

Office of Naval Research Contract No. N00014-82-C-0617

Westinghouse R&D Center
1310 Beulah Road
Pittsburgh, Pennsylvania 15235

Unclassified
SECURITY CLASSIFICATION OF THIS PAGE

REPORT DOCUMENTATION PAGE

1a. REPORT SECURITY CLASSIFICATION	1b. RESTRICTIVE MARKINGS AD-A163 053
2a. SECURITY CLASSIFICATION AUTHORITY	3. DISTRIBUTION/AVAILABILITY OF REPORT
2b. DECLASSIFICATION/DOWNGRADING SCHEDULE	
4. PERFORMING ORGANIZATION REPORT NUMBER(S) 85-9C9-TUDEV-R1	5. MONITORING ORGANIZATION REPORT NUMBER(S)
6a. NAME OF PERFORMING ORGANIZATION Westinghouse Research and Development Center 6b. OFFICE SYMBOL (If applicable)	7a. NAME OF MONITORING ORGANIZATION DCASMA Pittsburgh
6c. ADDRESS (City, State and ZIP Code) 1310 Beulah Road Pittsburgh, Pennsylvania 15235	7b. ADDRESS (City, State and ZIP Code) 1626-S Federal Building 1000 Liberty Avenue Pittsburgh, PA 15222
8a. NAME OF FUNDING/SPONSORING ORGANIZATION Office of Naval Research 8b. OFFICE SYMBOL (If applicable)	9. PROCUREMENT INSTRUMENT IDENTIFICATION NUMBER
8c. ADDRESS (City, State and ZIP Code)	10. SOURCE OF FUNDING NOS. PROGRAM ELEMENT NO. / PROJECT NO. / TASK NO. / WORK UNIT NO.
11. TITLE (Include Security Classification) THIN FILM TECHNOLOGY OF HIGH-CRITICAL-TEMPERATURE SUPERCONDUCTING ELECTRONICS	
12. PERSONAL AUTHOR(S) Talvacchio, J.; Braginski, A. I.; Gavaler, J. R.; and Janocko, M. A.	
13a. TYPE OF REPORT Final 13b. TIME COVERED FROM 8-1-82 TO 9-30-85	14. DATE OF REPORT (Yr., Mo., Day) 851211 15. PAGE COUNT 149
16. SUPPLEMENTARY NOTATION	
17. COSATI CODES FIELD / GROUP / SUB. GR.	18. SUBJECT TERMS (Continue on reverse if necessary and identify by block number)

19. ABSTRACT (Continue on reverse if necessary and identify by block number)

The objective of this three-year program was to develop a technology of Josephson tunnel junctions capable of operating at temperatures above 10K. The superconducting electrode materials investigated were V_3Si, Nb_3Sn and Mo-Re. Tunnel barriers were formed mostly by oxidizing metallic overlayers of Al and Y. Superconductor/barrier interfaces were characterized by surface-analytical techniques. The results of characterization permitted fabricated of junctions with Nb_3Sn and Mo-Re base electrodes and Pb, Pb-Bi and Mo-Re counterelectrodes having nearly ideal current-voltage characteristics. These counterelectrodes were deposited at temperatures not exceeding T = 100°C. The Mo-Re counterelectrode formed at low T had a critical temperature, T_c, of only 8K. A high-critical-temperature Nb_3Sn counterelectrode requiring high deposition temperatures could not be fabricated successfully. The main cause of this negative result was the nonuniform coverage of the base with overlayers which contained thin or defective

20. DISTRIBUTION/AVAILABILITY OF ABSTRACT UNCLASSIFIED/UNLIMITED ☐ SAME AS RPT. ☐ DTIC USERS ☐	21. ABSTRACT SECURITY CLASSIFICATION
22a. NAME OF RESPONSIBLE INDIVIDUAL	22b. TELEPHONE NUMBER (Include Area Code) / 22c. OFFICE SYMBOL

DD FORM 1473, 83 APR EDITION OF 1 JAN 73 IS OBSOLETE.

Unclassified
SECURITY CLASSIFICATION OF THIS PAGE

spots. In contrast to Nb_3Sn, high-T_c NbN counterelectrodes were successfully fabricated and sumgap voltages exceeding 5 mV were measured at 4.2K. The report contains new information on artifical barriers and on Mo-Re and Nb_3Sn superconducting films.

TABLE OF CONTENTS

ABSTRACT

The objective of this three-year program was to develop a technology of Josephson tunnel junctions capable of operating at temperatures above 10K. The superconducting electrode materials investigated were V_3Si, Nb_3Sn and Mo-Re. Tunnel barriers were formed mostly by oxidizing metallic overlayers of Al and Y. Superconductor/barrier interfaces were characterized by surface-analytical techniques. The results of characterization permitted fabrication of junctions with Nb_3Sn and Mo-Re base electrodes and Pb, Pb-Bi and Mo-Re counterelectrodes having nearly ideal current-voltage characteristics. These counterelectrodes were deposited at temperatures not exceeding T = 100°C. The Mo-Re counterelectrode formed at low T had a critical temperature, T_c, of only 8K. A high-critical-temperature Nb_3Sn counterelectrode requiring high deposition temperatures could not be fabricated successfully. The main cause of this negative result was the nonuniform coverage of the base with overlayers which contained thin or defective spots. In contrast to Nb_3Sn, high-T_c NbN counterelectrodes were successfully fabricated and sumgap voltages exceeding 5 mV were measured at 4.2K. The report contains new information on artificial barriers and on Mo-Re and Nb_3Sn superconducting films.

LIST OF FIGURES

LIST OF TABLES

1. INTRODUCTION

1.1 Program Objective

The overall objective of this program was to develop a technology of thin-film Josephson tunnel junctions capable of operating at temperatures, T_{op} > 10 kelvin, compatible with the performance of small closed-cycle refrigerators. The availability of such junctions would make it possible to incorporate superconducting electronics into mobile/airborne electronic warfare and advanced radar systems.

The specific objective was to demonstrate the technical feasibility of thin film tunnel junctions with electrodes fabricated from A15 compounds and/or hard alloy superconductors, such as Mo-Re, having critical temperatures, T_c, sufficiently high to achieve useful device characteristics at temperatures exceeding 10 kelvin. This would permit a comparison with high-T_c, B1 structure NbN and NbCN junctions that are under active development in several R&D organizations in the United States and overseas.

The program tasks defined in the Statement of Work were:

Task 1. Investigate A15/rare-earth oxide and Mo-Re/oxide interfaces to identify the oxide species and their depth profiles.

Task 2. Develop a selective anodization process for A15 and Mo-Re films.

Task 3. Fabricate and characterize A15 and Mo-Re reference tunnel junctions with low-T_c soft alloy and Nb counterelectrodes.

Task 4. Determine the preferred approach to high-T_c counterelectrode fabrication.

Task 5. Fabricate and test high-operating-temperature (> 10K) prototype tunnel junctions.

The objectives of this program were complementary to those of the more basic program on "Superconducting Electronic Film Structures" aimed at laying scientific foundations for the high-operating-temperature junction technology. That program is supported in part by the Air Force Office of Scientific Research (AFOSR) under Contract No. F49620-85-C-0043 (and preceding contracts). It will be referred to in this report as the "AFOSR program."

1.2 Approach

The approach was based on the use of a novel ultra-high-vacuum (UHV) closed system referred to as the Westinghouse Superlattice Deposition and Analytical Facility (SDAF). This has made it possible to deposit, process and characterize bilayered and multilayered film structures without breaking the vacuum. From these film structures, which incorporated the superconducting electrode(s) and the tunneling barrier, junctions and/or junction components could be patterned.

The dominant approach to the formation of superconducting thin films was to co-evaporate the elemental components of the

A15-structure compound or an alloy in an UHV environment. Sputter-deposition was also used, but to a lesser extent.

The dominant approach to the formation of tunneling barriers has been to deposit on the superconducting base electrode and to oxidize a thin overlayer of a metal which forms a chemically, mechanically and thermally stable oxide, without suboxides, upon exposure to an oxygen-containing atmosphere. Direct deposition of an oxide was also attempted in the final phase of the program. Metal overlayers were either evaporated or dc magnetron-sputtered. Direct oxide deposition was by rf magnetron sputtering.

The key problems to be solved were:

1. To find an artificial tunneling barrier that would perform well with high-T_c electrodes. This requires that there be no chemical interaction and no interdiffusion with the electrodes at whatever processing temperature is necessary to synthesize a high-T_c superconductor. A compatibility with the crystalline structure of the counterelectrode may also be required.

2. To form a counterelectrode having a high T_c within a coherence length, ξ_s, of the barrier/counterelectrode interface (the ξ_s is of the order of 3 to 5 nm in high-T_c, type II superconductors). For the A15-compound films, this requires a high degree of crystalline order in the initial deposit. Consequently, the choice was made to study and use crystalline and epitaxial barriers on which ordered counterelectrode films could be grown.

The Mo-Re superconducting alloy counterelectrode was proposed as a possible solution to both problems. Indeed, we found that it can be formed near the room temperature, thus minimizing the thermally activated interdiffusion with the barrier, and it does not oxidize readily so that it should not reduce the barrier. Also, the T_c in Mo-Re is relatively insensitive to disorder so that the second problem could be minimized. However, with a T_c of only up to 12K, the bcc-structure alloy is clearly inferior to the B1-structure NbN or NbCN compound which can exhibit T_c's up to 16 and 17K.

1.3 Summary of Results

Most significant results and conclusions obtained in each task are listed below.

Task 1. The Y/Y_2O_3 overlayer (representing the rare-earths) was found by X-ray photoelectron spectroscopy (XPS) and tunneling to form an excessively thick self-limited oxide layer resulting in very high barrier resistances. Consequently, Al/Al_2O_3 and Mg/MgO overlayers having lesser self-limited oxide thicknesses were investigated in more detail. The XPS has shown that the Al/Al_2O_3 overlayer can retain its integrity up to 750 degrees centigrade and can be compatible with the high processing temperatures required for A15 counterelectrodes. Yttrium was found, however, to diffuse less than Al into the base electrode.

Task 2. The reactive ion etching (RIE) process was used,

instead of anodization, to pattern the junctions. It was found that thin Al_2O_3 and MgO barrier layers represent convenient etch-stop points thus facilitating the control of this process. Aperture (stencil) masks were also used to form counterelectrodes in an ex-situ junction fabrication sequence.

Task 3. Low subgap conductance tunnel junctions were fabricated with Nb, Nb_3Sn, and Mo-Re base electrodes, Al/Al_2O_3 or Y/Y_2O_3 overlayer barriers and lead or Pb-Bi counterelectrodes.

Task 4. The preferred approach to high-T_c counterelectrode formation was determined to be that of epitaxial growth. This approach was believed necessary since even in the Mo-Re counterelectrode the gap voltage near the interface with the barrier was depressed from 12K to 8K.

Task 5. The goal of this task was not attained since high-T_c A15 or Mo-Re counterelectrodes could not be demonstrated and high-operating-temperature tunnel junctions were not fabricated with such counterelectrodes. In contrast, high-T_c NbCN counterelectrodes were obtained recently under the AFOSR program, using the approach defined in Task 4. Earlier in 1985, high-T_c NbN or NbCN counterelectrodes were also obtained in two other laboratories: ETL in Japan and NRL in USA.

The overall conclusion derived from this program is that the approach to the problem remains correct but the A15 high-T_c counterelectrodes are much more difficult to obtain than those of NbN or NbCN. The difficulty is largely related to the necessary use of crystalline and epitaxial tunnel barriers having a low subgap conductance and crystalline compatibility with the A15 structure. Such barriers were not obtained to date. Consequently, high-operating-temperature junctions with NbN or NbCN electrodes represent the only short-term option available. More work is required to attain all-A15 high-T_{op} junctions. The feasibility of such junctions was, however, not disproved.

1.4. Notation

Throughout this text a layered film structure fabricated to form a tunnel junction is defined in the sequence of depositing the layers: substrate/base/overlayer (barrier)/counterelectrode.

2. EXPERIMENTAL APPARATUS AND METHODS

2.1 Film Deposition

Preliminary film deposition experiments under this program, which preceded the implementation of the present equipment, were performed using a dc diode sputtering system [1]. Its description is not reproduced here since it has little archival value. Since May 1983, sputtered superconductor and barrier films were deposited in the four-magnetron-gun vacuum chamber. Its present version is described in Appendix A. Description of the first version is given in [2]. In early 1984 that chamber was integrated into the SDAF (Appendix A). Co-evaporation of superconducting films and evaporation of metallic overlayers have been performed only in the SDAF.

2.2 Analytical Methods

X-ray photoelectron spectroscopy (XPS) was used extensively throughout this program. The SDAF is presently equipped with a Riber MAC-1 electron energy analyzer having a limited sensitivity and poor energy resolution of, at best, 1.5 to 2.0 eV. The angle between the normal to the sample and the detector, θ, is fixed and ill-defined. Consequently, this XPS apparatus was used mostly for qualitative, in-situ analysis. The quantitative and angle-dependent XPS was carried out mostly ex-situ, in an ESCALAB Mark

II (VG Scientific) equipped with a hemispherical electron energy analyzer. The $Mg_{K\alpha}$ and $Al_{K\alpha}$ radiation was used without a monochromator. Many films analyzed were deposited on sapphire substrates and were not electrically grounded. Consequently, shifts in the kinetic/binding energy up to 10 eV were observed. However, in the ex-situ procedure the analysed films were always exposed to air and enough carbon was present on the surface to calibrate all other photoelectron energies to the known energy of C_{1s}. High resolution spectra have been recorded with an analyzer pass energy of 20 eV which corresponds to 1.2 eV resolution. The angle, θ, was defined to $\pm 6^{o}$ since the entrance aperture of the analyzer subtends a 12 degrees arc. The analysis could be performed at temperatures between ambient and approximately $800^{o}C$. The typical operating vacuum level was 10^{-9} to 10^{-10} torr.

A scanning electron microscope (Cambridge, Model MK 150-2) equipped with an analyzer (Kevex 7000) for energy dispersion spectroscopy (EDS) and an electron microprobe (ARL, Model SEMQ) capable of measuring oxygen content have been used for determining chemical composition. An X-ray diffractometer (Scintag PAD 2) has been used for phase identification and lattice constant measurement. The qualitative, in-situ determination of the film crystallinity has been performed in the SDAF by reflection high energy electron diffraction (RHEED).

2.3 Junction Fabrication and Testing

Two methods of junction fabrication have been used: ex-situ and in-situ. In the ex-situ process, an A15 or Mo-Re superconducting base was deposited on 6.4 x 6.4 mm sapphire substrates.

Up to 17 (typically 7) substrates were clamped to a molybdenum block which served as the transfer vehicle and specimen table within the SDAF. The clamps helped to insure an adequate thermal contact to the block and delineated an approximately 4 mm wide deposit strip centered on the substrate. The barrier overlayer was deposited on the base and oxidized thermally or by an ion-beam-assisted process without breaking the vacuum. The completed bilayer was removed from SDAF and briefly exposed to air. The base electrode width was defined either by the width of the deposit strip itself or by hand-painting insulating Q-dope or photoresist over a part of the strip surface. The painted layer helped also to protect the base step-edges from shorting to the counterelectrode. Subsequently, the bilayer was placed under an aperture mask defining the 0.25 mm wide counterelectrode strip and a counterelectrode film deposited. The four counterelectrode contact pads were positioned on the uncoated part of the substrate as shown in Fig. 2.1. Lead and Pb-Bi soft counterelectrodes were deposited in separate evaporation or sputtering facilities.

Refractory counterelectrodes were deposited in the SDAF. In this case, the aperture mask was mounted on a Mo-block. This process resulted in four large-area junctions (approximately 0.05 mm^2) per substrate chip. Due to this large junction size only quasiparticle current-voltage (I-V) characteristics could be determined. The main advantage and principal reason for wide utilization of this process was a very short turn-around time.

The in-situ process consisted of a sequential deposition of all three layers (base/barrier/counterelectrode) without breaking

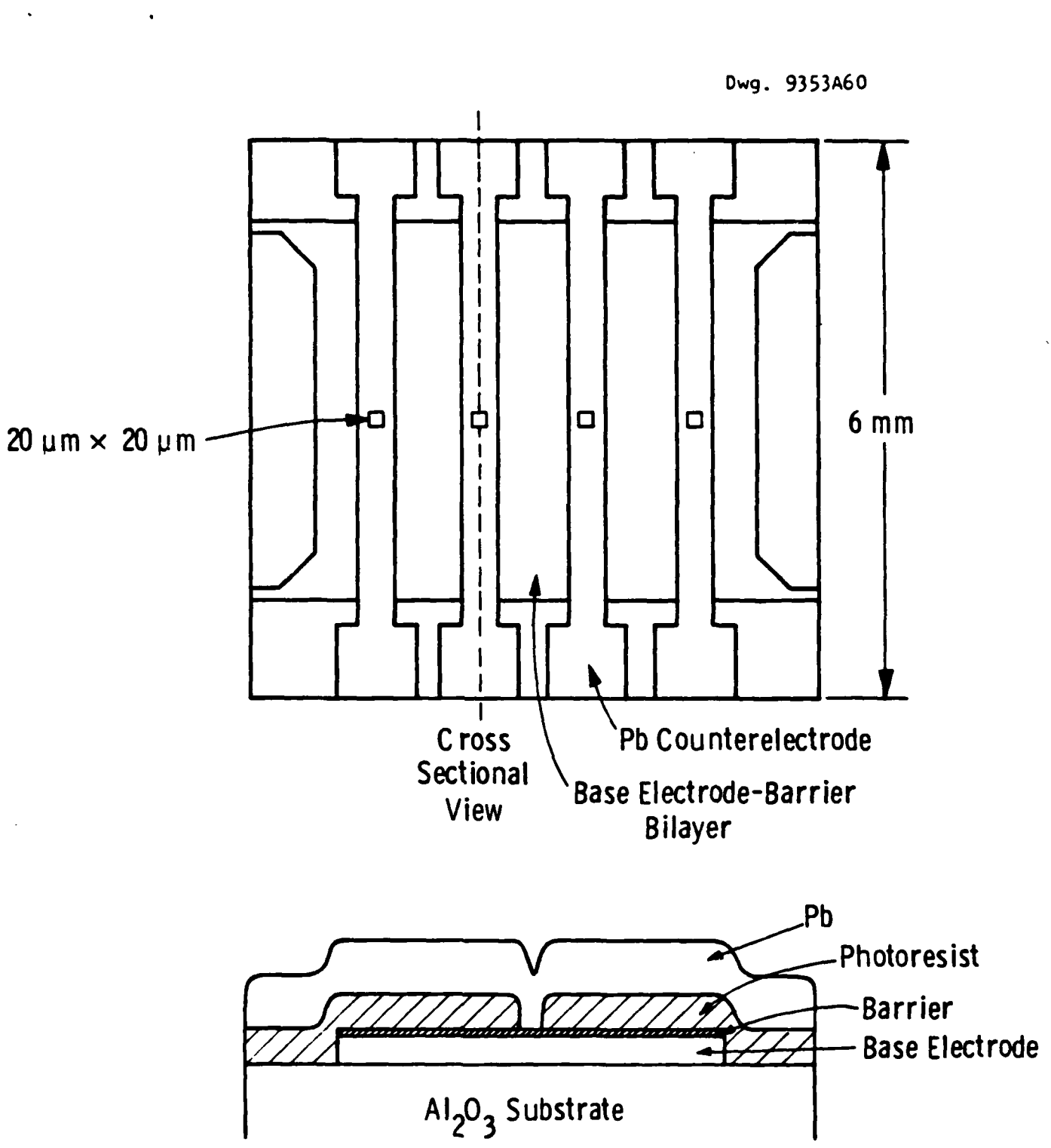

Fig. 2.1 Geometry of a single 6.4 × 6.4 mm sample prepared for tunneling in a top view and in cross section.

the vacuum. The barrier oxidation, thermal or ion-beam-assisted was performed in the SDAF prior to depositing the counter-electrode. A simple process with turn-around times of 2 to 3 days was used to delineate junction areas from trilayers upon removal from the SDAF. Figure 2.2a shows the trilayer covering the entire substrate except for the area under the clamps. The four counterelectrode areas (20 x 20) micrometers were protected by patterned photoresist while the counterelectrode was etched. Both wet etching and reactive ion etching (RIE) were used in the course of the program. In the latter case Freon 12 was used as the etching gas. The etched sample is shown in Fig. 2.2b. The Al_2O_3 and especially MgO oxide served as an effective etch-stop so that only a small fraction of the base thickness was removed even with a very relaxed etch-rate control. A second layer of photoresist was patterned as shown in Fig. 2.2c and left in place to insulate the base electrode from the metallization layer shown in Fig. 2.2d. This layer, usually Pb-Bi, permitted one to make contact with the patterned counterelectrode. The metallization layer was deposited through an aperture mask identical to those used in the ex-situ process.

Three measuring probes have been used. All have press-contact electrical connections to the sample for rapid turn-around. One probe permits a resistive measurement of transition temperature and van der Pauw[3] measurement of resistivity as a function of temperature, in a liquid helium storage dewar with a 12.8 mm (1/2 inch) neck. A calibrated germanium thermometer is used for temperature measurement, and the height of the sample/thermometer block above the level of helium liquid is used for temperature

Dwg. 9379A58

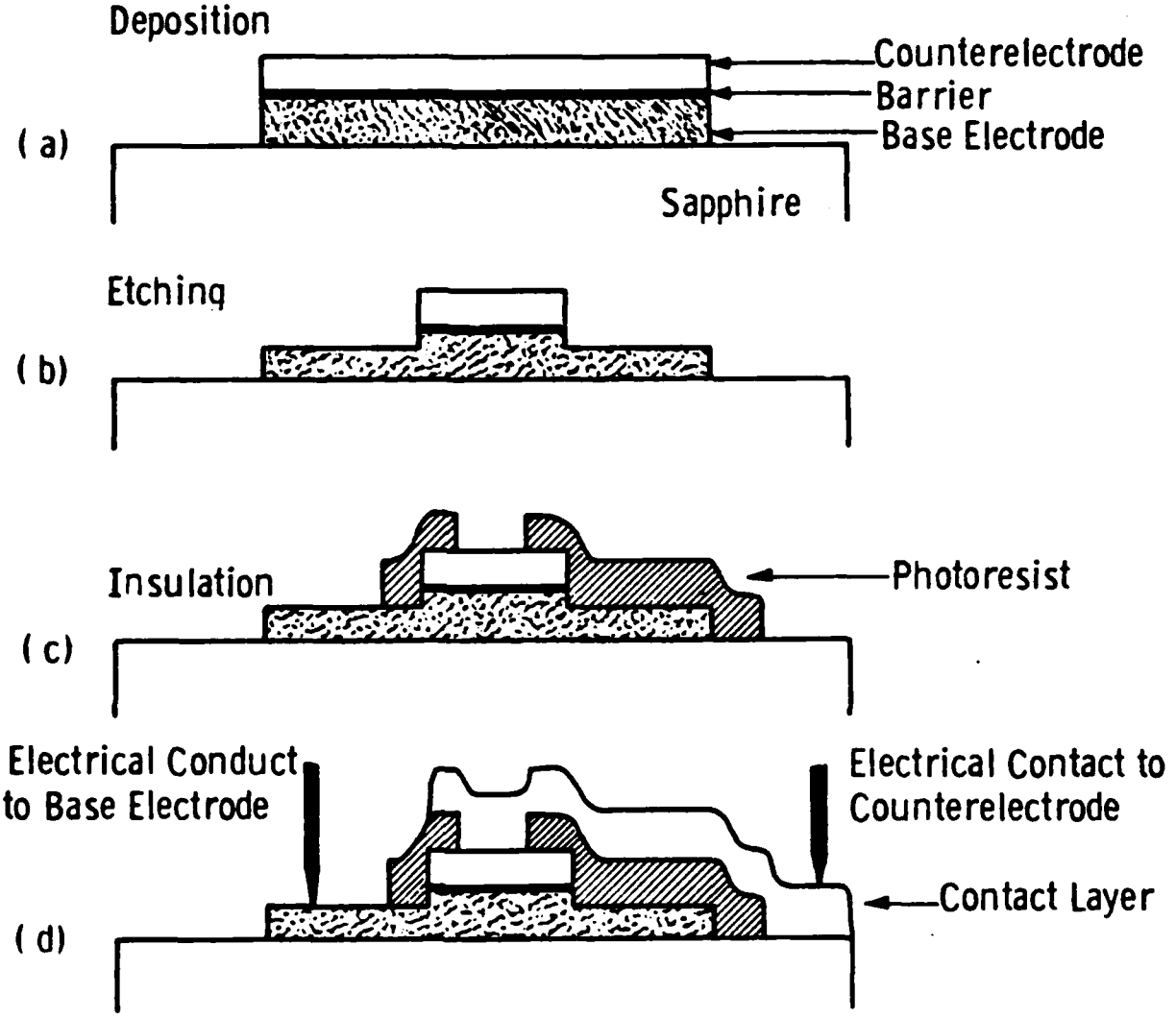

Fig. 2.2 Processing steps to form a tunnel junction from a trilayer formed <u>in situ</u>.

control. The estimated accuracy of the measurement is ±0.1 kelvin. An air-lock allows the sample to be warmed from cryogenic to room temperature in dry nitrogen gas. The second probe has ten press contacts configured for four-point measurements of the I-V characteristic of four junctions on one standard (6.4 mm x 6.4 mm) chip. This probe is also compatible with the air-lock-equipped liquid helium storage dewar and is intended for measurements at 4.2K. The third probe accommodates four standard substrate chips. Sixteen contacts are made to each chip, thus permitting a four-point measurement of the I-V characteristic of each tunnel junction and the resistivity of the base electrode. Liquid He must be transferred to a 4-inch dewar. The temperature of the samples is controllable because a vacuum space isolates the probe from the liquid helium.

Electrical characterization of tunnel junctions was limited to quasiparticle I-V characteristics, as already mentioned above. The large junction areas in most of fabricated samples resulted in sufficient self-shielding to preclude a reliable determination of the junction critical current, I_c. Hence, the standard junction quality parameters, the I_cR_N product (where R_N is the normal resistance of the junction above the gap voltage) and $V_m = I_cR_S$ (where R_S is the subgap resistance) could not be determined directly. Instead, the ratio of currents at fixed voltages above and below the gap: $Q = I_N/I_S$ was used as a quantitative indicator of the junction quality at 4.2 K. For junctions with a sum of base and counterelectrode gap voltages less than 4 mV the ratio Q = I(4 mV)/I(2 mV) was used. For junctions with a sum of gap voltages > 4 mV, the ratio was Q = I(6 mV)/I(3 mV). As shown in

Ref. 7, Q is related to V_m. By making the ratio of fixed reference voltages above and below the gap to always equal 2, the estimated value of V_m is:

$$V_m = 1/2(I_cR_N)_{th}Q \qquad (1)$$

where $(I_cR_N)_{th}$ is the maximum theoretical value of the product at a temperature T in the absence of any proximity layer. Assuming the BCS relation $= 1.76\ k_BT_c$ one obtains at zero kelvin: $(I_cR_N)_{th} = 240\ T_c$ (microvolts). For $T/T_c < 0.3$ the zero kelvin value holds. For Nb ($T_c = 9.2$ K, $T/T_c = 0.46$) the value must be calculated from the theoretical BCS expression [4] and is approximately 15 % lower. Substituting the zero kelvin value into (1) one obtains:

$$V_m = 0.12\ T_cQ\ (mV) \qquad (2)$$

Proximity effect will reduce V_m. However, for high sum gap voltages one will usually obtain $V_m > Q$.

The sum of gap voltages was determined from the I-V characteristics by taking the maximum derivative (highest inflection) point on the curve. To obtain the base electrode gap voltage, the Pb or soft alloy gap (well-defined by the composition) was substracted. For all-refractory junctions the separation was not possible.

3. RESULTS AND DISCUSSION

3.1. Task 1 - Superconductor/Barrier Interfaces

3.1.1. Objective

The objective of this task was to determine requirements for fabricating tunnel junctions with the base electrode gap voltage approaching the bulk material value, unaffected by adverse physico-chemical effects occuring at the base/artificial barrier interface. These effects depend upon the barrier type and the method of its fabrication. The complementary objective was thus to investigate some of the barrier fabrication parameters. Further characterization of barriers is included in the description of Tasks 3 to 5. Under Task 1 results were obtained in the following problem areas:

1. Surface segregation in A15 superconductor base.
2. Interdiffusion between the base and the artificial barrier overlayer.
3. Barrier overlayer thickness uniformity.
4. Oxidation of metallic barrier overlayers.

Studies of the superconductor/barrier interface were originally scheduled for the first year of performance under the three-years' program. They continued, however, until its comple-

tion since the barrier properties and the resulting junction performance critically depend upon the investigated interface.

3.1.2. Surface Segregation

Atomic segregation near the A15 superconductor's surface can significantly alter its composition over depths comparable to the coherence length. The T_c and the energy gap, , decrease by 10 to 15% per each atomic percent deviation from the stoichiometric 3:1 composition. Consequently, a degraded proximity layer may define the base electrode gap voltage if segregation occurs due native or artificial oxide barrier formation. The first systematic XPS study of the surface segregation of A15 compound surfaces which is induced by the presence of oxygen on the surface was performed by Ihara and coworkers.[5] Work under this program, performed at the same time, concentrated on the comparison of V_3Si, Nb_3Sn and V_3Ga. The V_3Si was originally chosen as the representative A15 material for this program. The results of the XPS study are summarized in Appendix B, and a general discussion of the effect is given in Appendix C. Upon surface oxidation, the segregation of the Nb_3Sn was found to be less dramatic than that of V_3Si. In contrast to V_3Si, no change in the composition of Nb-Sn at the interface with its oxides could be observed within the resolution of the ESCALAB XPS apparatus. A direct consequence of these findings was the replacement of V_3Si by Nb_3Sn to serve as the representative, stable A15 material for junction fabrication and studies. The growth conditions for Nb_3Sn films are presented below, under Task 4.

Minimal oxidation and no surface segregation were found in

Mo-Re. These results are also presented in conjunction with Task 4. It surfices to state here that the Mo-Re/barrier interface presented no real problems except one. Since Mo-Re does not oxidize readily, the pinholes in the barrier, if present, cannot be sealed by the native oxide. Yields of junctions with the Mo-Re base and soft electrodes were consistently lower than those for Nb_3Sn and especially NbN base. This indicated that pinholes were present in the barriers under investigation. Mo-Re is, therefore, a suitable test material for studies of the barrier integrity.

3.1.3. Interdiffusion

In the case of metallic overlayers deposited on the base electrode to form a barrier, and oxidized after the deposition, an interface is initially formed between the base surface and the metal. If the overlayer is thick enough a thin unoxidized metal layer may remain even after the oxide is formed. Kwo and coworkers were the first to observe by XPS that the thickness of this residual layer is less than expected from the deposition rate and measured oxide thickness.[6] They attributed this "loss" to the thermally activated grain boundary diffusion of the overlayer metal (Al) into the polycrystalline base film (Nb). Interdiffusion of this type may cause the degradation of the superconductor's gap energy, especially if higher processing temperatures are involved which will be necessary for junctions with A15 counterelectrodes. Under this program, XPS was used to investigate the effect of temperature on the diffusion of Al and Y overlayers into Nb and V_3Si base electrode. The results are presented in Appendix C. Under the AFOSR program diffusion of Mg

into NbN was also investigated (Appendix B and C). The most important conclusions referring to comparable conditions of experiments are:

1. Yttrium diffuses less into the base than Al due to a larger atomic radius of Y.
2. Diffusion of Y and Al into polycrystalline V_3Si is less pronounced than into polycrystalline Nb.
3. Diffusion of Al into single-crystal Nb is not observed up to 750°C. This proves that it occurs along the grain boundaries of the base.
4. The Al/Al_2O_3 overlayer on single-crystal and even polycrystalline Nb retains its XPS-defined integrity up to 750°C. This overlayer is thus potentially compatible with high-temperature processing.
5. Magnesium diffuses into and/or reacts with NbN above 300 to 500°C.
6. No deleterious effect on the base gap voltage or subgap conductance was observed as a result of Al or Y diffusion along grain boundaries of the base. In contrast, Mg diffusing into NbN increased the subgap conductance of the latter.

3.1.4. The Overlayer Thickness Uniformity

The rationale for concentrating on oxidized metallic overlayer barriers was provided by the observation of Rowell and coworkers that even extremely thin metallic overlayers of Al are capable of coating the Nb base such that upon thermal oxidation

the barrier properties are "Al_2O_3-like" rather than "Nb_2O_5-like".[7] The proposed explanation of this effect was that a few monolayers of Al are capable of completely "wetting" the Nb base.[8] Calculations based on a theoretical wetting model[9] indicated that no major differences in wetting of Nb or V by all metallic overlayers considered in this program should be expected. Consequently, their use should result in an adequate coverage of the base assuming that the surface properties of A15's are not too different from those of their major metallic component (Nb or V). A discussion of wetting is included in Appendix C. It was thought that metallic overlayers will cover the base better than a directly deposited oxide.

No prediction can be made of the overlayer thickness uniformity. Consequently, an XPS evaluation of that uniformity was performed under this program. Appendix C shows XPS results that indicate that even in the case of best-wetting amorphous Si on extremely smooth amorphous Mo-Ge the overlayer thickness fluctuation was comparable to the thickness itself. Single crystal Nb-surface was covered more uniformly by Al than a polycrystalline Nb-film. The conclusion from this work is that thin or "weak" spots are likely to be present in all overlayers investigated here and that this problem will be aggravated by the base roughness and grain boundaries. A micro- or single-crystalline A15 base would permit a relatively best overlayer uniformity. A coarse-grained base will be least suitable.

3.1.5. Barrier Oxidation

Thermal growth of oxides on metal overlayers such as Al, Y,

or Mg is self-limiting. To permit the ex-situ junction processing, and to obtain an easy control and reproducibility of the barrier thickness in the in-situ process (Section 2.3) the use of self-limiting oxide thicknesses was preferable in this program. Appendix C (Table 3) shows the self-limiting thicknesses determined by XPS and the corresponding junction resistances. Room temperature oxidation of yttrium produced an approximately 4 nm thick oxide, and, correspondingly, very high, rather impractical junction resistances of 10^2 ohm-cm^2. This high junction resistance, and the strong tendency of Y to form hydroxides (Appendix C and Ref. 1) that complicate the ex-situ processing resulted in the Y/Y_2O_3 barrier to be de-emphasized in this program in favor of Al/Al_2O_3.

Ion-beam assisted oxidation was used for the first time to form artificial barriers. This process, discussed in Appendix D, produced Al/Al_2O_3 barriers with an increased thickness and barrier height that were suitable for NbN-counterelectrodes discussed under Task 5 but not for A15. Thermally oxidized barriers worked satisfactorily only for Pb, Pb-Bi and Mo-Re counterelectrodes (Task 5).

3.1.6. General Conclusions From Task 1

Work under Task 1 permitted one to determine conditions suitable for obtaining an A15 (Nb_3Sn or V_3Si) base electrode protected from degradation by a metal/oxide overlayer. For Al- and Y-overlayers this should be possible as long as some unoxidized metal is left between the base and the oxide. XPS was an indispensable tool for obtaining the results.

3.2 Task 2 - Analogue to SNAP Process

Some process was needed for patterning base/barrier/-counterelectrode trilayers formed *in situ* in analogy to the Selective Niobium Anodization Process (SNAP) developed at Sperry Research Center for Nb/Si/Nb junctions.[10] The motivation for such a process was to achieve more uniformity in junction parameters by protecting the barrier from exposure to air, dust, photoresist, and wet chemicals. An outline of the process that was used during this program was presented in Section 2.3 and Figure 2.2. Background information and details of that process will be presented here.

At the beginning of this program, private information was obtained from Sperry that anodization does not work well with Nb-based compounds such as NbN. At the same time, Gurvitch et al. demonstrated the use of plasma etching (SNEP) to define Nb counterelectrode areas.[11] Plasma etching utilizes a reactive gas, usually fluorine or chlorine-based, to form volatile reaction products. Thus it is a highly-selective process which is effective for all of the high-T_c superconductors of interest, but cannot etch through an entire trilayer containing an Al_2O_3 or MgO barrier.

The temperature at which the vapor pressure reaches 1 torr is listed in Table 3.1 for a number of the reaction products created by plasma etching. Those which are volatile at low temperatures include such products of the etching of high-T_c superconductors as NbF_5 and MoF_3. Those which are stable at room temperature include the products of several barrier materials such as AlF_3 and MgF_2.

Table 3.1 — The temperature at which RIE reaction products have a vapor pressure of 1 torr

Compound	Temperature (°C)
AlF_3	1240
$AlCl_3$	100
MgF_2	~ 1000
$MgCl_2$	640
MoF_6	- 70
NbF_5	90
$NbCl_5$	~ 100
SiF_4	- 150
$SiCl_4$	- 60
$SnCl_4$	310

Reactive Ion Etching (RIE) is distinguished from plasma etching in that there is also a physical ion bombardment associated with the chemical processes which slowly removes material of any vapor pressure by sputtering. The difference arises from the fact that samples are placed on the powered electrode in RIE and are placed on a grounded or floating potential for plasma etching.

Etch rates and parameters for RIE (Table 3.2) were established for Nb, Nb_3Sn, and Mo-Re for this program, and for other materials, such as NbN, independent of this program. Figure 3.1 clearly shows how the etched step height of NbN, plotted as a function of etching time, can be affected by a thin, oxidized overlayer of aluminum. An extra 4.5 minutes, enough time to remove 250 nm of NbN, was needed to etch through a 2.0 nm thick Al_2O_3 barrier. The native oxides of NbN and Si on the surfaces of the other samples did not affect the rate since the step-height data for those samples extrapolated to the origin of the plot.

Table 3.2 includes etch rates from two different RIE systems. An Anelva system was used for the second year and half of the third year of the program. A Semi Group 1000 TP, available in the last 6 months of the program, was a dedicated system for superconducting devices.

Therefore, RIE permitted the delineation of counterelectrode areas and the patterning of an entire trilayer with large tolerances in the required etch times. This control over process end-points was peculiar to the particular materials being studied for high-T_{op} tunnel junctions. It is a fortuitous advantage that is in addition to the usual advantages of RIE.

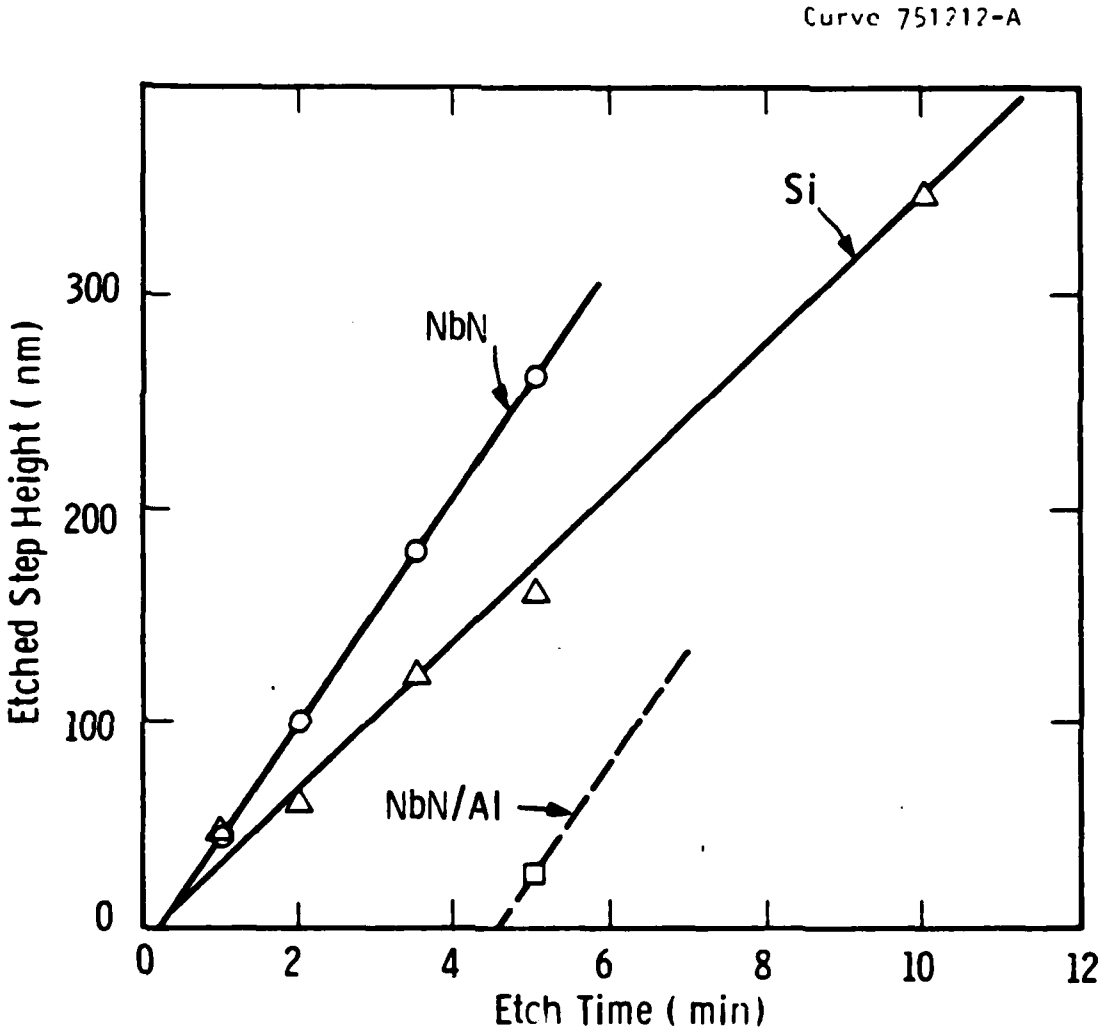

Fig. 3.1 Example of RIE etch rate calibration. The etching gas and power were CCl_2F_2-15% Ar gas at 75 mtorr and 0.4 W/cm_2. No additional etching time was needed to remove the native oxides of NbN and Si, but an additional 4 minutes were needed to remove 2.0 nm of oxidized Al.

Table 3.2 — Typical etch rates and etching parameters for RIE

Material	Etch Rate (nm/min)	RIE System	Etching Gas	Pressure (millitorr)	Power (W/cm^2)
Nb	28	Anelva	CF_4	30	0.2
Mo-Re	40	Anelva	CF_4	30	0.2
	10	SEMI	CCl_2F_2-15% Ar	75	0.6
Nb_3Sn	95	SEMI	CCl_2F_2-15% Ar	75	0.6
NbN	35	Anelva	CF_4	30	0.2
	50	SEMI	CCl_2F_2-15% Ar	75	0.6
	25	SEMI	NF_3	75	0.6
Al_2O_3	0.5	SEMI	CCl_2F_2-15% Ar	75	0.6
MgO	~ 0.3	SEMI	CCl_2F_2-15% Ar	75	0.6
Si	35	SEMI	CCl_2F_2-15% Ar	75	0.6

3.3 Task 3 - Reference Tunnel Junctions

3.3.1 Objective

The objective of this task was to demonstrate that the results of Task 1 permit one to fabricate tunnel junctions with undegraded high-T_c base electrode gap voltages and low leakage barriers when using lead, soft alloy, or Nb counterelectrodes. The specific goals were to:

1. Verify that adequate coverage of the base by the overlayer and protection from oxidation were achieved.
2. Verify that the base/overlayer interdiffusion did not affect the base gap voltage.
3. Determine the homogeneity of superconducting base films within a coherence length from the base/overlayer interface.
4. Characterize the barrier itself.

The original intention was to separate the issues concerning the base electrode/barrier interface and the barrier itself from those specific to the barrier/counterelectrode interface and the high-T_c counterelectrode. Results obtained later under Tasks 4 and 5 have shown that such separation was not justified.

3.3.2 Niobium-Base Junctions

The Nb-base junctions were fabricated and characterized to perform a preliminary barrier test prior to investigating the high-T_c and counterelectrode material candidates. Polycrystalline Nb films were dc-magnetron sputtered on sapphire substrates. Highly textured and single crystal Nb films were e-beam

evaporated on epitaxially polished sapphire, usually having a $(11\bar{2}0)$ orientation. The corresponding orientation of Nb was (110). Electron-beam evaporated and dc-magnetron sputtered Al-overlayers and e-beam evaporated Y overlayers were oxidized and characterized. Thermal oxidation was performed by exposing the overlayer to 100 mtorr of dry oxygen for up to 1 hour at room temperature. The oxidized sample was exposed to air of unknown humidity for at least 10 min prior to the deposition of a soft counterelectrode. The effect of short exposure to humid air on the barrier properties remained largely unknown. Long exposures, of several days duration, were found to significantly degrade the Q of Al-oxide barrier junctions. Ronay and Latta found, however, that exposure to humidity was crucial for obtaining low-leakage Y/Y_2O_3 barriers.[12]

Figure 3.2 summarizes the experience gained with Al/Al_2O_3 barriers on Nb. Current-voltage characteristics are compared for barriers and base electrodes fabricated by different methods which resulted in differences in the barrier crystallinity. No differences between these junctions appeared in XPS characterization of the oxidized Nb/Al bilayers. All had a layer of Al_2O_3 approximately 2 nm thick, a layer of unoxidized Al underneath that was slightly less than 1 nm thick, and a Nb surface which showed no signs of oxidation - even with the XPS energy analyzer (ESCALAB) at a glancing angle.

Aluminum overlayers e-beam evaporated at a rate of 3 nm/min (Fig. 3.2a,b, samples R84-21-B3 and R84-35-B2) were grown on a (110) single crystal Nb that had an atomically smooth surface according to RHEED, and a high resistivity ratio (up to 150).

Curve 751271-A

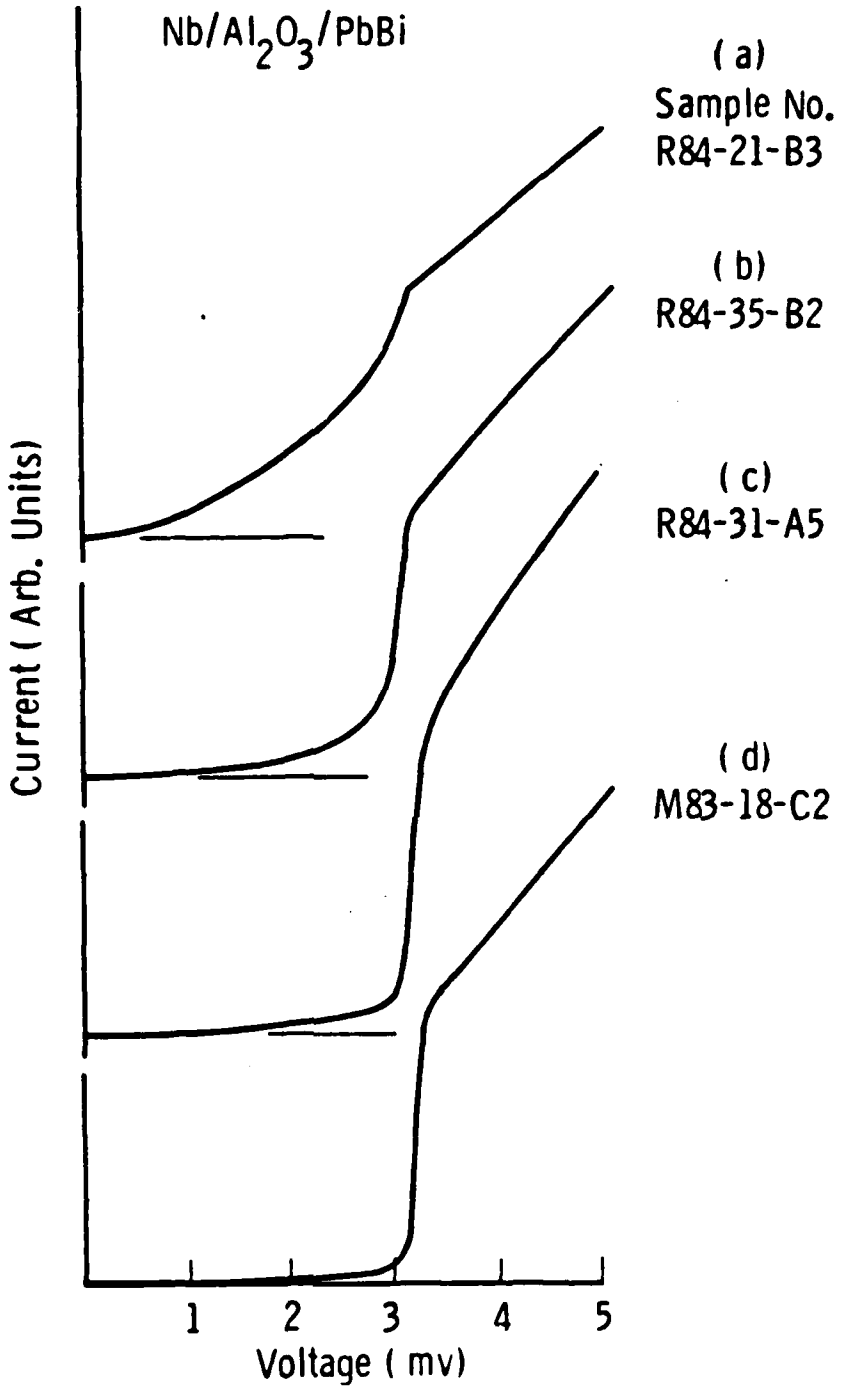

Fig. 3.2 Quasiparticle tunneling characteristics of four Nb / oxidized-Al / Pb-Bi junctions with barriers of different morphologies measured at 4.2K. (a) Highly-textured evaporated Al (b) Amorphous barrier, ion milled after evaporation (c) Highly-textured sputtered Al (d) Randomly-oriented, fine-grained Al grown on sputtered polycrystalline Nb.

The Al deposited on such surfaces was always epitaxial, and exhibited a single crystal RHEED pattern. Upon thermal oxidation the diffraction pattern still indicated a strong texture that in some samples was sufficient to induce (110) orientation in the Nb counterelectrode (Appendix C). The I-V curve of sample R84-21-B3 (Fig. 3.2a) exhibiting a very high subgap conductance was representative of several experiments, always producing the same result. The analogous sample R84-35-B2, used for Fig. 3.2b, was ion-milled after oxidation which made the oxide amorphous or highly disordered. The ion-beam energy was 600 eV, the current density 250 nA/cm^2, and the exposure time 15 min at ambient temperature. After ion-milling the thermal oxidation was repeated. These processing steps significantly reduced the leakage current (Q = 15 instead of 3), although no change in the oxide thickness was observed by XPS. The proposed interpretation of the ion-milling effect (see Also Appendix C) is that it causes: (a) oxide thickness homogenization and improved coverage due to atomic displacements induced by ion-bombardment, (b) partial elimination of stoichiometry defects present in the highly crystalline oxide, and (c) partial elimination of grain boundaries along which an enhanced diffusion of the counterelectrode atoms may occur.

Figure 3.2c shows the I-V curve of sample R84-31-A5 having the Al overlayer dc-magnetron sputtered (standard rate of 0.3 to 0.4 nm/min) on the Nb single crystal. This overlayer was also epitaxial, as in case 3.2a, but the subgap conductance was dramatically reduced, with Q = 34 compared to Q = 3 in 3.2a. This result suggested that thermalized sputtering of Al atoms having

random incident angles produced a much more uniform coverage of Nb than the straight-line evaporation. Finally, Fig. 3.2d shows the I-V curve of sample M83-18-C2 having the Al overlayer dc-magnetron sputtered on polycrystalline Nb that was also sputtered at ambient temperature. The RHEED pattern of Al had diffuse concentric rings characteristic of a microcrystalline film and the tunneling properties were nearly ideal, with Q > 60. While no RHEED pattern of the Al-oxide is available, it is believed to be microcrystalline or amorphous. The result of Fig. 3.2d suggests that all three causes of excessive subgap conductance evoked to explain Fig. 3.2a might be of significance. Of these causes, nowever, the uniformity of coverage appears to be the most critical, at least in the case of soft counterelectrodes.

A correlation between the the subgap conductance and the Al-oxide barrier height, $\bar{\phi}$, was observed. The average barrier height and its electrical width, s, were obtained by polynomial fitting to the theoretical expression for the barrier conductance below the gap given by Simmons (Appendix B). Figure 3.3 shows $\bar{\phi}$ as function of log Q. With increasing subgap leakage the barrier height is decreasing. This result is consistent with the interpretation of $\bar{\phi}$ variation proposed by Halbritter for native Nb-oxide barriers.[13] A real barrier is inhomogeneous and its height is defined by a parallel connection of regions with nearly ideal $\bar{\phi}$, characteristic of the barrier material itself, with narrow defective tunnels having a very low $\bar{\phi}$. In the present case, the Al-oxide barrier height is in excess of 2 eV. Defective regions result from nonuniform coverage and their barrier height, $\bar{\phi}$ < 1 eV, is defined by the native Nb-oxide plugging the pinholes. The

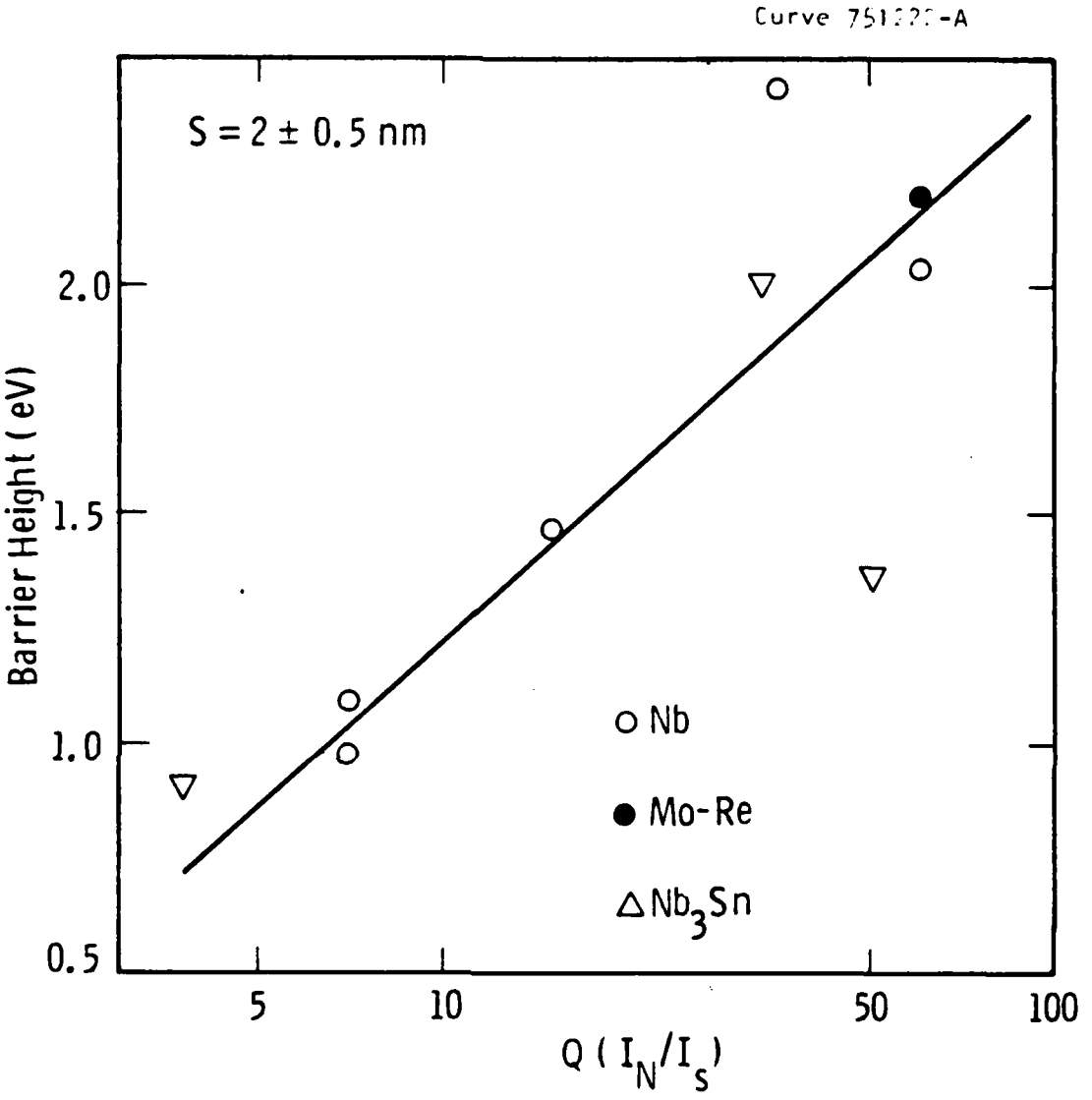

Fig. 3.3 The barrier height inferred from the curvature of the I-V curve in the region 0.1 < V < 0.4 volts, versus log Q. The solid line is a rough fit to the data.

sensitivity of XPS is not sufficient to detect minute amount of oxide in these pinholes.

In contrast to the results obtained with soft counter-electrodes, there was essentially no reduction of the subgap conductance of all-niobium junctions when Al-overlayer sputtering replaced the e-beam evaporation. The I-V curve of Fig. 3.4 is that of a representative junction formed on a single crystal Nb base. The Al-overlayer was sputtered, thermally oxidized, and a counterelectrode consisting of 4 nm sputtered Al plus evaporated Nb was subsequently formed in-situ. The junction was patterned by the method depicted in Fig. 2.2. The Q-value was only 5. Exposing the oxidized barrier to moist air prior to the counterelectrode deposition did not improve the Q. Since it is known that Nb/Al-Al_2O_3-Al/Nb junctions with nominally amorphous barriers can have excellent, high-Q I-V characteristics (Ref. 8), the following tentative conclusion was reached. In the case of refractory counterelectrodes, the high subgap conductance is due to one or both of the two causes:

(1) The crystallinity of the oxide, through the mechanism (c) proposed in the discussion of Fig. 3.2a.

(2) Electrochemical interactions between the refractory counterelectrode atoms and the native oxide in pinholes (Appendix C) reduce the barrier height of these channels.

3.3.3 Junctions with a Mo-Re Base

The polycrystalline Mo-Re base, 70 to 100 nm thick, was typically deposited at 100°C, and strongly textured as shown by

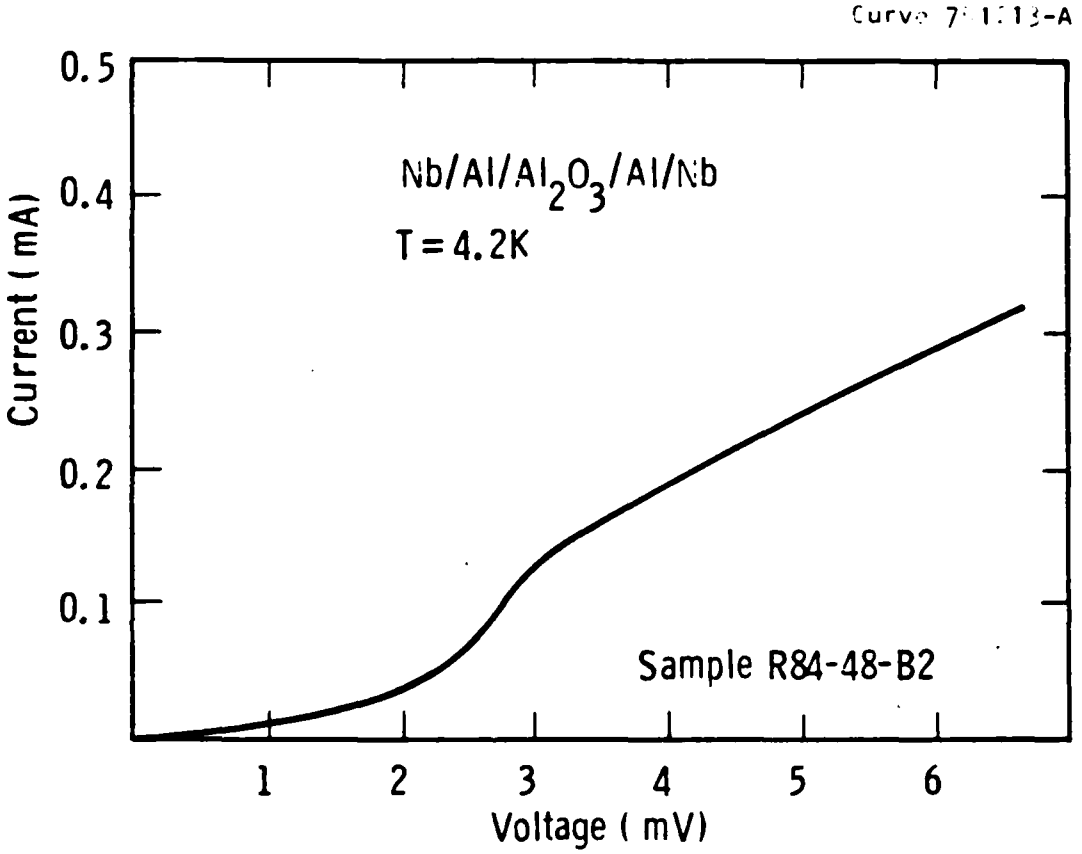

Fig. 3.4 I-V curve for a tunnel junction with a single-crystal Nb base, sputtered and then oxidized Al barrier, and an evaporated Nb counterelectrode.

the RHEED pattern of Fig. 3.10b. Aluminum overlayers evaporated on such base films and oxidized thermally, as described for overlayers on Nb-base, resulted in junctions that even with soft electrodes exhibited microshorts and a very high subgap conductance. Sputtered Al overlayers produced similar results. In contrast, on a 20 nm thick disordered (microcrystalline) Mo-Re exhibiting the RHEED pattern of Fig. 10a, the sputtered Al overlayer barrier resulted in the excellent I-V characteristics, Q > 60, shown in Fig. 3.5. The Al-oxide was 2 nm thick, and the unoxidized Al that remained was 1.3 nm thick, according to XPS. The Al-oxide barrier height exceeded 2 eV (Fig. 3.3). With the very thin base electrode (nominally one coherence length thick) the unoxidized Al-layer resulted in a proximity-effect knee seen in Fig. 3.4 just above the gap. The sharp current rise at the gap voltage showed that the thin base film was homogeneous. In the case of a dc-magnetron sputtered, polycrystalline Mo-Re base, 40 nm thick, the subgap leakage was also reasonably low, with Q = 20 (sample M84-32-B2).

The preparation and superconductivity of Mo-Re are further discussed under Task 4. The tentative conclusion drawn here from the Mo-Re reference junction results is that the base electrode smoothness critically affects the barrier integrity and the subgap conductance. Textured, crystalline deposits of approximately 100 nm thickness are much rougher than very thin microcrystalline films. Since Mo-Re does not oxidize readily, the native oxide of the base is less likely than in the case of Nb-base to plug pinholes that may be enhanced by the nonuniform coverage of a rough surface.

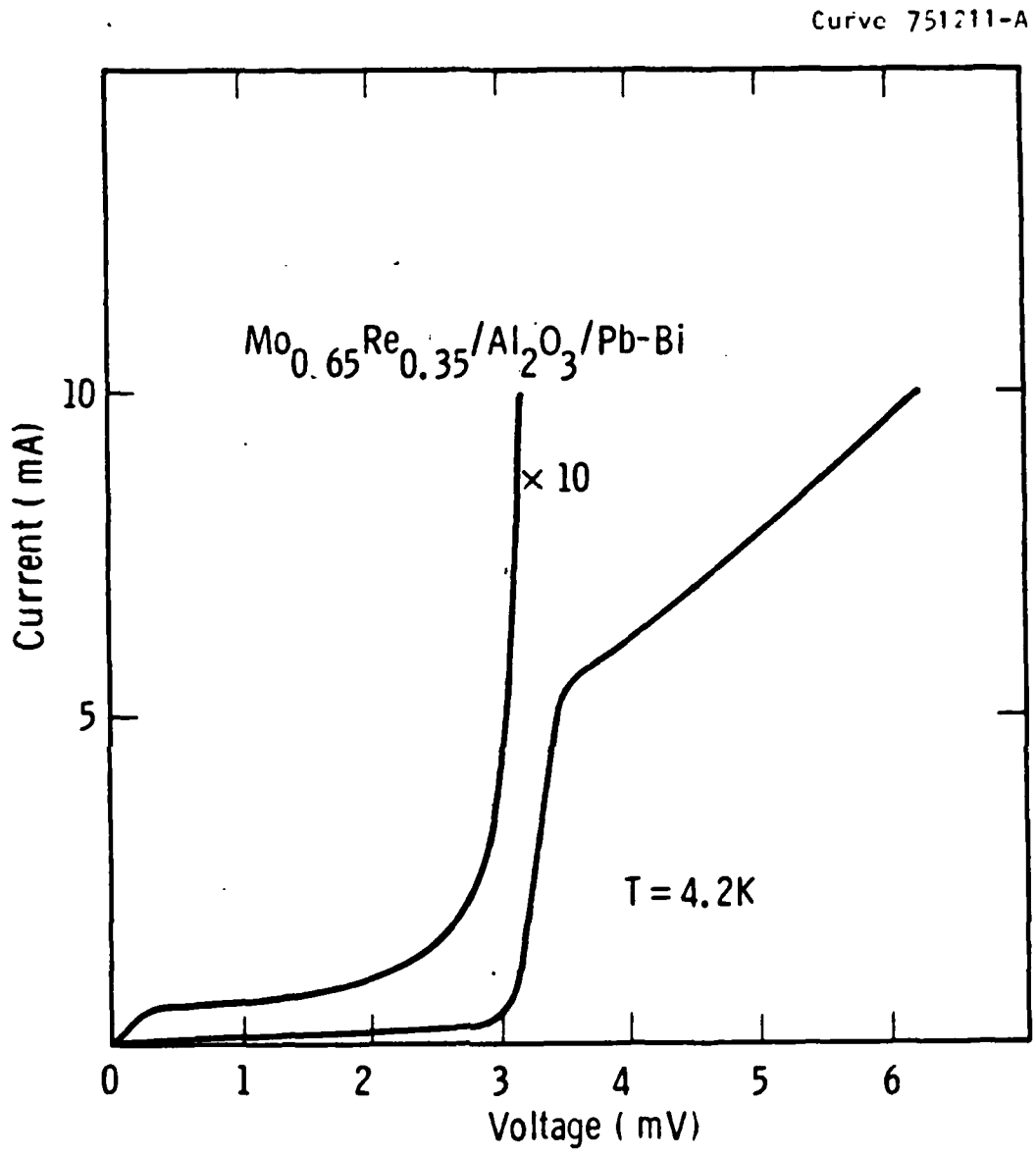

Fig. 3.5 I-V curve for a $Mo_{.65}Re_{.35}$ / oxidized-Al / Pb tunnel junction with Q = 80 measured at 4.2K.

3.3.4 Junctions with a Nb_3Sn Base

In contrast to reference junctions with single crystal Nb or textured Mo-Re base, the evaporated and thermally oxidized Al overlayer permitted one to fabricate excellent reference junctions on single crystal Nb_3Sn when using soft counterelectrodes. Consequently, sputtered overlayers were not investigated in any detail. The fabrication of Nb_3Sn films is described below under Task 4, and the reference junction properties are discussed in Appendix B. It is important to note, however, that these films were typically grown on randomly oriented or $(11\bar{2}0)$ sapphire with the "phase locked" stoichiometric composition. The thickness was of the order of 200 nm, and the RHEED patterns were indicating a single crystal or highly textured deposit. According to RHEED the surface of films deposited on unoriented sapphire was usually highly faceted and, therefore, quite rough. The surface of films on $(11\bar{2}0)$ sapphire was usually less faceted. Using X-ray diffraction, these films were found to be (100) single crystals of good quality as indicated by the X-ray rocking curve linewidth of only 0.4 degrees.

The Al overlayers e-beam evaporated on the films described above at a rate of up to 3 nm/min were nominally 3 to 4 nm thick, epitaxial, single crystal or highly textured. The thermal oxide, obtained in conditions described for Nb-base junctions, was typically 2 nm thick (by XPS), crystalline and textured. Even on most faceted surfaces, however, the Al-oxide barriers had consistently a low subgap conductance with junction Q values between 30 and 80. The fit to the equation derived by Simmons gave barrier thicknesses of 1.5 to 2 nm, in a reasonable agreement with XPS

data, and a barrier height of 0.9 to 2.0 eV (Fig. 3.3). The base electrode gap voltage (midpoint) was 3.25 to 3.55 eV at 4.2 K. According to XPS spectra, niobium in the superconductor was usually protected from oxidation but some Sn-oxide was present in spite of the fact that the unoxidized Al (proximity) layer was approximately 1.2 nm thick.

According to RHEED, yttrium overlayers e-beam evaporated on Nb_3Sn and nominally 4 nm thick, were polycrystalline and less textured than those of Al. The diffraction patterns observed after oxidation were very diffuse with some indication of texture. The Q-values did not exceed 10 (Table 3.2 in Ref. 2 erroneously gives Q = 45). The fit to Simmons' equation gave a 4 nm barrier thickness and a barrier height of only 0.4 eV. The gap voltage at 4.2K was only 3.15 eV, lower than in the case of the Al overlayer. This could be explained by the thickness of Y being comparable to the self-limited oxide thickness and thus insufficient to fully protect Nb_3Sn. Indeed, XPS confirmed ample presence of Nb and Sn oxides. However, unoxidized Y was also prominent and the XPS thickness of the Y-oxide was only .5 nm. An unambiguous interpretation of these results is that the Y-overlayer covered Nb_3Sn much less uniformly than the Al-overlayer. Consequently, the average barrier height was defined by the native oxide areas (rather than just pinholes) while lumps of unoxidized Y remained. Indeed, in the case of the Nb base $\bar{\phi}$ = 1.9 eV was obtained for Y-oxide suggesting that wetting was better in this case. The results described above provided additional justification for de-emphasizing Y overlayer barriers. A comparison of I-V curves of Nb_3Sn junctions with Al and Y over-

layers is shown in Fig. 3.6.

The comparison of the Nb_3Sn-base reference junction properties with those of junctions with Nb and Mo-Re base leads to the clear-cut conclusion that the native oxides of this superconductor (mostly Sn-oxide) effectively plug pinholes and thin regions in the Al-overlayer barrier that result from nonuniform coverage by the overlayer and are more prominent in barriers on rough base surfaces. Consequently, sputtered Al overlayers do not offer any noticeable advantages. This conclusion is supported by the XPS data. Results obtained with Nb counterelectrodes are presented under Task 5.

3.3.5 Conclusions From Task 3

The following conclusions were drawn from the results of Task 3 in conjunction with those of Task 1.

1. The coverage with metallic overlayers and their oxides was nonuniform. This nonuniformity was enhanced by the base electrode surface roughness and inadequate wetting.

2. The pinholes and thin areas resulting from nonuniform coverage were plugged by native oxides. The native oxide of Nb_3Sn (presumably dominated by Sn-oxide) has better electrical properties than the Nb-oxide. Since Mo-Re does not oxidize readily, nonuniform coverage of this base resulted in shorts.

3. The barrier height is averaged over the artificial barrier oxide and the native, possibly defective oxide in pinholes and thin regions.

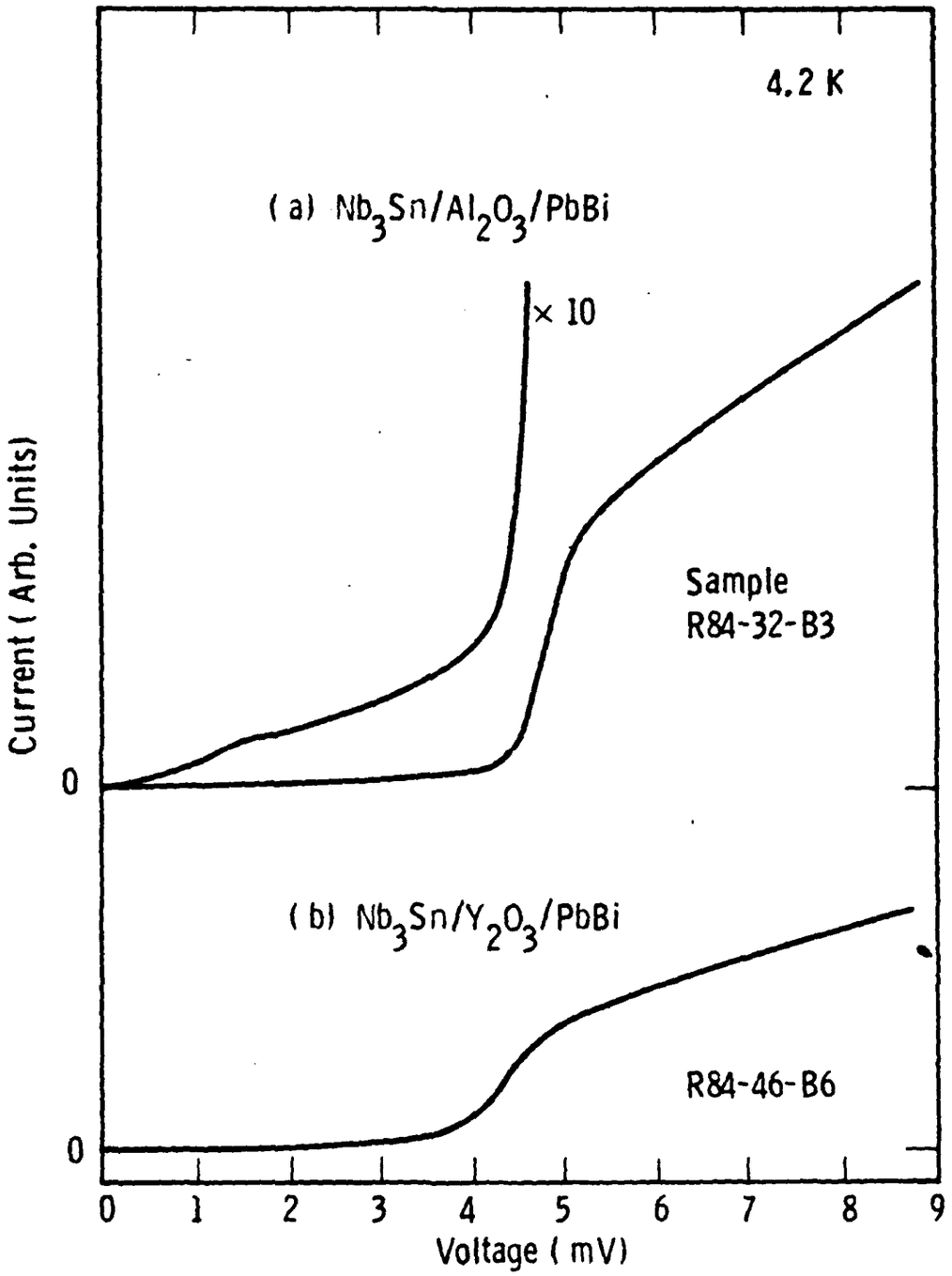

Fig. 3.6 The quasiparticle I-V characteristics of two Nb_3Sn-based junctions. (a) Evaporated (oxidized) Al barrier (b) Evaporated (oxidized Y barrier.

4. Artificial barrier crystallinity and texture did not affect its electrical properties as long as the coverage was sufficiently uniform and a soft counterelectrode was used. In the case of refractory (Nb) counterelectrode, however, the presence of grain boundaries in the barrier could be the cause of increased subgap conductance.

5. Niobium and Mo-Re base films were uniform as indicated by the narrow gap region in the I-V curve. A wider gap region in Nb_3Sn junctions was consistent with Rudman's data (Appendix B) and remained unexplained. The Nb_3Sn base was at least representative of the results by others.

6. No indication of significant base/overlayer interdiffusion was obtained from junction electrical properties.

3.4 Task 4 - Approach to High-T_c Counterelectrodes

3.4.1 Objective

The objective of this task was to determine an approach for obtaining a T_c > 10K within a coherence length of the barrier/counterelectrode interface. This task represented the core of the entire program. The materials which were investigated in the second and third years of the program were Mo-Re and Nb_3Sn. The emphasis on Mo-Re was reduced in the third year for two reasons:

- Low-leakage junctions with NbN counterelectrodes had been successfully fabricated in this laboratory under an AFOSR/Westinghouse program and reports of greater progress with NbN at ETL and ONR were published.[14,15] Although the first junctions with NbN counterelectrodes did not have a T_c > 10K (counterelectrode gap energy > 1.8 eV at 4.2K), the results were promising enough that even a complete success with Mo-Re risked being overshadowed by the higher T_c of NbN.
- The earliest Mo-Re counterelectrodes fabricated and measured as part of Task 5 did not have a T_c > 10K within a coherence length of the barrier.

In light of these developments, more emphasis was placed on the much more difficult task of using high-T_c A15 compounds represented by Nb_3Sn (T_c = 18K).

3.4.2 Low-temperature growth

The only candidate material for low temperature formation of a counterelectrode was Mo-Re because its T_c was expected to be

relatively insensitive to disorder. In contrast, Nb_3Sn grown at < 500°C would be amorphous,[16] and not superconducting. In the composition range of 30 to 40 atomic percent Re, the stable Mo-Re phase is a bcc alloy with a T_c = 12K.[17] Mo-Re in this composition range has also been stabilized in the Mo_3Re A15 structure.[18] The highest T_c of 15K was obtained for 35 atomic percent Re, with the excess Re atoms occupying Mo sites. Higher T_c A15 materials such as Nb_3Sn exhibit a decrease in T_c for much smaller levels of antisite disorder.

The speculation that Mo-Re films, with T_c's as high as bulk samples, could be grown at low temperature was verified by the data in Figure 3.7a. Samples which were prepared by co-evaporation at 100°C, had a bcc structure and T_c values in agreement with the data of Ref. [17]. The electron-phonon coupling strength, $2\Delta/kT_c$, plotted in Figure 3.7b, was based on tunnel junction I-V curves (Pb counterelectrodes) similar to the one in Figure 3.5, but with higher subgap conductances. While resistive T_c measurements might preferentially measure a single high-T_c path, and tunneling measurements alone might preferentially sample the area or the surface with the lowest energy gap, a ratio as high as 3.5 and the sharp rise in the conductance of junctions observed at the gap voltage, indicated that the samples were homogeneous. Since $2\Delta/kT_c$ was not greater than 3.5, bcc-phase Mo-Re can be identified, for the first time, as a weak-coupling, BCS superconductor.

Efforts to stabilize the A15 phase were successful, but T_c values showed little increase over the bcc alloy. The onset of superconductivity was increased to 13.0K, but the resistive

Fig. 3.7 (a) Superconductive transition temperature of Mo-Re bcc alloys grown by co-evaporation at 100°C plotted as a function of composition and compared with data from bulk samples reported in Ref. 55. The error bars indicate 5% and 95% of the resistive transition. (b) The electron-phonon coupling strength plotted as a function of composition and compared with the weak-coupling, BCS value.

transitions were somewhat broader (1K wide) than for the alloy films. The A15 phase was found when films were deposited by co-evaporation at 1000°C in a pressure > 10^{-9} torr instead of the normal pressure of < 10^{-10} torr (the chamber had not been fully degassed). Postnikov et al. reported that the A15 phase was stabilized in Mo-Re films deposited by evaporation at 950° to 1300°C in a pressure of 10^{-6} torr.[19] Subsequent experiments tended to support the role of high temperature over impurity stabilization. For example, a series of films deposited at 800°C grew with a bcc lattice, and films grown in somewhat better vacuum (1 x 10^{-10} torr) at 1000°C were still A15. However, further experimental work was considered to be outside the scope of this program since the high temperatures needed to obtain the A15 phase obviated the advantages Mo-Re offered over Nb_3Sn.

Two additional developments concerning the A15 structure of Mo-Re should be noted. First, both the 800°C bcc alloy and 1000°C A15-structure films grew as single crystals on (11$\bar{2}$0) sapphire as observed by in-situ RHEED. The A15 film had a (100) growth direction, the same as observed in Nb_3Sn films grown on this orientation of sapphire.[20] The bcc film had a (110) growth direction, as in the case of bcc films of Nb grown on this orientation of sapphire.[21] The x-ray diffraction rocking-curve width of 0.3° for the latter film confirmed the quality of the crystal. Secondly, the normal-state resistivity at 15K, as plotted in Figure 3.8, was a good indicator of crystal structure. It was nearly independent of composition for the bcc films, as expected for an alloy. However, the resistivity was 3 to 6 times higher and varied with composition for the A15 compound.

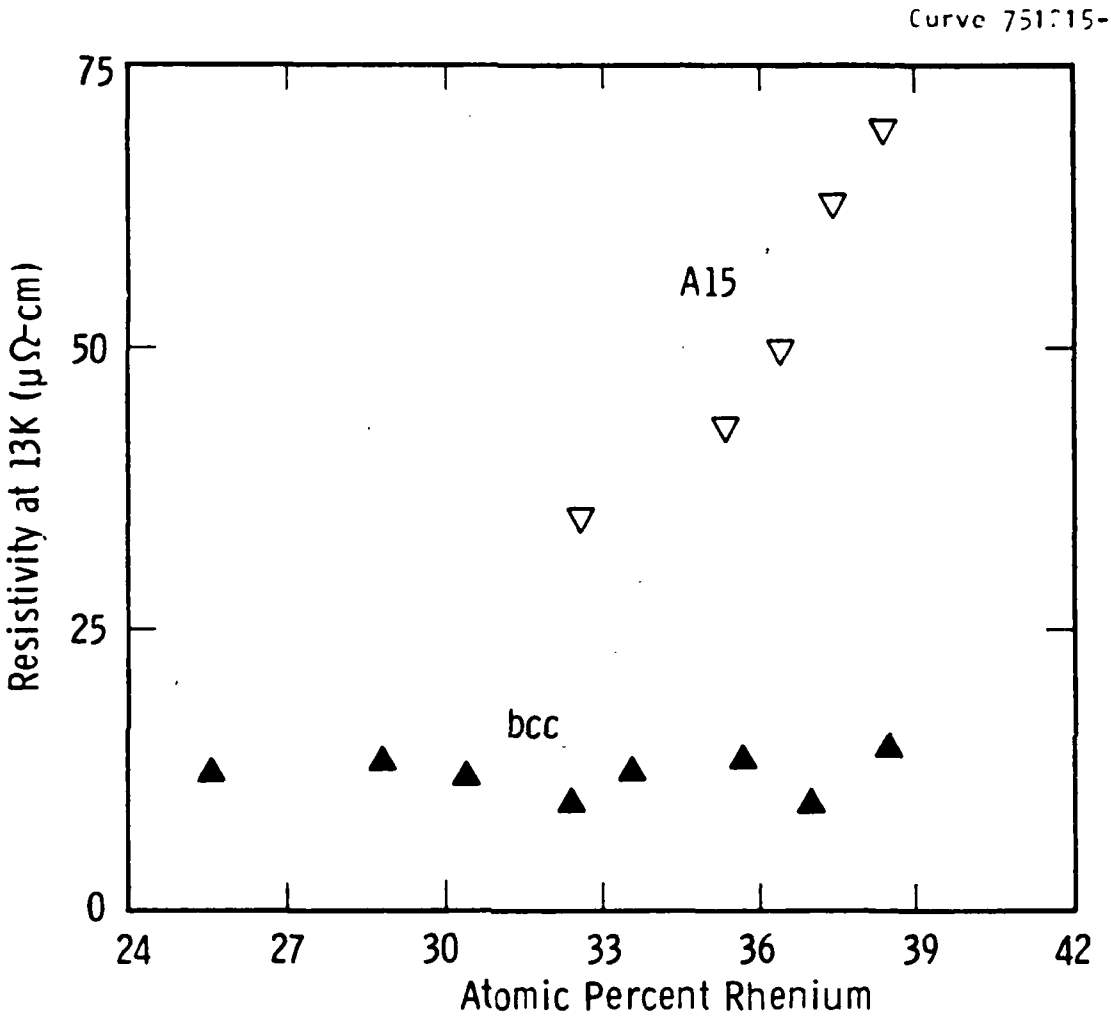

Fig. 3.8 The normal-state resistivity of Mo-Re bcc-alloy and A15-compound films measured just above the superconductive transition temperature.

Achieving a T_c equivalent to bulk samples in thick films at low temperature does not indicate whether the full T_c can be obtained within a coherence length of the barrier/counterelectrode interface. The limitation is less serious for Mo-Re than for high-T_c A15 compounds because the coherence length for Mo-Re is approximately 20 nm compared to 3 nm for Nb_3Sn. Films as thin as 20 nm were grown on sapphire to simulate the material formed in the first coherence length of the counterelectrode.

The results of T_c and resistivity ratio, $\rho_n(300^\circ C)/\rho_n(15^\circ C)$, measurements on evaporated and dc-magnetron-sputtered films, are shown in Figure 3.9 as a function of film thickness. The sputtered films had much lower T_c and resistivity ratios for thin films than for films > 100 nm thick. The evaporated films, grown in a lower background pressure, showed a negligible change in these properties between 20 nm and 100 nm thickness. The only caveat concerning the use of the evaporated films for counterelectrodes came from the RHEED patterns reproduced in Figure 3.10. The pattern in Figure 3.10a shows diffuse rings characteristic of a highly-disordered 20 nm-thick film. Figure 3.10b shows that the 100 nm thick film exhibited a pattern characteristic of polycrystalline films with some texturing. For comparison, a RHEED pattern of an A15 Mo-Re single crystal is reproduced in Figure 3.10c. The disorder in the 20 nm thick polycrystalline Mo-Re shown in Figure 3.10a, suggested that a film grown at 100°C on a substrate which was less favorable to epitaxial growth than sapphire might be amorphous, and thus posess a depressed energy gap.

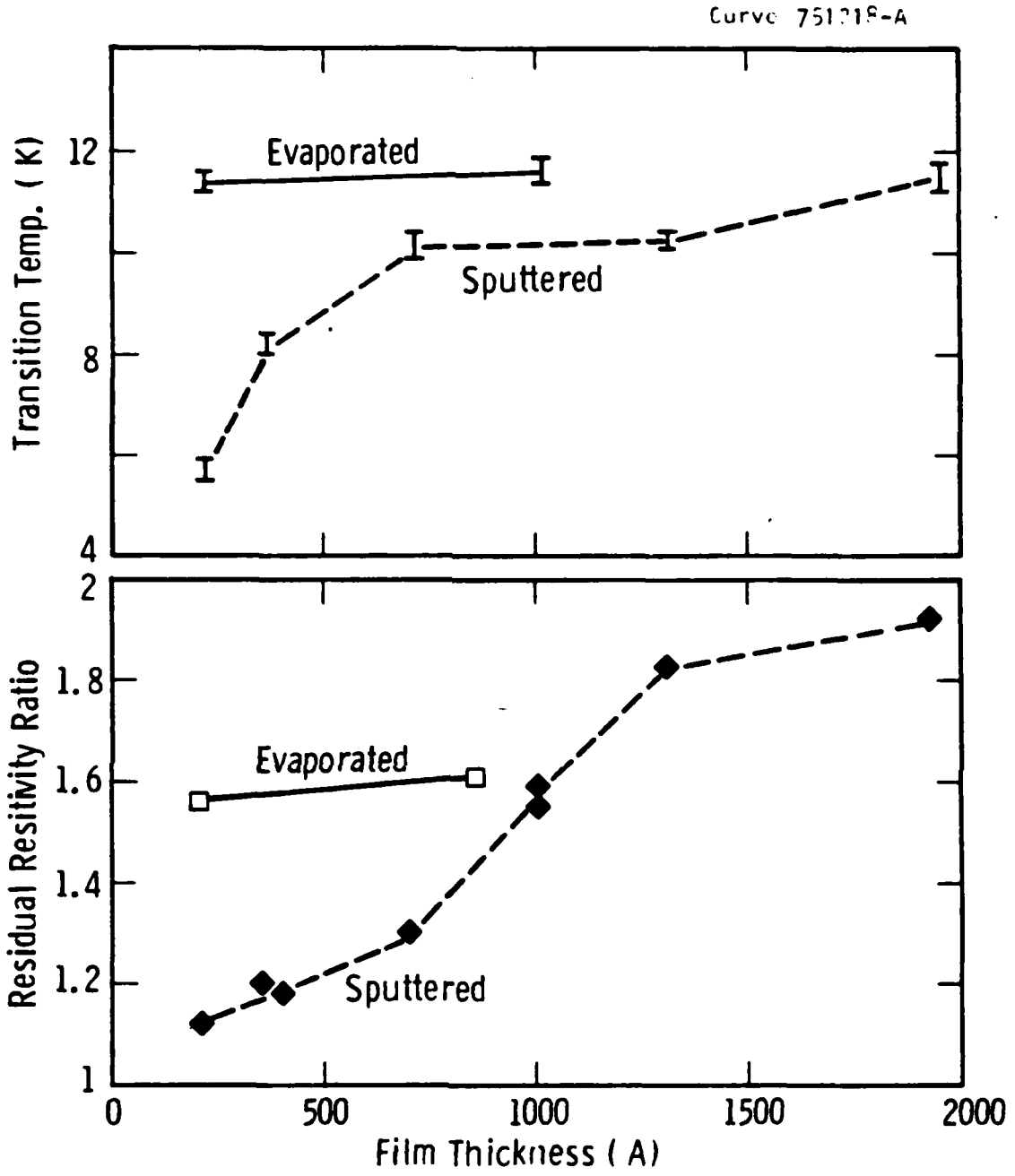

Fig. 3.9 A comparison of the properties of sputtered and evaporated Mo-Re (approximately 35 at. % Re) alloy superconductors as a function of film thickness. (a) Transition temperature and (b) Resistivity ratio, $\rho_n(300^\circ C)/\rho_n(15^\circ C)$.

$Mo_{65}Re_{35}$ – 9 kV RHEED

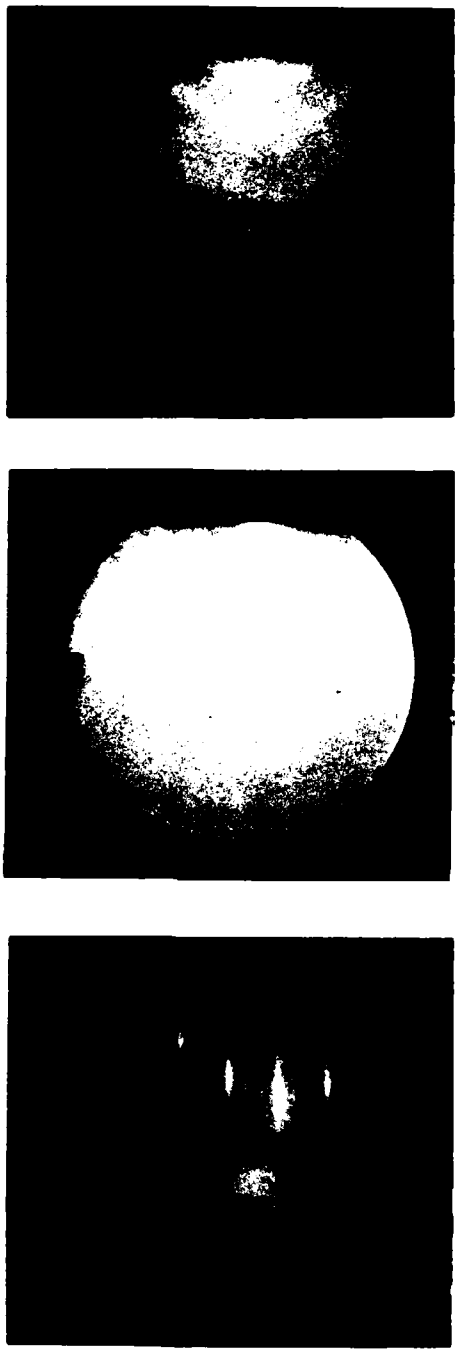

Fig. 3.10 <u>In-situ</u> RHEED patterns of Mo-Re films. (a) Diffuse rings characteristic of randomly-oriented, highly-disordered grains in a thin film grown at low temperature. (b) Pattern characteristic of a polycrystalline film with some texture. (c) Sharp lines indicated that the film was a relatively smooth (two-dimensional reciprocal lattice) single crystal.

The reaction of Mo-Re surfaces with oxygen was mentioned in Section 3.3.3 in connection with the sealing of barrier pinholes with the native oxide. However, for the barrier/counterelectrode interface, it would be better to have a superconductor that does not react with oxygen. Figure 3.11 shows that a Mo-Re surface protected by an Al overlayer has nearly the same XPS spectra for Re_{4f} and Mo_{3d} photoelectrons as a Mo-Re surface exposed to air for several months. The fraction of photoelectrons with a chemical shift indicative of the oxides of Re and Mo, corresponded to a thickness of the oxide of approximately 0.2 nm for the exposed surface. For comparison, single-element films of Re and Mo were grown and exposed to air for two months. The Re oxide grew to a thickness of 0.6 nm and the Mo oxide to approximately 7 nm. This indication of the chemical stability of Mo-Re relative to other high-T_c superconductors was not fully exploited since a decision had been made to form Mo-Re counterelectrodes only at low temperatures where chemical reaction was less likely to occur.

3.4.3 High-temperature growth

A fundamental concern with regard to high temperature processing of tunnel junctions is that the barrier material might diffuse into, or react with, one of the electrodes, as discussed in Section 3.1. Thus the emphasis in this program on refractory oxides which do not form stable suboxides at the processing temperatures. As part of Task 1, XPS measurements of Nb/oxidized-Al bilayers were made at temperatures up to 750°C (Section 3.1) without apparent damage to the Al_2O_3. The same measurements on NbN/oxidized-Al bilayers (Appendix A) also showed no change in

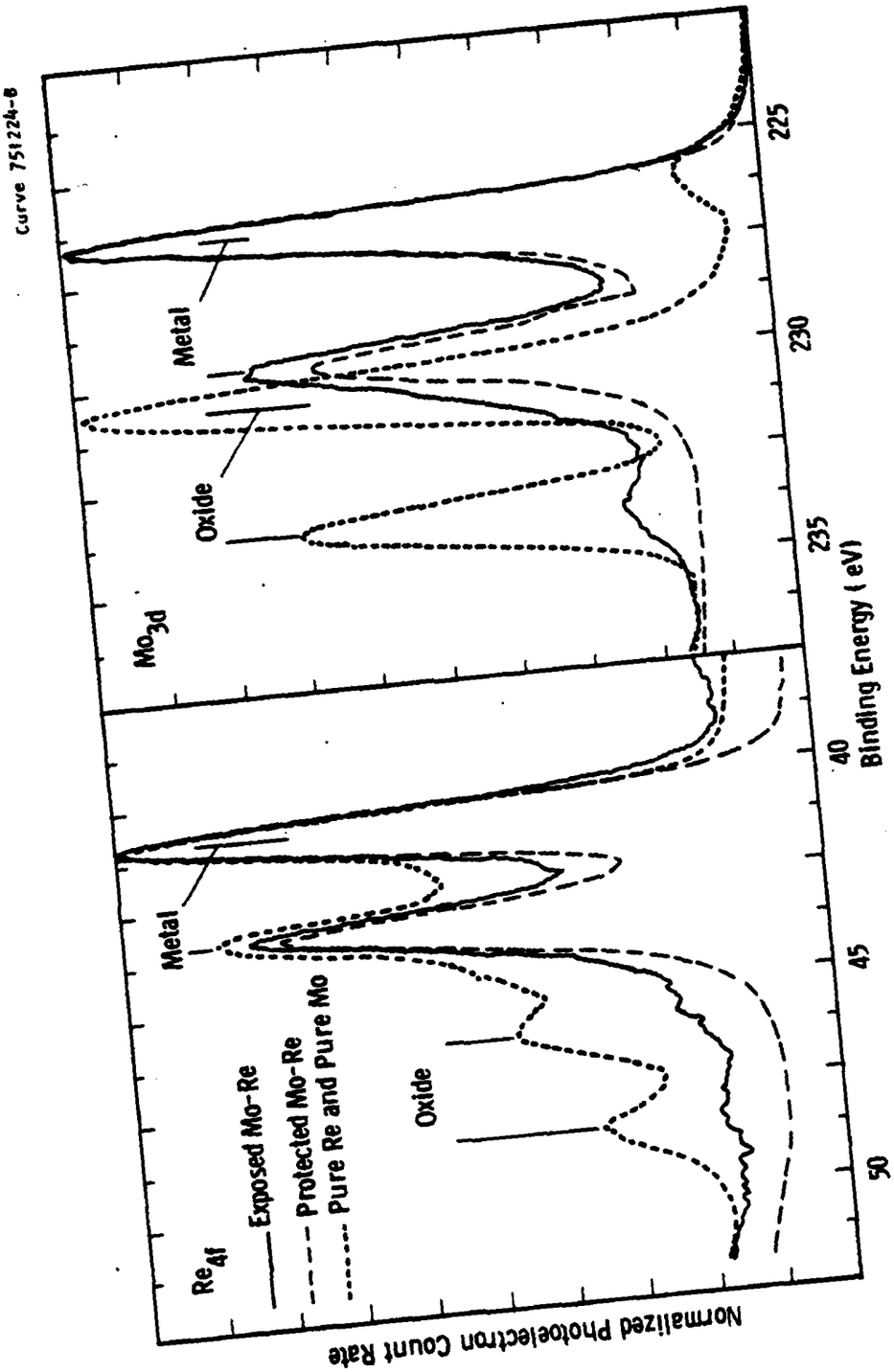

Fig. 3.11 XPS data for (a) Re_{4f} and (b) Mo_{3d} photoelectrons. The "exposed" Mo-Re, pure Re, and pure Mo films were measured after long-term oxidation in air. The "protected" Mo-Re had an overlayer of Al 2.0 nm thick deposited immediately after the Mo-Re film and without breaking vacuum.

the Al_2O_3 up to 850°C. If diffusion into these base electrodes had been observed, a clear upper limit to the processing temperature would have been established.

Several experiments were performed to look for diffusion or chemical reduction at the barrier/counterelectrode interface at high temperatures. A layer of Nb_3Sn 7.5 nm thick was evaporated on $(11\bar{2}0)$ sapphire at 850°C and on an oxidized Al underlayer at both 850°C and 925°C. *In situ* XPS was used to look for reduction of the Al_2O_3 by Nb or Sn. Since the coherence length of Nb_3Sn is only 4 nm, XPS could be used to study the substrate/film interface even for a film twice as thick as the coherence length.

As an example of the technique, Figure 3.12a shows the four major photoelectron peaks from the sample for which interdiffusion was most likely, the Nb_3Sn film grown on oxidized Al at 925°C. The two Al_{2p} peaks are from Al_2O_3 and from metallic Al under the oxide. The Nb_{3d} and Sn_{3d} peaks are $3d_{3/2}$ and $3d_{5/2}$ spin doublets which indicated that only metallic Nb and Sn were present. Figure 3.12b shows more detail of the Nb_{3d} spectrum. The chemical shift of photoelectrons from Nb atoms in Nb_2O_5 is 5.0 eV. Therefore, one can say with certainty that no Nb_2O_5 was present. However, NbO has a shift of only 1.0 eV so the presence of some NbO could be masked by the large number of counts from the Nb_3Sn. Nevertheless, no evidence of interdiffusion or reaction could be found with XPS, even at 925°C.

The reason for wanting to deposit Nb_3Sn counterelectrodes at > 900°C is to take advantage of "composition locking".[22] Figure 3.13 is a plot of the composition of Nb-Sn films deposited at three temperatures without rotation of the substrate holder, i.e.

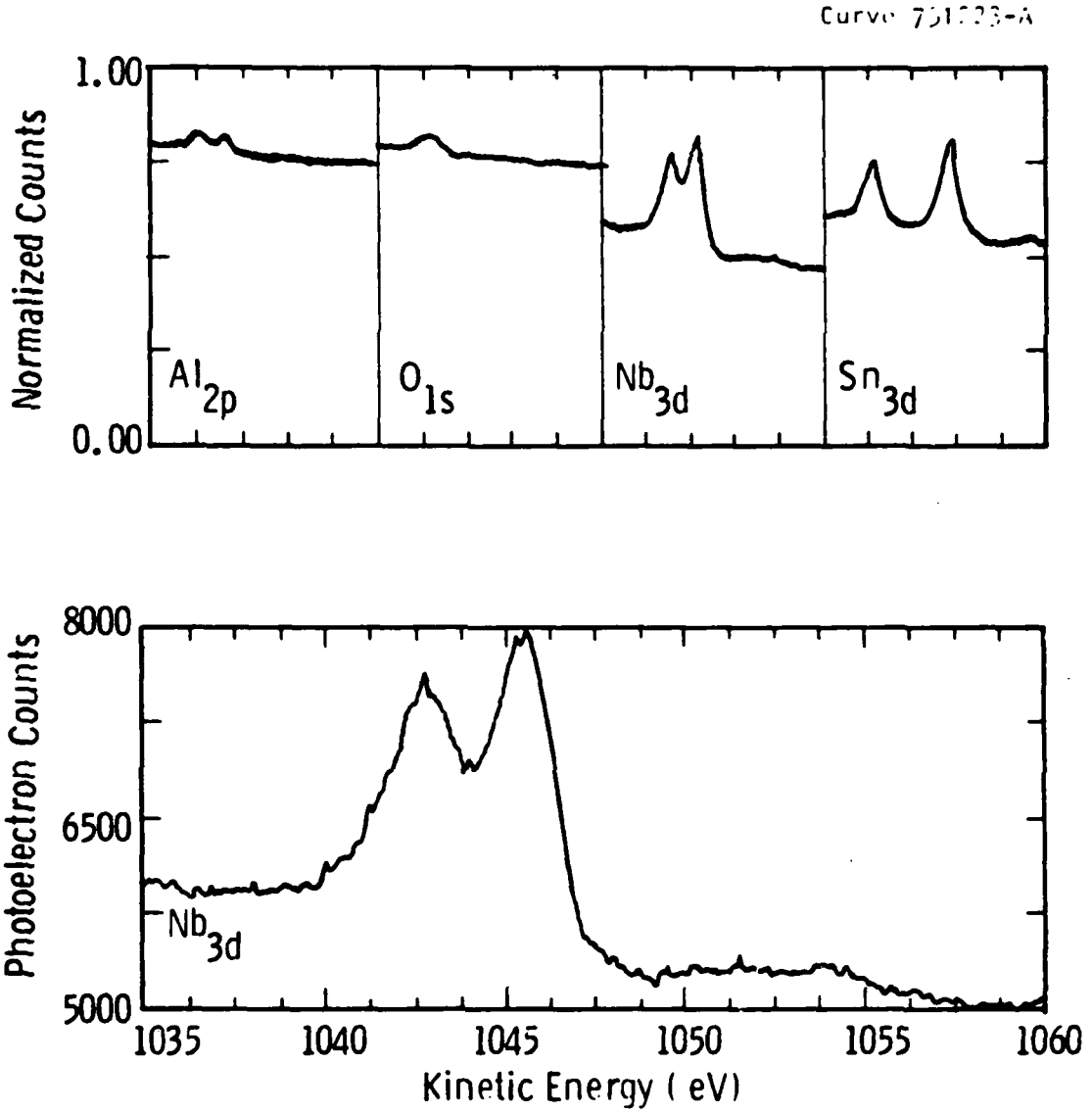

Fig. 3.12 XPS spectra recorded <u>in situ</u> for a 7.5 nm-thick Nb_3Sn film deposited on an oxidized Al film at 925°C. (a) Spectra of photoelectrons with four different kinetic energies. (b) The expanded Nb_{3d} photoelectron peak shows no chemical shift and, therefore, no indication of a reaction with the oxidized Al.

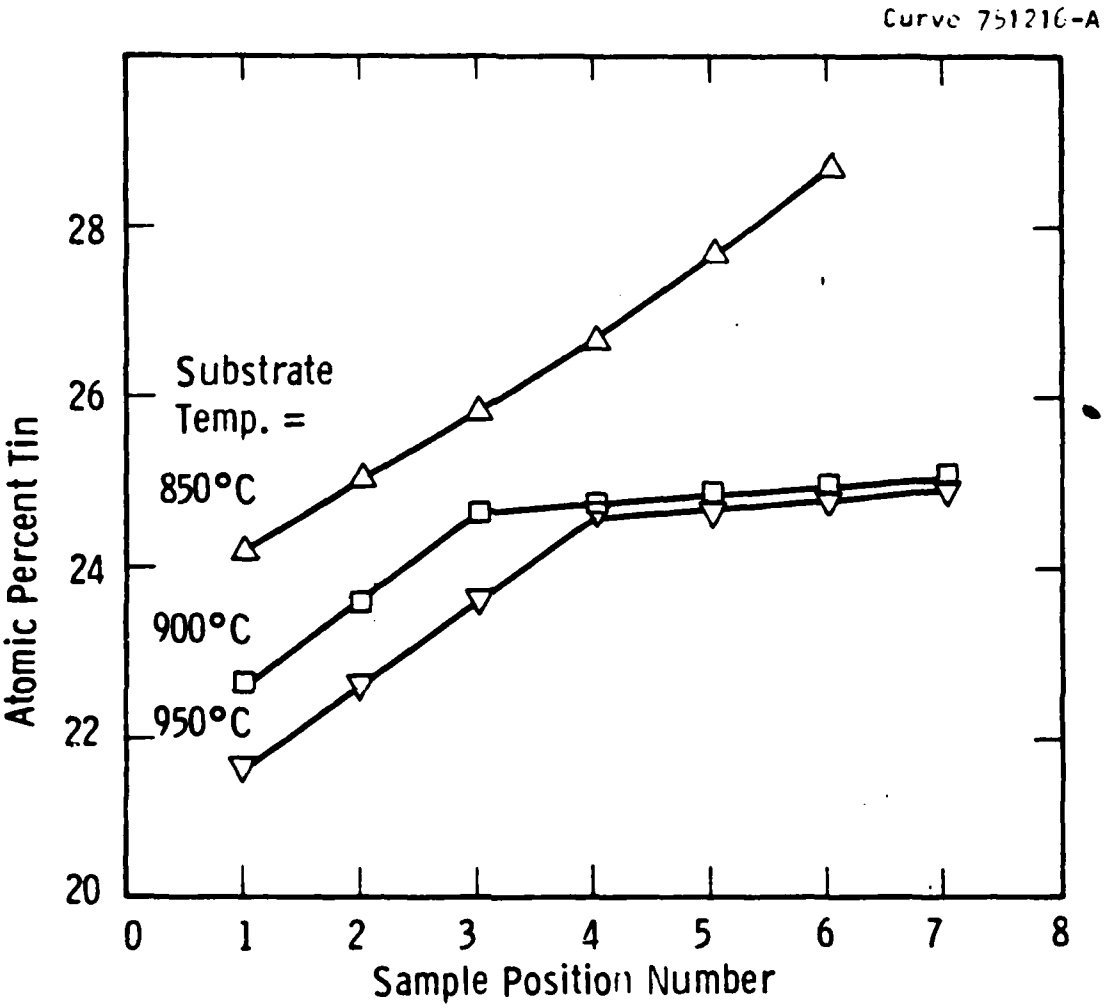

Fig. 3.13 Composition of Nb_3Sn co-evaporated films as a function of sample position on a block which was not rotated during deposition. The "composition-locking" observed for substrate temperatures > 850°C was due to re-evaporation of tin from the Nb_6Sn_5 phase.

the "phase spread" configuration. Samples 4 to 7 deposited at 850°C have an excess of tin that remains in the film as a Nb_6Sn_5 phase. Samples 4 to 7 deposited at > 900°C have exactly 25 atomic percent tin and are single-phase A15 films because the excess tin re-evaporates.

One way to ensure that only the A15 phase formed was to make samples with < 25 atomic percent tin. The drawbacks of that approach are lower and broader T_c's. Figure 3.14 shows a comparison of the T_c of Nb_3Sn samples deposited at Westinghouse with the midpoints of the superconductive transitions of samples evaporated at Stanford.[22] By using heat capacity measurements, Hellman et al. have shown that the Stanford films had T_c's as broad as the single-crystal Westinghouse films and speculated that it was because the off-stoichiometry samples were polycrystalline.[23] The large transition width for the off-stoichiometry Westinghouse films appears to be the result of two factors related to the current limitations of the SDAF:

- Fluctuations in the Nb evaporation rate were large (±5%) because a fast-response rate control technique for electron-beam evaporation developed by Hammond has not been fully implemented.[24]
- The relatively slow sample rotation (20 rpm), compared to the deposition rate, resulted in fluctuations in compositions of up to 7 atomic percent tin (for edge samples) with a periodicity of approximately 2 nm in the growth direction.

The results of T_c measurements of the 7.5 nm-thick Nb_3Sn films indicated that at 925°C there probably was some interdiffusion which could not be detected by XPS. At 850°C, the films on

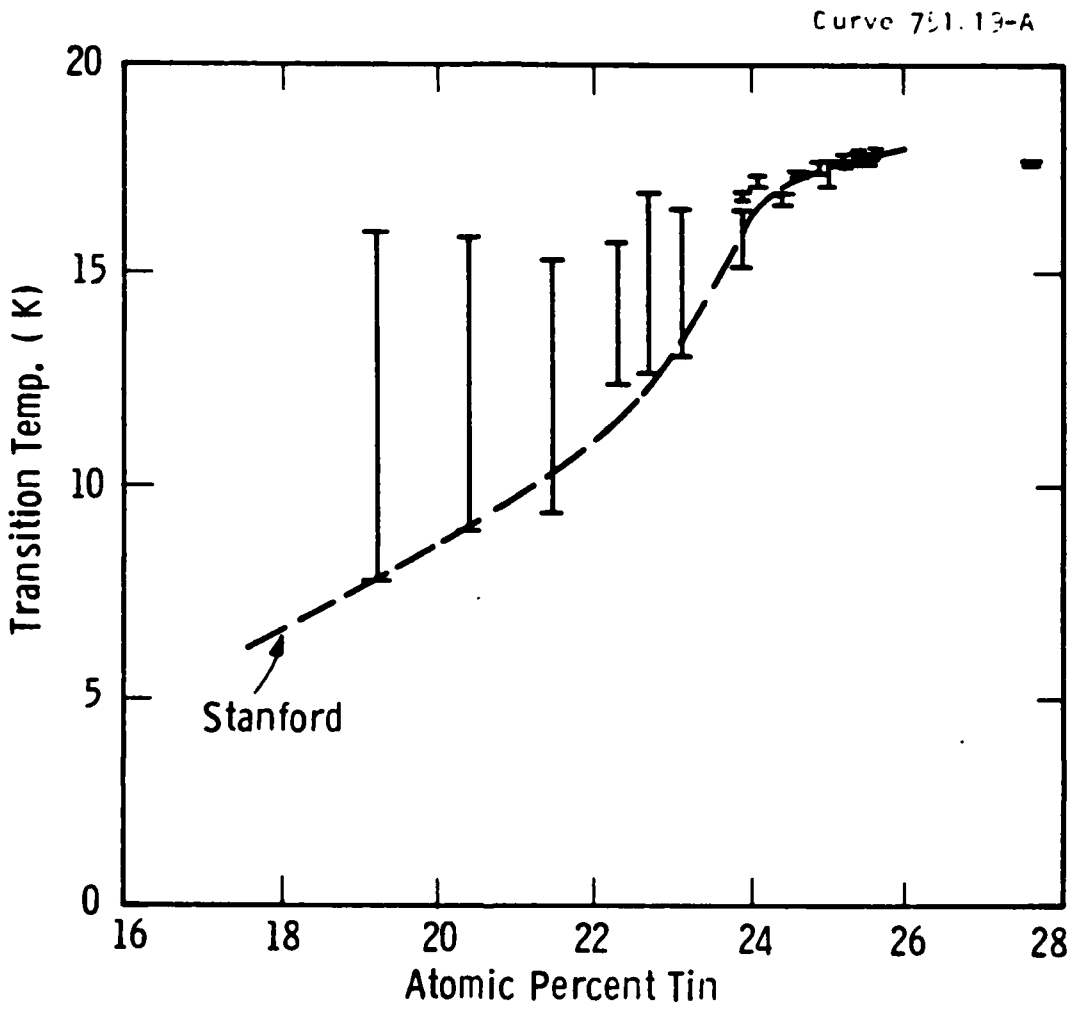

Fig. 3.14 The superconductive transition temperature for co-evaporated Nb_3Sn films in the range of composition below the "composition-locked" phase boundary at 25 at. % Sn. The comparison with Stanford data (Ref. 56) shows the need for fast-response Nb rate control.

sapphire had T_c = 12.0-9.9K (5% and 95% of the transition). The films grown on oxidized Al had T_c = 11.5-7.0K. The relatively low T_c's were expected because the films contained < 25 at.% Sn (probably 22-23 at.%) to ensure that they were single-phase. The difference between the results on the two types of substrates was small enough to be explained by the fact that one grew as a single-crystal and the other had a randomly-oriented polycrystalline morphology. However, the films grown on oxidized Al at 925°C were expected to have a higher T_c because composition-locking was used to obtain 25 at.% Sn. Instead, the T_c's were very broad with 5% of the transition at 9.5K and the midpoint < 4.2K. The decrease was presumably due to contamination from the oxidized Al substrate.

The conclusions drawn from the experiments with thin Nb_3Sn films grown at high temperatures were:

1. The upper temperature limit for the growth of Nb_3Sn counterelectrodes on polycrystalline Al_2O_3 tunnel barriers is less than the temperature needed for composition-locking.

2. XPS was insufficiently sensitive to detect the reaction between a thin superconductive overlayer and a barrier. The reaction was significant enough to result in a decreased T_c and is assumed to be detrimental to barrier integrity.

3. Nb_3Sn counterelectrodes should be grown with < 25 at.% Sn to ensure that they are single-phase A15 films. However, improvements are needed in deposition rate control and uniformity in composition across the substrate, if a high-T_c junction with a sharp gap is to be attained. The highest T_c

obtained for a single-phase, Nb-rich film was 12-10K in a thickness twice the coherence length.

3.4.4 Counterelectrode formation by solid-state reaction

A hybrid approach to Nb_3Sn counterelectrodes was considered which combined low-temperature deposition and high-temperature annealing to form the A15 phase. The background experiments for this approach, reported in Ref. [25], were performed as part of the AFOSR program in an effort to understand the formation of stable A15 compounds.

It was established that A15 Nb_3Sn would form by annealing amorphous Nb-Sn at temperatures as low as 650°C on a polycrystalline oxide substrate. The specific approach was to first fabricate and test an S-I-N junction, and then to anneal the sample in a number of steps at progressively higher temperatures. The results of the fabrication and testing of junctions formed by all three of the approaches which were developed, are given in Section 3.5.

3.4.5 Conclusions from Task 4

Three approaches to the formation of a counterelectrode for a high-T_{op} junction were developed. Conclusions regarding the implementation of each approach are listed below.

1. Low-temperature growth of Mo-Re counterelectrodes: bcc-alloy films with a T_c = 12K can be grown within a coherence length of a sapphire substrate at 100°C even though the first 20 nm of the film are highly-disordered.

2. High-temperature growth of Nb_3Sn counterelectrodes: The

temperature or deposition on oxidized Al must be lower than the phase-locking temperature. Improved control over fluctuations in composition is needed so that single-phase films can be obtained without significantly reducing the T_c. Alternatively, a different barrier must be formed to permit Nb_3Sn phase-locking without any barrier/counterelectrode interaction.

3. Low-temperature deposition of Nb-Sn followed by annealing: This approach involves the implicit assumption that refractory counterelectrodes can be formed at low temperatures as normal conductors without damage to the barrier. Then, formation of a high-T_c superconductor by solid-state reaction can be monitored.

3.5 Task 5 - Fabrication and Testing of High-T_{op} Junctions

3.5.1 Objective

Task 5 was to be an integration of the other four tasks pending the development of a promising approach in Task 4. The two approaches described in the last section which involved low-temperature counterelectrode deposition were tested.

3.5.2 Mo-Re junctions

Figure 3.15 shows an I-V curve for a Mo-Re / oxidized-Al / Mo-Re tunnel junction measured at 4.2K. The evaporated Al layer for the barrier was exceptionally thick, 6.0 nm. Only the top 2.0 nm oxidized. These were probably the lowest-leakage of the all-Mo-Re junctions because the thick Al overlayer covered completely. However, the unoxidized Al was also the most likely cause of the large "knee" in the I-V curve just below the gap voltage.

The I-V curve was measured as a function of temperature for this set of Mo-Re junctions. The "junction T_c" was approximately 8K. The Mo-Re counterelectrode had been evaporated in a pressure of 4×10^{-10} torr at 100°C. Although a RHEED pattern of the top surface of the 60 nm-thick counterelectrode showed a series of rings from a polycrystalline film, the first 20 nm must have been at least as disordered as the 20 nm films grown on sapphire. In view of the RHEED pattern of Figure 3.10a, and the T_c of the junction, we believe that the material within the first coherence length of the barrier/counterelectrode interface was amorphous. The T_c of amorphous Mo-Re can be as high as 9K.[26]

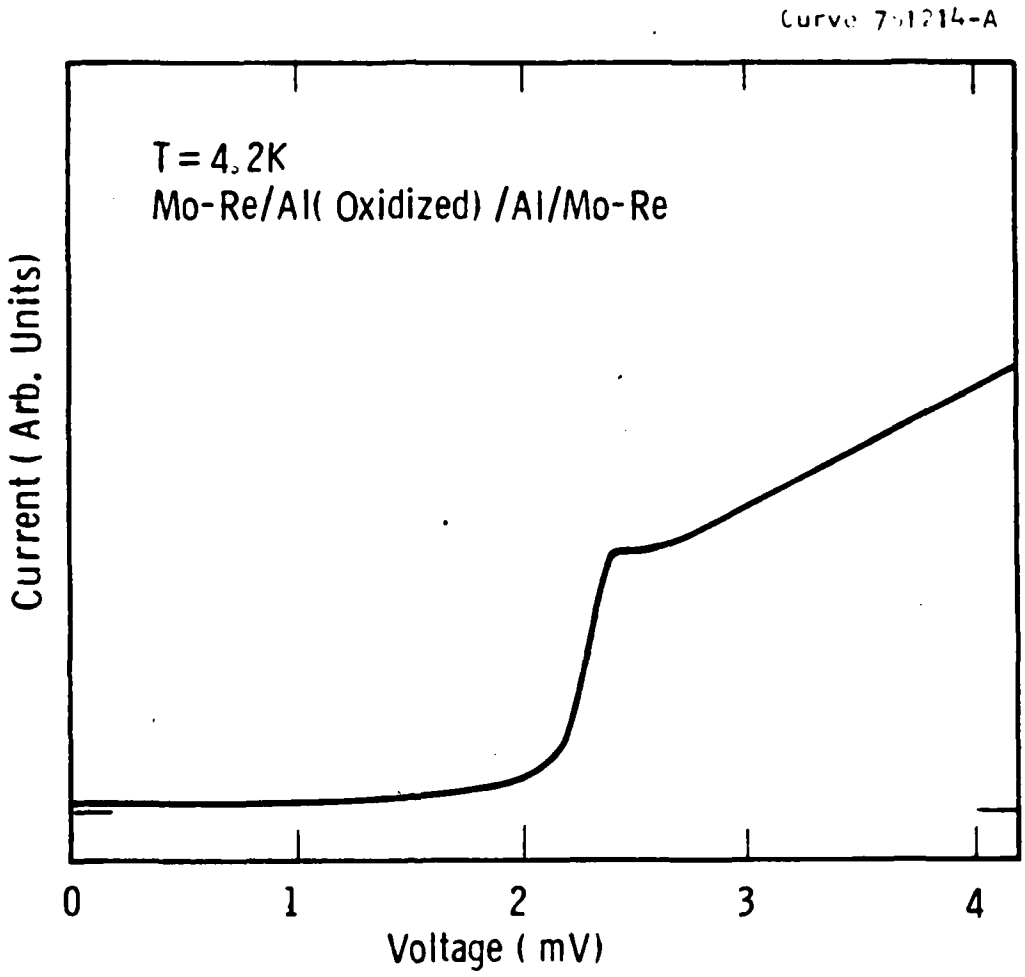

Fig. 3.15 Tunneling I-V curve for a Mo-Re / oxidized Al / Mo-Re junction measured at 4.2K. The gap voltage of the counterelectrode corresponded to a T_c = 8K.

3.5.3 Nb-Sn junctions

The Nb-Sn counterelectrodes which were tested, grown on either Nb_3Sn or NbN base electrodes, were deposited at relatively low temperatures. The resulting junctions, expected to be S-I-N junctions until high-temperature annealing was completed, invariably had very high subgap conductance and were often completely shorted. In almost every case, the problem appeared to be related to poor coverage by a barrier which, based on Pb reference junctions (Task 3) and analytical criteria developed in Task 1, appeared to cover the base electrode. In each of these cases, oxidized Al, Y, Mg, Si, and rf-sputtered MgO, it was necessary to return to Tasks 1 and 3 for modifications to the process of barrier formation.

The exceptions to the problems with poor coverage were the ion-milled barriers. In particular, the Al_2O_3 formed by ion-beam oxidation (Appendix D) for the AFOSR program, provided adequate coverage on either NbN or Nb_3Sn base electrodes. Counterelectrodes of NbN or Pb deposited on Nb_3Sn/ion-beam oxidized Al bilayers formed low-leakage junctions at zero bias (I-V curve in Appendix A). However, the subgap conductance increased sharply above the NbN or Pb gap due to damage to the Nb_3Sn from the 300 V $Ar-O_2$ ion beam. The ion-beam oxidized Al and Mg barriers are now used exclusively for NbN base electrodes which are less sensitive to disorder in the surface layer than Nb_3Sn.

3.5.4 Conclusions from Task 5

The following conclusions were drawn from the testing of tunnel junctions made with counterelectrodes of high-T_c supercon-

ductors:

1. Mo-Re counterelectrodes films grown at low temperature were amorphous for the first 20 nm and thus had a T_c of only 8K. To obtain crystalline material in the first layer deposited, either the deposition temperature must be raised, or an epitaxial substrate, such as sapphire, must be simulated by the tunnel barrier.

2. Nb-Sn counterelectrodes cannot be fabricated at this time, even at low temperature. However, the current problem results from the properties of the tunnel barrier rather than from the counterelectrode deposition.

3. NbN tunnel junctions are the only high-T_{op} junctions that can be made given the current status of tunnel barrier development.

4. CONCLUSIONS

Detailed conclusions specific to each task are given in subsections at the end of each corresponding part of Section 3. Below are given conclusions from all five tasks that are believed to be most the important.

1. Oxidized metallic overlayers of Al are capable of protecting the Nb and A15 Nb_3Sn base electrode from oxidation and the resulting degradation of gap voltage. The Mo-Re surface does not oxidize readily.

2. The Al/Al-oxide barrier is more suitable than the Y/Y_2O_3 barrier due to lesser self-limited oxide thickness and better wetting properties.

3. The Al/Al-oxide layer can withstand heating up to 750°C without disintegration and is, therefore, a promising candidate for high-temperature junction fabrication processes. Electrical performance of barriers heated above 300°C remains to be evaluated.

4. The single most important cause of high subgap conductance and of junction shorts or microshorts is the non-uniform coverage of the base by the overlayer. Rough base surfaces result in a less uniform coverage.

5. The native oxides of Nb_3Sn (mostly the Sn-oxide) are more effective in plugging the pinholes due to nonuniform coverage than is the native Nb-oxide.

6. Nearly ideal I-V junction characteristics were obtained using the Al/Al-oxide barrier on Nb, Mo-Re and Nb_3Sn surfaces but only in the case of Pb, Pb-Bi and Mo-Re electrodes.

7. Barrier crystallinity and texture do not enhance the subgap leakage current in the case of soft counterelectrodes. The results with refractory counterelectrodes did not permit any firm conclusion on the effect of the barrier crystallinity.

8. Hard (refractory) Mo-Re bcc alloy counterelectrode deposited at low temperature on thermal Al-oxide did not attain gap voltages higher than those of Nb. This was probably due an amorphous layer within a coherence length from the barrier.

9. High-T_c A15 counterelectrodes were not demonstrated since all A15 films deposited on Al/Al_2O_3 and MgO barriers resulted in shorts or microshorts. The main goal of this project, therefore, was not attained. In contrast, high-T_c NbN counterelectrodes were formed successfully on similar barriers.

10. The main reason for the failure to obtain high-T_c A15 counterelectrodes is believed to be the insufficiently uniform coverage of the base by the metal/oxide or oxide

overlayer, combined with the electrochemical interaction between the barrier and counterelectrode atoms. This problem is, in-part, process- and equipment-related, and can be solved.

11. The approach to high-T_c counterelectrode and high T_{op} junction fabrication remains to be that of ordered, epitaxial growth of the counterelectrode on a crystalline barrier conforming to the high-T_c base structure. Correctness of this approach was demonstrated for NbN/MgO/NbN epitaxial tunnel junctions having sumgap voltages exceeding 5 mV at 4.2 K. High processing temperatures, up to 920°C, will be necessary, however, to implement this approach in all-Nb_3Sn junctions. For other high-T_c A15 compounds the processing temperatures will also be high.

12. High-operating-temperature junctions with NbN or NbCN counterelectrodes represent the only short-term option available. The use of A15, high-T_c base electrodes is possible if clear advantages are indicated.

5. ACKNOWLEDGEMENTS

The authors acknowledge the collaboration with R. D. Blaugher and J. Buttyan in the area of junction patterning and fabrication. They are also indebted to H. C. Pohl for his assistance in film sputtering and T_c measurements.

6. REFERENCES

1. J. Talvacchio, A. I. Braginski, J. R. Gavaler, M. A. Janocko, A. S. Manocha and R. D. Blaugher, Thin Film Technology of High-Critical-Temperature Superconducting Electronics, First Annual Report under ONR Contract No. N00014-82-C-0617, December 1983.

2. J. Talvacchio, A. I. Braginski and M. A. Janocko, Thin Film Technology of High-Critical-Temperature Superconducting Electronics, Second Annual Report under ONR Contract No. N000-82-C-0617, December 1984.

3. L. J. van der Pauw, "A Method of Measuring Resistivity and Hall Effect on Discs of Arbitrary shape", Philips Res. Repts 13, 1 (1958).

4. V. Ambegaokar and A. Baratoff, "Tunneling Between Superconductors," Phys. Rev. Lett. 10, 486 (1963) and erratum 11, 104 (1963).

5. H. Ihara, Y. Kimura, H. Okumura, K. Senzaki and S. Gonda, "Oxidation Mechanism of the Surface of A15 Superconductors," in Adv. Cryo. Eng., A. F. Clark and F. P. Reed, editors, vol. 30 - Materials, p.589, Plenum (1984).

6. J. Kwo, G. K. Wertheim, M. Gurvitch and D. N. E. Buchanan, "X-ray Photoelectron Study of Surface Oxidation of Nb/Al Overlayer Structures", Appl. Phys. Lett. 40, 675 (1982).

7. J. M. Rowell, M. Gurvitch and J. Geerk, "Modification of Tunneling Barriers on Nb by a Few Monolayers of Al", Phys. Rev. B 24, 2278 (1981).

8. M. Gurvitch and J. Kwo, "Tunneling and Surface Properties of Oxidized Metal Overlayers on Nb", in Adv. Cryo. Eng. (A. F. Clark and R. P. Reed, eds.), vol. 30, p. 509 (1984).

9. A. R. Miedema and F. J. A. den Broeder, "On the Interfacial Energy in Solid-Liquid and Solid-Solid Metal Combinations," Z. Metallkunde 70, 14 (1979).

10. H. Kroger, L. N. Smith, and D. W. Jillie, "Selective Niobium Anodization Process for Fabricating Josephson Tunnel Junctions," Appl. Phys. Lett. 39(3), 280 (1981).

11. M. Gurvitch, M. A. Washington, H. A. Huggins, and J. M. Rowell, "Preparation and Properties of Niobium Josephson Junctions with Thin Al Layers," IEEE Trans. Magn. MAG-19(3),

791 (1983).

12. M. Ronay and E. E. Latta, "Interaction of Nb Counterelectrodes with Aluminum Oxide and Rare-earth Oxide Tunnel Barriers," Phys. Rev. B 27, 1605 (1983).

13. J. Halbritter, "Potential Barrier Model Incorporating Localized States Explaining Tunnel Anomalies", J. Appl. Phys. 58, 1320 (1985).

14. S. Kosaka, A. Shoji, M. Aoyagi, F. Shinoki, S. Tahara, H. Oniyasni, H. Nakagawa, S. Takada, and H. Hayakawa, "An integration of all-refracrory Josephson logic LSI circuit," IEEE Trans. Magn. MAG-21(2), 102 (1985).

15. E. J. Cukauskas and M. Nisenoff, "All-refractory high-Tc Josephson device technology," to be published in Advances in Cryogenic Engineering - Materials, edited by A. F. Clark and R. P. Reed (Plenum, New York, 1986)

16. R. H. Hammond, private communication.

17. R. D. Blaugher, A. Taylor, and J. K. Hulm, "The Superconductivity of Some Intermetallic Compounds," IBM J. of Res. and Dev. 6(1), 116 (1962).

18. J. R. Gavaler, M. A. Janocko, and C. K. Jones, "A15 Structure Mo-Re Superconductor," Appl. Phys. Lett. 21(4), 179 (1972).

19. V. S. Postnikov, V. V. Postnikov, and V. S. Zheleznyi, "Superconductivity in Mo-Re system alloy films produced by electron beam evaporation in high vacuum," Phys. Status Solidi A 39, K21 (1977).

20. J. R. Gavaler, A. I. Braginski, M. A. Janocko, and J. Talvacchio, "Epitaxial Growth of High-T_c Superconducting Films," presented at the International Conference on the Materials and Mechanisms of Superconductivity, Ames, Iowa, May, 1985.

21. S. M. Durbin, J. E. Cunningham, and C. P. Flynn, "Growth of single-crystal metal superlattices in chosen orientations," J. Phys. F: Met. Phys. 12(1), L75 (1982).

22. D. A. Rudman, F. Hellman, R. H. Hammond, and M. R. Beasley, "A15 Nb-Sn Tunnel Junction Fabrication and Properties," J. Appl. Phys., 55(10), 3544 (1984).

23. F. Hellman, J. Talvacchio, T. H. Geballe, and A. F. Marshall, "A new look at the growth of thin films of Nb-Sn," to be published in Advances in Cryogenic Engineering - Materials, edited by A. F. Clark and R. P. Reed (Plenum, New York, 1986).

24. R.H. Hammond, "Electron Beam Evaporation Synthesis of A15 Superconducting Compounds: Accomplishments and Prospects," IEEE Trans. Magn. MAG-11(2), 201 (1975).

25. A. I. Braginski, J. R. Gavaler, and K. Schultze "Formation of A15 phase in epitaxial and polycrystalline Nb-Sn and Nb-Al diffusion couples," to be published in Advances in Cryogenic Engineering - Materials, edited by A. F. Clark and R. P. Reed (Plenum, New York, 1986).

26. M. M. Collver and R. H. Hammond, "Superconductivity in amorphous transition-metal alloy films", Phys. Rev. Lett. 30(3), 92 (1973).

APPENDIX A

UHV DEPOSITION AND IN-SITU ANALYSIS OF THIN-FILM SUPERCONDUCTORS

J. Talvacchio, M. A. Janocko, J. R. Gavaler,
and A. I. Braginski

Westinghouse R&D Center
Pittsburgh, Pennsylvania

ABSTRACT

The application of a UHV deposition and surface analysis facility to the fabrication of high-transition-temperature superconducting films for studies of epitaxial growth and development of refractory tunnel junctions is discussed. A description is given of the vacuum system with some detail of the chambers used for co-evaporation and reactive dc magnetron sputtering. Specific examples presented to illustrate the effect of MBE-like deposition conditions, and the role of RHEED, XPS, and, to a lesser extent, other surface-sensitive probes, are: (a) the preparation of clean and damage-free sapphire and Nb_3Ir substrates, (b) the epitaxial relationships in a number of superconductor-insulator systems such as sapphire and NbN, Nb_3Sn, and Mo-Re, (c) the development of CaF_2 and ion-beam oxidized Al and Mg tunnel barriers, and (d) the deposition of refractory counterelectrodes. Correlations are made with tunneling characteristics for appropriate examples.

INTRODUCTION

The fundamental aspects of Molecular Beam Epitaxy (MBE) have been established in the study of semiconductor thin films. We have attempted to prepare and characterize superconductor films in an analogous fashion. Some similarities to the growth of semiconductor films by MBE which are desirable are:

1. The use of single-crystal subatrates with surfaces that are characterized with respect to structure (periodicity), composition, and contaminants.

2. Low (< 0.1 nm/sec) deposition rates without having film properties dominated by background impurities which are incorporated into the films.

3. Precise control of composition by achieving stable deposition rates.

4. A UHV environment which allows sufficient time for characterization before surfaces are contaminated.

The realization of these growth conditions for high-T_c superconductors is different from semiconductors not just due to the different growth properties of metals and semiconductors. The high-T_c superconductors are all composed of at least one refractory element. Whereas effusion cells can be used to evaporate most of the elements needed for semiconductors, refractory metals must be deposited by electron-beam evaporation or by sputtering. Vacuum chambers must be designed so that there is no compromise in the level of contaminants due to the presence of a plasma for sputtering, or due to a greater heat load from higher source and substrate temperatures. Evaporation rates from electron-gun sources are inherently less stable than from effusion cells. Rate fluctuations are particularly significant for compounds with structural or superconducting properties which are sensitive to composition such as the A15 compounds.[1]

This paper is organized as follows: The capabilities of our vacuum system will be described with an emphasis on the conditions necessary for MBE-type growth and analysis of metallic films. Examples will be given of the manner in which surface analytical tools are used to help prepare and to investigate epitaxial high-T_c superconducting films and refractory tunnel junctions. The examples are in the areas of substrate preparation, niobium nitride, niobium-tin, and molybdenum-rhenium.

AN INTEGRATED DEPOSITION AND ANALYSIS FACILITY

The four chambers of the UHV deposition and analysis facility at Westinghouse are shown schematically in Figure 1. Three of the chambers were designed and fabricated by ISA/Riber. The prototype design was based, in part, on specifications and concepts developed by future users. The magnetron sputtering chamber was designed and assembled by Westinghouse. Samples as large as 2-inch wafers are clamped to molybdenum blocks before insertion to the system. The molybdenum blocks can be transferred between chambers, without exposure to atmosphere, through gate valves using transfer rods which are magnetically coupled to the exterior of the system.

Each chamber has two positions on its manipulator which hold the blocks - one heated stage and one unheated stage. The blocks have a small cavity on the back into which a fixed W-Re thermocouple is inserted as the block is mounted on a heated stage. A larger cavity in the molybdenum block surrounds the fixed heater filament. The transfer mechanism and heater configurations are standard Riber equipment although the 1250°C heaters were designed for this system.

Evaporation Chamber

Figures 2a and 2b show vertical and horizontal cross sections, drawn to scale, of the evaporation chamber. The levels labeled in Figure 2a are the transfer level, substrate and RHEED (Reflection High-Energy Electron Diffraction) level, rate monitor sensor and main shutter level, and effusion cell and electron-beam source level. The walls of the chamber are largely shielded from radiation from the electron guns by liquid-nitrogen-filled cryopanels (stippled areas). Figure 2b shows the arrangement of evaporation sources at the level of the electron-beam guns. Guns #1 and #2 have 40 cc hearths and are mounted on the same flange. Gun #3 has 4 hearths in-line, each with a 7 cc capacity. Gun #4 has 3 small in-line hearths. The position available for effusion cell #1 currently has a standard evaporation boat mounted in place of a third effusion cell.

Shuttered vibrating-crystal rate monitors are mounted above guns #1, #2, and #3. A fourth crystal monitor is positioned as close to the sample block as possible on the substrate level. Rate information from the crystal monitors is use in a feedback loop to control the filament current for

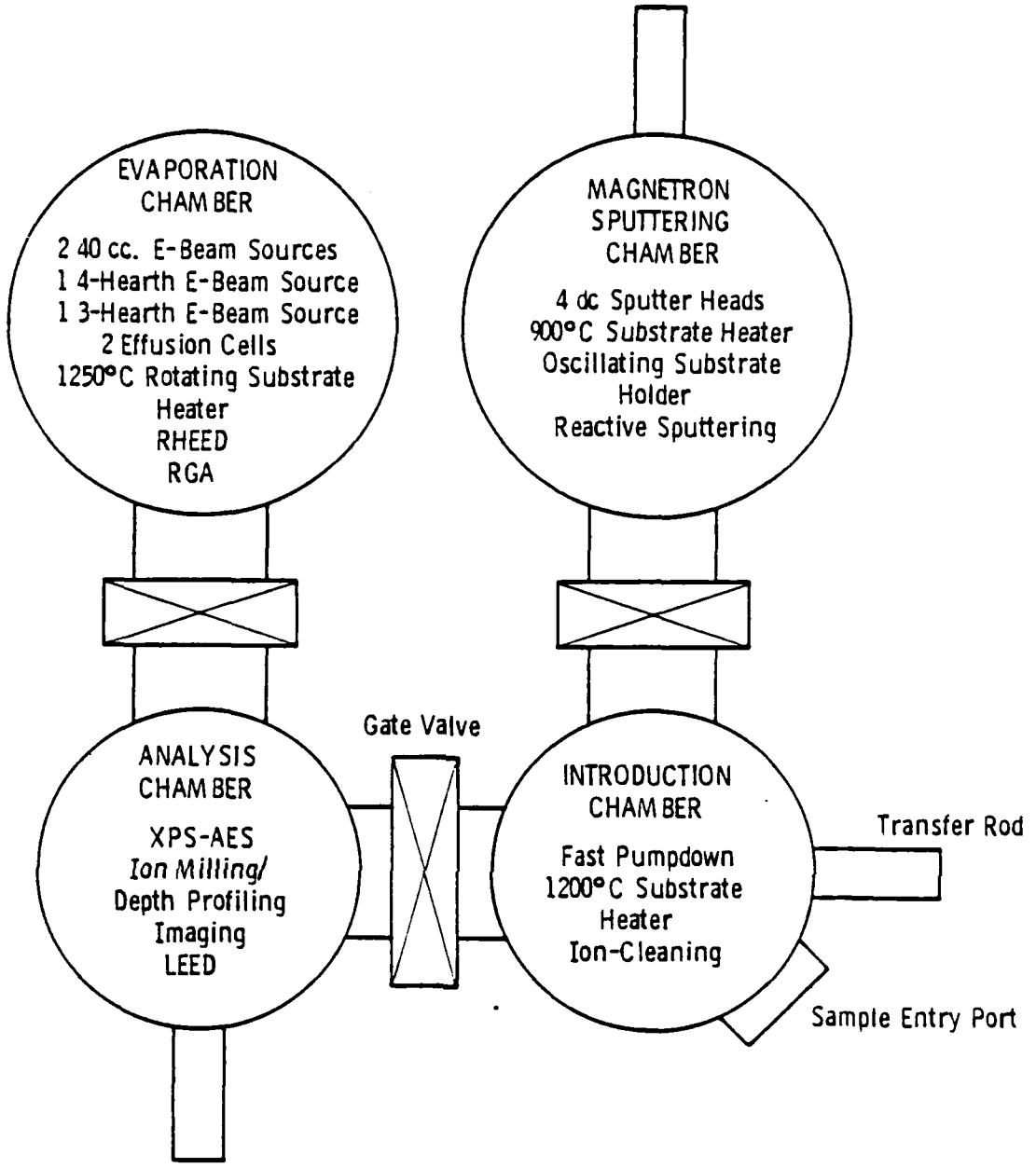

Fig. 1. Schematic of the Westinghouse deposition and analysis facility.

guns #3 and #4. "Sentinel" rate monitors made by Leybold-Heraeus/Inficon, which use Electron Impact Emission Spectroscopy (EIES) to obtain a photon count proportional to the flux of evaporant, are positioned above guns #1 and #2. The vibrating-crystal rate monitors are used to calibrate the Sentinel sensors before each evaporation. The beam position on the hearth of a 40 cc gun is swept both laterally and longitudinally. Following Hammond,[1] the signal from the rate monitor can be used to control the amplitude of the sweep in one direction for a faster response to fluctuations than can be achieved by changes to the filament current alone. The response time is limited to 100 msec, the period at which the Sentinel updates its output signal. One reason that the Sentinel rate monitors are used in place of crystal monitors over the large sources is that there is no accumulated deposit to require frequent periodic maintenance. Our experience indicates that replacing crystals, removing flakes and debris, and replenishing sources has to be performed every 10 to 14 weeks.

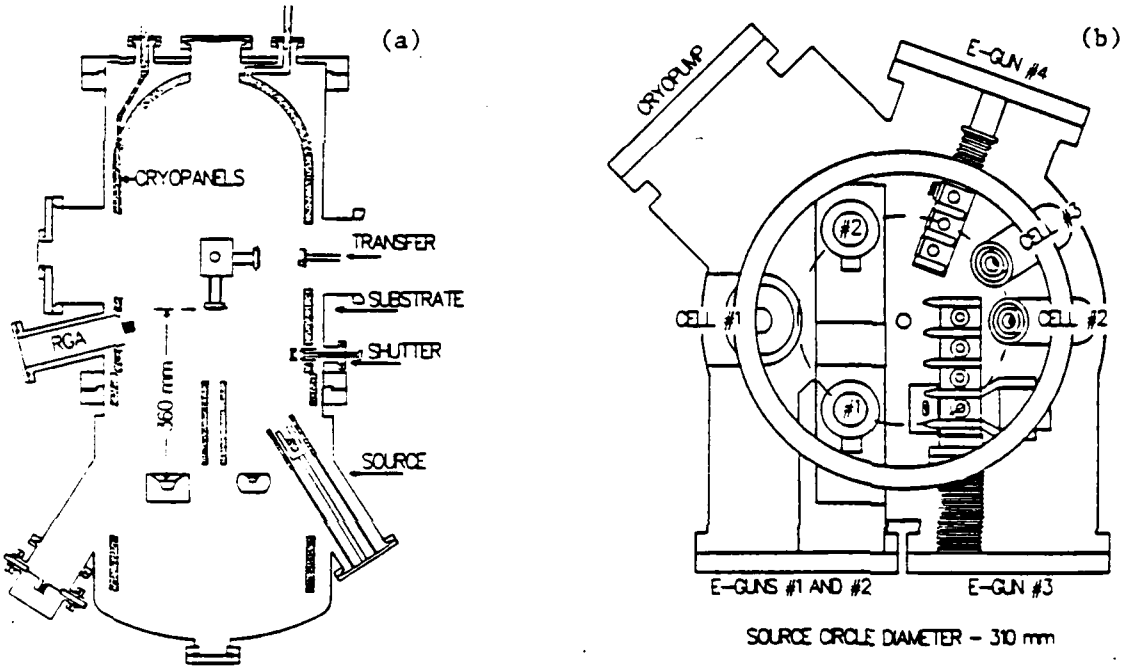

Fig. 2. Scale drawings of the evaporation chamber in (a) vertical section and (b) horizontal section at the source level.

Evaporation rates from the effusion cells are controlled indirectly by using the temperature of the cell to control cell heater current. The short-term rates are inherently stable due to the thermal mass of the cell. Several minutes are needed for the temperature of the cell to equilibrate after its shutter is opened, but the main shutter remains closed during that time. Changes in the level of the charge in the cell have not been great enough in typical 10-14 week periods to affect the reproducibility of rates versus temperature.

The evaporation chamber is pumped by a 400 liter/sec ion pump and a titanium sublimation pump. The normal base pressure (cryopanels cold) is $< 3 \times 10^{-9}$ Pa. Typical background pressure during evaporation of a film using a 40 cc electron-beam source is 2×10^{-8} Pa. The background pressure is somewhat lower if only the small guns or effusion cells are used. Substrates can be rotated during deposition and heated up to 1250°C.

Sputtering Chamber

A horizontal cross-section of the sputtering chamber at the level of the substrates and sputtering targets is shown in Figure 3. There are four sputter guns which accommodate 2-inch targets. Three of the guns are dc magnetron sources and the fourth, an rf magnetron gun, has been added recently. The substrates can be rotated to face any source, oscillated ±30° in front of a single source to promote uniform coverage, or oscillated ±60° between two guns for co-depositions.

A base pressure in the mid 10^{-7} Pa range is reached with a cryopump, titanium sublimation pump, and a 100 liter/sec ion pump. With the cryopump pumping through a nearly-closed throttle valve, just before adding the sputtering gas, the pressure is about 1×10^{-6} Pa. The level of impurities due to the background pressure is lower than the level introduced by research-grade argon with a pressure of 1 Pa. However, clean surfaces become contaminated with about a monolayer of oxygen in 10-30 minutes after deposition. The presence of a plasma apparently increases the out-

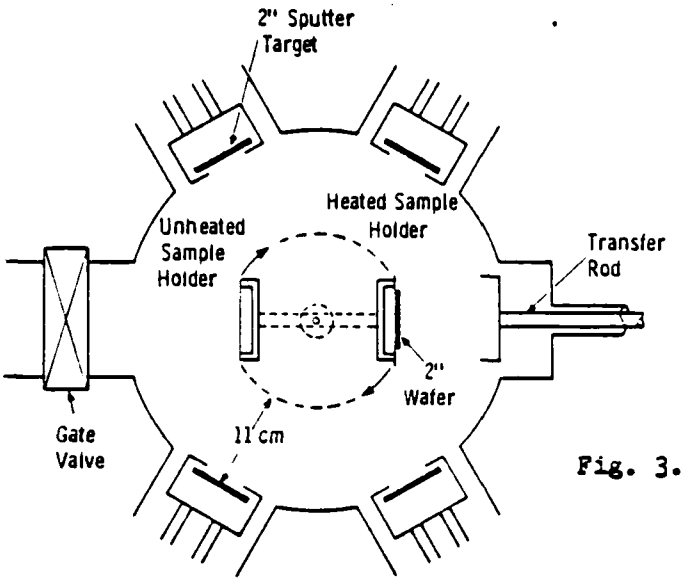

Fig. 3. Horizontal cross section of the magnetron sputtering chamber at the level of the targets and substrates.

gassing rate from the chamber walls. To qualify as an analogue to MBE systems, this chamber should have a liquid-nitrogen-filled cryopanel similar to the evaporation chamber or the sputtering system described in reference 2.

Analysis Chamber

The most important of the surface analysis techniques available in the analysis chamber has been X-ray Photoelectron Spectroscopy (XPS). The primary advantage of Auger Electron Spectroscopy (AES) over XPS is the possibility of focusing the beam to analyze a small area. However, for analysis of freshly-deposited films which cover large areas, XPS is preferred because the chemical shifts are more easily interpreted. AES is more frequently used in conjunction with ion milling to obtain depth profiles so that only a small area needs to be milled. However, with deposition and analysis capabilities both present in UHV, the uncertainties of ion-induced chemical change and uneven milling rates can be avoided by obtaining "depth profile" information as a multilayer structure is being formed.

The analysis chamber is pumped by a 200 liter/sec ion pump and a titanium sublimator. Typical pressure is 5×10^{-9} Pa, without cooling the sublimator cryoshroud. The electron spectrometer is a Riber MAC-1.

Introduction Chamber

The introduction chamber is the only one which is not baked each time it is vented. It has one 6" port, normally sealed with a viton o-ring, which can be quickly opened and closed for loading samples into the system. A rough vacuum is obtained with sorption pumps, and the chamber is pumped with a cryopump. The pressure can be reduced from 1 atm to $< 5 \times 10^{-6}$ Pa in 20 min. Then the sample block can be transferred to the sputtering or analysis chamber without deteriorating the vacuum level in those chambers. Pumping overnight reduces the pressure to about 1×10^{-7} Pa.

The introduction chamber is used for operations which would compromise the cleanliness of the other chambers such as an initial degassing of sample blocks, thermal oxidation in oxygen pressures up to 10 Pa, low-energy ion beam cleaning, and ion-beam oxidation in an argon/oxygen background.

SUBSTRATE PREPARATION

An essential preliminary step to the growth of epitaxial films is the preparation of single-crystal substrates with clean and damage-free surfaces. A procedure for preparing the surface must be developed and evaluated without removing the sample from vacuum. In principle, the procedure may be developed in one vacuum system and then repeated in the deposition system without characterizing its effect. However, we have found that the application of published cleaning processes, even one developed by us in a different vacuum system, may require some modification such as a longer ion-milling time or higher annealing temperature to obtain equivalent results. Some examples of substrate preparation are presented below with an emphasis placed on the role of in-situ characterization.

Sapphire (α-Al_2O_3) surfaces with a commercial epitaxial-grade polish have a layer of adsorbed carbon on the surface. Sinharoy has shown that the carbon AES signal from the (0001) surface can be reduced by thermal desorption up to 1000°C.[3] Therefore, sapphire substrates are routinely pre-heated to 900-1000°C even for low-temperature depositions and then brought to the deposition temperature. No carbon has been detected by in-situ XPS after heating. RHEED patterns show that the surface is smooth and crystalline in contrast to sapphire with a fine, non-epitaxial polish. The samples with the lower-grade polish exhibit a RHEED pattern characteristic of an amorphous surface. Single-crystal and polycrystalline Nb films have been grown side-by-side on sapphires with the different polishes for diffusion-couple experiments investigating the formation of A15 phase Nb_3Sn and Nb_3Al.[4]

Single crystals of A15 Nb_3Ir, grown by E. Walker at the Universite de Geneve, have been used for the epitaxial growth of Nb_3Ge. The cleaning procedure, developed in a separate surface analysis system, used an ion heat treatment, that is, a 500 eV argon ion milling while the sample was maintained at a temperature of > 700°C.[5] This combination was more effective than heating alone or ion milling followed by heating, in removing oxygen from the surface. Oxygen-free (100) and (111) surfaces exhibited unreconstructed (1x1) Low-Energy Electron Diffraction (LEED) patterns. Only the (110) surface exhibited a reconstructed surface when there was no oxygen contamination.

The prescribed ion heat treatment for Nb_3Ir was repeated in the deposition and analysis system. Although there were some differences in the apparatus compared with the vacuum system where the recipe was developed (such as a 45° incidence for the ion beam instead of normal incidence), it was surprising to find that two cycles of the ion heat treatment at 800°C followed by annealing at 1000°C were needed to remove all oxygen from the surface as determined by XPS. XPS and AES sampled comparable distances of about 1.5 nm into the film in this case because the O(1s) photoelectrons and O(KVV) Auger electrons have comparable kinetic energies. This experience emphasized the necessity of in-situ characterization of the actual substrate to be used for film growth.

Single crystals of MgO were polished with Syton (0.035 micron silica particles in a basic solution), degreased, and heated to 700°C to remove adsorbed gases. Without additional treatment, LEED patterns were observed and the surface was free of carbon.[6]

NIOBIUM NITRIDE

All NbN films have been prepared by reactive dc magnetron sputtering. Epitaxial, single-crystal films have been grown on several orientations of

sapphire and MgO substrates,[7] following Noskov et al. and Oya and Onodera.[8,9] Details of the deposition parameters and the role of epitaxy in stabilizing the high-T_c composition of NbN are reported in reference 7.

The epitaxial relationship between the substrate and film can be easily observed with RHEED. Figure 4a is a RHEED pattern of a (100) MgO crystal. The azimuthal angle of the electron beam with respect to the crystal was adjusted by rotating the sample block until a high-symmetry pattern was observed. In this case, the beam is parallel to the (010) direction. After a 100 nm thick NbN film was deposited at 700°C in the sputtering chamber, the block was transferred back to the evaporation chamber and the azimuthal angle was set to the value used for the substrate ($\pm$ 1°). The pattern in Figure 4b was observed. The presence of streaks instead of spots, Kikuchi lines, and the ring of lines at the bottom of the photograph, indicates that the film is a smooth single crystal.[10]

The RHEED patterns are more difficult to interpret for epitaxial relationships between crystals with different structures such as NbN grown on sapphire, although x-ray diffraction can be used for thick enough films. Figures 4c and 4d show RHEED patterns, at a fixed azimuthal angle, of an (0001) sapphire substrate and a 100 nm thick NbN film deposited at 700°. In this case, the growth direction was easily identified by comparison with the RHEED pattern of a (111) NbN film (Figure 4f) grown at

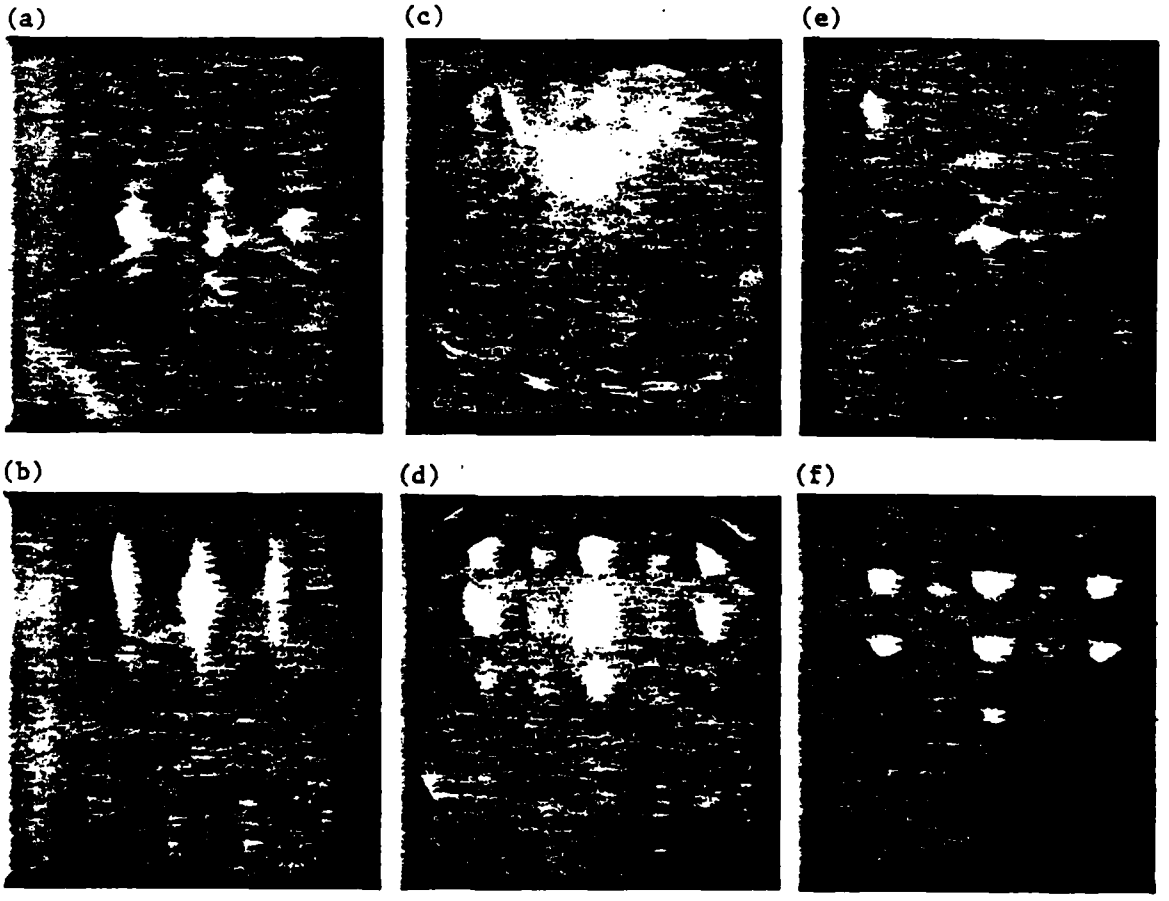

Fig. 4. Pairs of RHEED patterns for substrate and film with a fixed azimuthal angle: (a) (100) MgO substrate and (b) (100) NbN film deposited at 700°C; (c) (0001) sapphire substrate and (d) (111) NbN film deposited at 700°C; (e) (111) MgO substrate and (f) (111) NbN film deposited at 300°C.

300°C on a (111) MgO substrate (Figure 4e). For the (111) NbN films, the RHEED patterns exhibited "arrowhead"-shaped spots rather than streaks. The spot pattern indicated that the electron beam was diffracted by a three-dimensional crystal caused by the roughness of the surface of the film. The shape of the spots was a signature of a faceted surface.[11]

These samples provide an opportunity to study fundamental superconducting properties of NbN that may be anisotropic, such as tunneling $\alpha^2F(\omega)$ and H_{c2}. We have used XPS to measure the anisotropic growth of the native oxide of (100), (111), and randomly-oriented polycrystalline surfaces at room temperature.[12] After three days exposure to air, the respective thicknesses were 1.5 nm, 1.9 nm, and 1.8 nm based on assumptions of a uniform thickness for the oxide layer and a photoelectron escape depth of 2.0 nm. A number of groups have successfully used the thermally-grown native oxide for tunnel barriers.[13-16] We have also made low-leakage junctions with the native oxide of polycrystalline films using Pb-Bi counterelectrodes. The ratio of the current at 5 mV (above the gap) to the current below the gap, i(5)/i(2.5), was as high as 110 at 4.2K. However, the oxide that formed on the (100) and (111) surfaces had much different barrier properties. The relatively thin oxide of the (100) surface formed a low-leakage barrier that had a resistance 2 orders of magnitude higher than the oxide of the polycrystalline film. The thicker oxide of the (111) surface had a similarly high resistance but the tunnel junctions had high leakage currents, perhaps related to the faceted surface observed with RHEED. The native oxide grown thermally on single-crystal Nb films has also been reported to have properties as a tunnel barrier that were different from the oxide grown on polycrystalline Nb.[17]

The oxides of thin overlayers of Al and Mg have also been used to make low-leakage NbN / oxide / Pb-Bi tunnel junctions with higher resistances than the native oxide.[18] However, just as with the native oxide, attempts to make tunnel junctions with NbN counterelectrodes resulted in shorted barriers. One solution was to use a low-energy (300 V was optimum) argon-oxygen ion beam to make the Al or Mg oxide thicker (determined by XPS) and, perhaps, more uniform. The effect of the ion beam was to remove material from the surface while oxidizing in an analogue to the Greiner process.[19] Ion-beam oxidation has been used to form the native oxide of Nb films,[20-22] but has not been used before with an artificial barrier. The role of in-situ XPS was crucial in determining the end-point of the process, the point at which a minimum of unoxidized Al or Mg remained and the NbN was not yet oxidized. A typical sequence of spectra for the Al_{2p} XPS peak from a NbN / ion-beam-oxidized-Al bilayer is shown in Figure 5. Comparison of the photoelectron count from oxidized (chemically-shifted) Al with unoxidized Al and with Nb (not shown) gives the thickness of the Al_2O_3. The tunneling data are reported in reference 18.

There have been several published observations of the diffusion of a thin metal overlayer into the grain boundaries of a metal base, even at room temperature.[23-25] We have measured the thicknesses of oxidized Al and Mg overlayers on polycrystalline NbN by XPS as a function of analysis temperature (Figures 6a and 6b). The purpose of such measurements was to observe possible diffusion of the overlayer into the base and possible changes in the chemistry of the oxides at temperatures which would be desirable for counterelectrode deposition. The thickness of the unoxidized metal layer was initially two to four times greater than for samples used for tunnel junctions so that diffusion would be easier to observe. The samples were maintained at each temperature for 15 minutes before collecting the XPS spectra during an additional hour. In the case of the oxidized Al overlayer, there was no observable change in the oxide thickness or chemical shift up to 800°C. The thickness of the unoxidized Al layer decreased to only half of its room temperature value at 800°C, above the

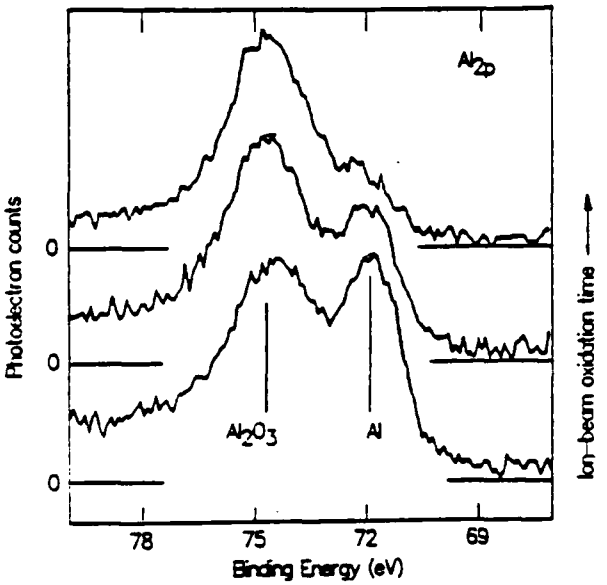

Fig. 5. XPS spectra for Al_{2p} photoelectrons used for monitoring the effect of ion-beam oxidation. The first spectrum was recorded after an initial thermal oxidation at room temperature for 15 min in 13 Pa oxygen.

melting point of Al. However, for the oxidized Mg overlayer, the unoxidized Mg thickness started to decrease at 300°C and disappeared by 500°C. No changes were seen in the MgO.

The results suggest that high temperatures might be used for counterelectrode growth, particularly for oxidized Al barriers. We have deposited NbN counterelectrodes on NbN / oxidized Al bilayers at temperatures up to 300°C. The leakage currents for junctions formed at 300°C were comparable to junctions with NbN counterelectrodes deposited at room temperature. Tunnel junctions with oxidized Mg barriers had a lower V_m compared to junctions with oxidized Al barriers due to smearing of the NbN gap rather than higher leakage at zero bias.[18] We attribute the smearing to the diffusion of Mg into the NbN base electrode. Since the ionic radius of Mg is larger than that of Al, the diffusion of Mg may be accompanied by a reaction forming magnesium nitride which does not occur in the case of Al. We have not been able to determine with XPS whether there was a reaction.

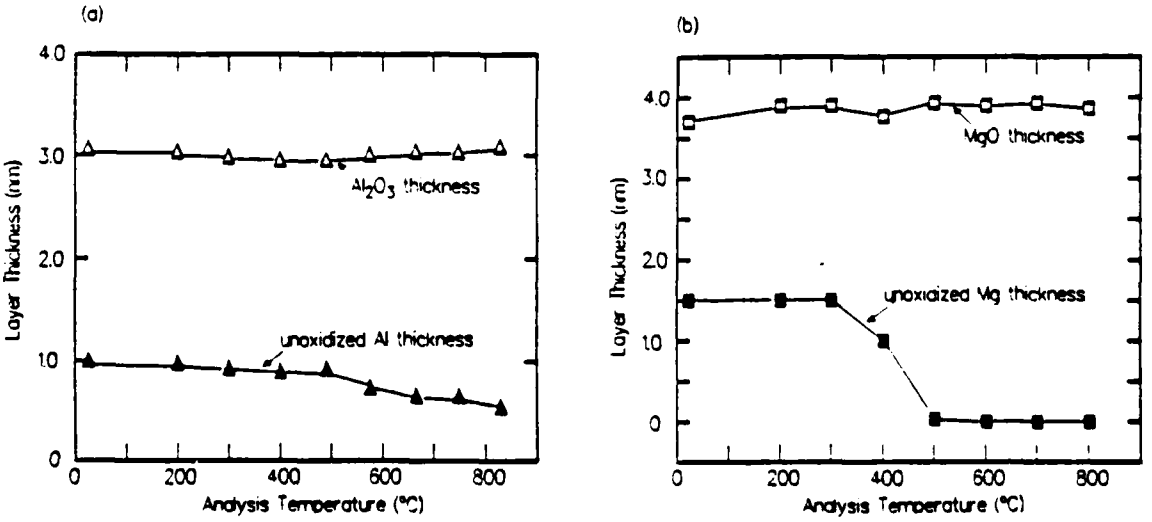

Fig. 6. The thicknesses of (a) Al_2O_3 and Al and, (b) MgO and Mg as a function of XPS analysis temperature for thin oxidized overlayers of Al and Mg on polycrystalline NbN.

NIOBIUM-TIN

A15-structure Nb_3Sn films have been formed by co-evaporation. The tin was evaporated from effusion cell #2 and the niobium from electron beam gun #1. A series of films were deposited at 850, 900, and 950°C without rotating the sample block. Plots of Sn composition versus sample position on the block showed a "composition locking" (re-evaporation of excess Sn from the Nb_6Sn_5 phase) at 25 atomic percent Sn, as reported by Rudman et al.,[26] for all but the 850°C films. The Nb_3Sn films used for studies of epitaxial growth and for tunnel junctions were deposited with a slight excess of Sn and at > 900°C.

Epitaxial films of Nb_3Sn have been grown on $(11\bar{2}0)$ and (0001) sapphire. RHEED patterns cannot be observed during evaporation from an electron-beam source or if the substrate temperature is > 700°C due to background light on the RHEED screen. However, the deposition of a (100) film was interrupted after 6.0 nm accumulation and the sample block cooled. We observed a RHEED pattern similar to that from a 200 nm thick single-crystal (x-ray rocking curve width of 0.4°) film, but with more diffuse spots.[27] There was no evidence that crystallites with another orientation were competing with the single crystal matrix as reported by Marshall et al. for a film grown on $(1\bar{1}02)$ sapphire.[28]

Figure 7 contains RHEED patterns of a 200 nm thick Nb_3Sn film and an 8.0 nm thick overlayer of CaF_2 observed from the same azimuthal angle. The CaF_2 was evaporated from a standard evaporation boat mounted in the position for effusion cell #1 in the evaporation chamber while the substrates were maintained at room temperature. The Nb_3Sn film was a smooth single crystal with an (100) growth direction. The RHEED pattern of the CaF_2 overlayer contains both rings and a pattern of focussed spots, suggesting that there was a mixture of randomly-oriented grains and an epitaxial matrix. Although the existence of an epitaxial relation between these structures has not been firmly established, both Nb_3Sn and CaF_2 have cubic structures and a lattice mismatch of only 3% (0.529 and 0.546 nm). Growth of CaF_2 at higher temperatures may provide an epitaxial insulator-superconductor system analogous to MgO-NbN which could promote the formation of a high-T_c layer in tunnel junction counterelectrodes within a coherence length of the barrier. The best epitaxial layers of CaF_2 grown on Si have been formed at 600±25°C.[29]

Tunnel junctions were made using the Nb_3Sn / CaF_2 samples by transferring them to another vacuum system to deposit Pb-Bi counterelectrodes.

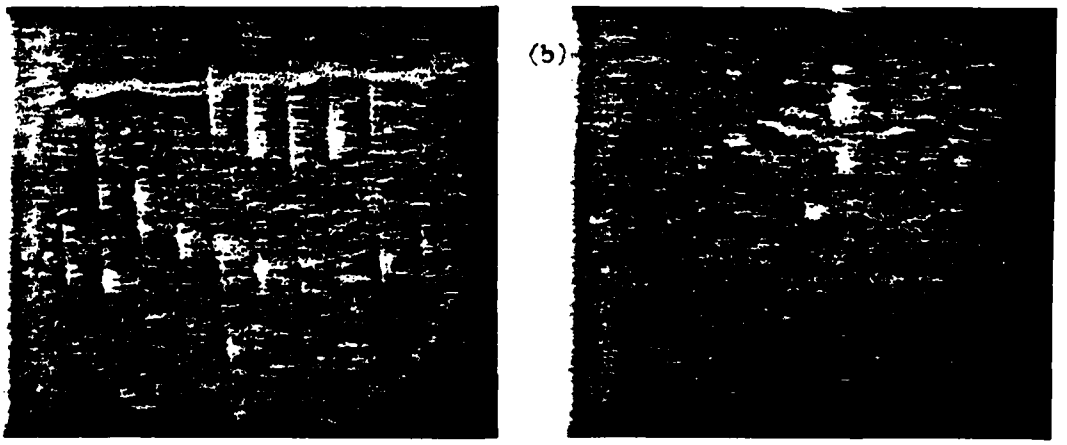

Fig. 7. RHEED patterns of (a) a 200 nm thick film of Nb_3Sn grown at 900°C, and (b) an 8.0 nm thick overlayer of CaF_2 deposited at 20°C.

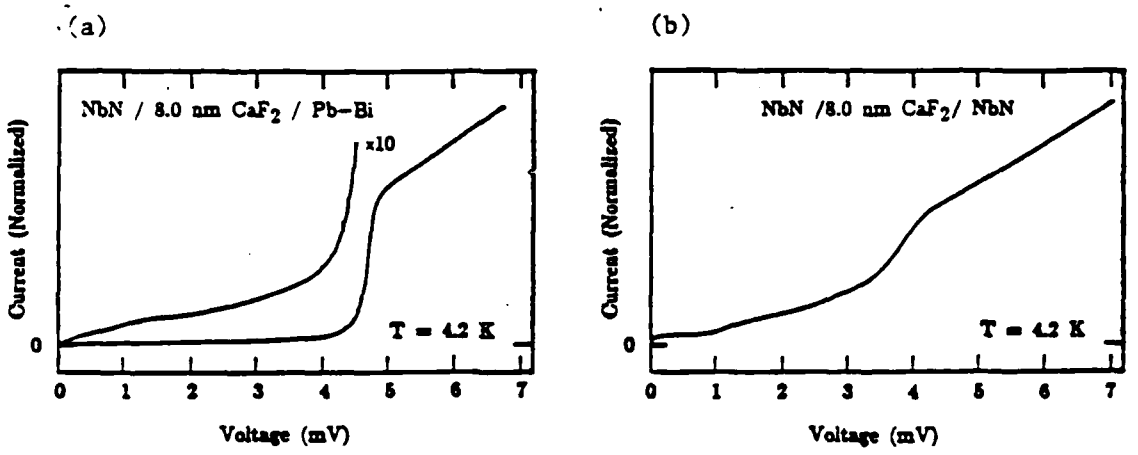

Fig. 8. Quasiparticle I-V curves for (a) NbN / CaF_2 / Pb-Bi and (b) NbN / CaF_2 / NbN tunnel junctions. The surface of the base electrode was oxidized prior to the CaF_2 deposition.

We measured samples with a range of thicknesses of the CaF_2 layer from 6.0 to 10.0 nm (based on evaporation rates and confirmed by XPS). All junctions had I-V curves characteristic of superconducting microbridges even though one might expect that the exposure to air just prior to depositing the counterelectrode would oxidize any area of the base electrode that was left exposed by pinholes in the CaF_2.[30] Similar I-V characteristics were observed for NbN / CaF_2 / Pb-Bi tunnel junctions.

In a second experiment with NbN base electrodes, a native oxide barrier was formed, prior to the deposition of 8.0 nm of CaF_2, by bleeding oxygen into the introduction chamber. The quasiparticle I-V curves for the latter set of samples, shown in Figure 8a for a Pb-Bi counterelectrode and Figure 8b for a NbN counterelectrode, indicated that the pinholes were sealed. The resistances of the junctions with Pb-Bi counterelectrodes were approximately 5×10^{-3} ohm-cm^2, two orders of magnitude higher than we typically obtained for the native oxide alone. The higher leakage at zero voltage for the junctions with NbN counterelectrodes was consistent with the fact, stated earlier, that the thermally-grown native oxide barrier was always shorted during the deposition of an NbN overlayer. The CaF_2 deposited on NbN was polycrystalline with randomly-oriented grains. Asano et al. have reported the successful use of amorphous ZrF_4 and AlF_3 tunnel barriers with Nb / Pb junctions.[31] They also had a low-resistance barrier, formed by cleaning in an Ar/CF_4 rf plasma, underneath the artificial fluoride barrier. Unresolved issues are whether the composite barrier structure is necessary for all of the fluoride compounds and whether the presence of pinholes is related to the evaporation of such compounds as undissociated molecular units.[32]

Figure 9a shows the I-V curve of a typical junction formed on a Nb_3Sn base with a thermally-oxidized Al barrier and a Pb-Bi counterelectrode. The tunnel junctions with thermally-oxidized barriers established that the top layer of the Nb_3Sn film was homogeneous with a high T_c,[27] but the thermal-oxide barrier was shorted by the deposition of refractory counterelectrodes. Figure 9b shows the I-V curve of a tunnel junction of the form, Nb_3Sn / Al_2O_3 / NbN, which was fabricated with the ion-beam oxidized Al tunnel barriers discussed in the previous section and in reference 18. The subgap conductance was primarily due to damage to the Nb_3Sn by the 300 V Ar-O_2 ion beam as indicated by the rise in conductance at the NbN gap.

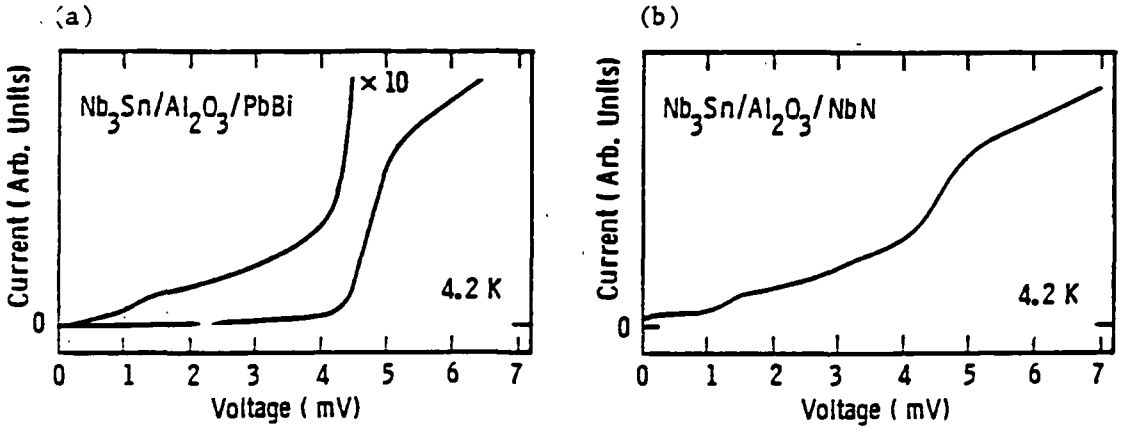

Fig. 9. I-V curves for Nb_3Sn-based tunnel junctions with oxidized Al barriers. (a) Thermal oxide and Pb-Bi counterelectrode. (b) Oxide formed by ion-beam treatment and NbN counterelectrode deposited at room temperature. The rise in conductance at the NbN gap, 1.2 mV, was from damage to the Nb_3Sn surface caused by the ion milling.

MOLYBDENUM-RHENIUM

We have studied the Mo-Re system in the range of 30 to 40 atomic percent Re for the following reasons:

1. A15 structure Mo_3Re provides an opportunity to study the stabilization of an A15 compound which does not exist in equilibrium at any composition.[33]
2. With a T_c of 12K for the bcc alloy and up to 15K for the A15 structure,[34] Mo-Re provides an alternative high-T_c material for refractory tunnel junctions.
3. In either the bcc or A15 structure, the T_c of Mo-Re is relatively insensitive to disorder. The coherence length, 20 nm, estimated from normal-state and superconducting properties in the literature,[35,36] is 4 to 5 times longer than for other high-T_c superconductors. Both are desirable properties for obtaining the T_c of the bulk material within a coherence length of a tunnel barrier / counterelectrode interface, particularly at low temperatures.

Single crystal films of bcc (α-Mo) structure $Mo_{65}Re_{35}$ with a (110) orientation and an x-ray rocking curve width of 0.3° have been grown by evaporation at 800°C on (11$\bar{2}$0) sapphire. The Mo source was electron-beam gun #2 and the Re source was gun #3. Although gun #3 is not equipped for high-frequency rate control, tunnel junctions made on these films with

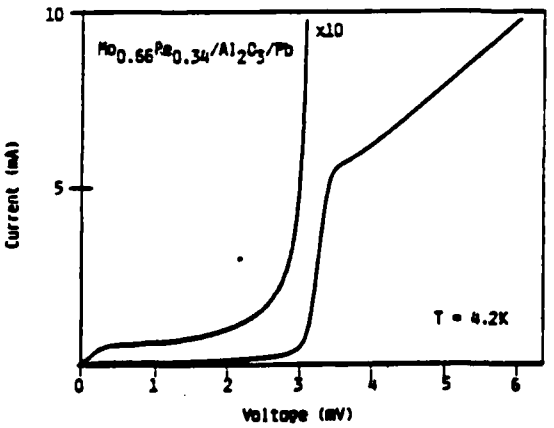

Fig. 10. Tunneling into a 20.0 nm thick $Mo_{65}Re_{35}$ film with a polycrystalline bcc structure. The width and value of the gap voltage showed that the film was homogeneous with T_c = 11.5K.

oxidized Al barriers and Pb counterelectrodes showed that the samples were homogeneous with a gap voltage only 0.2 meV wide. Films grown at 100°C had a polycrystalline bcc structure. The T_c's of the films agreed with values reported for bulk samples (12K) independent of substrate temperature in the range of 100 - 1000°C.[33] The T_c decreased by 0.5K for films grown both at low temperature (100°C) and only 20.0 nm thick, and were still homogeneous based on tunneling measurements (Figure 10).

A set of Mo-Re films were deposited at 1000°C in a background pressure of 6×10^{-7} Pa, consisting of mostly methane and nitrogen, and typical for the first set of films made after the evaporation chamber has been opened for maintenance, pumped out, and baked. Although other samples grown at the same temperature in a background of $< 2 \times 10^{-8}$ Pa had a single-crystal bcc structure, x-ray diffraction showed that the films grew with an A15 structure in a (100) orientation. The RHEED pattern showed a times-3 surface reconstruction that had not been seen for other Mo-Re films. A study of another single-crystal transition metal A15 compound, Nb_3Ir, found that the (100) surface also exhibited a (3x3) reconstruction when contaminated by oxygen and carbon.[5]

The formation of the A15 structure by evaporation has been reported by Postnikov et al. for comparable substrate temperatures but in a background pressure of about 10^{-4} Pa.[37] In contrast to the earlier A15 Mo-Re films formed by evaporation or sputtering, the single-crystal films had T_c values of approximately 12K. The onset of the transition for one film was 12.7K, 0.5K higher than found in any of the bcc samples. These results suggest that the impurities are needed not just to stabilize the A15 phase, but can also affect the T_c.

CONCLUSIONS

The growth of films of high-T_c superconductor materials in UHV has produced, with the appropriate choice and preparation of substrates, single-crystal samples for all superconducting materials that have been tested. For stable superconductors which have been grown as bulk single crystals, the existence of thin-film single crystals expands the number of characterization techniques which can be used to investigate the mechanisms of superconductivity, to include, for example, tunneling. Epitaxial thin-film growth is the only way to obtain single crystals of metastable compounds such as A15 Mo-Re and stoichiometric Nb_3Ge.

The combination of UHV film growth with in-situ surface treatment and analysis makes feasible the development of all-epitaxial tunnel junctions for high-operating-temperature circuit applications with low-loss transmission lines. At the least, clean, well-characterized interfaces and tunnel barriers used with homogeneous superconducting electrodes can serve as model systems for the study of barrier physics, metal-surface physics, nucleation and growth in metal-insulator epitaxial systems, and superlattices.

ACKNOWLEDGMENTS

This work was supported in part by AFOSR Contract No. F49620-78-C-0031 and ONR Contract No. N00014-82-C-0617. The authors would like to acknowledge ISA/Riber and especially M. Picault for their role in building the vacuum apparatus for this work. J. Bevk of Bell Laboratoies and C. M. Falco and I. K. Schuller of Argonne National Laboratory contributed to the design of the evaporation chamber. H. Pohl and A. L. Foley have contributed to the installation and operation of the facility.

REFERENCES

1. R. H. Hammond, Electron beam evaporation synthesis of A15 superconducting compounds: Accomplishments and prospects, IEEE Trans. Magn. MAG-11(2):201 (1975).
2. J. M. Lumley, R. E. Somekh, J. E. Evetts, and J. H. James, High quality all refractory tunnel junctions for SQUID applications, IEEE Trans. Magn. MAG-21(2):539 (1985).
3. S. Sinharoy, LEED and Auger studies of the structure and composition of the (0001) surface of sapphire, submitted to J. Surface Science.
4. A. I. Braginski, J. R. Gavaler, and K. Schultze, Formation of A15 phase in epitaxial and polycrystalline Nb-Sn and Nb-Al diffusion couples, presented at the International Cryogenic Materials Conference, Boston, 1985.
5. S. Sinharoy, A. I. Braqginski, J. Talvacchio, and E. Walker, A LEED, AES, and XPS study of single-crystal Nb_3Ir surfaces, submitted to Surf. Sci..
6. S. Sinharoy, private communication
7. J. R. Gavaler, J. Talvacchio, and A. I. Braginski, Epitaxial growth of NbN films, presented at the International Cryogenics Materials Conference, Boston, 1985.
8. V. L. Noskov, Y. V. Titenko, F. I. Korzhinskii, R. L. Zelenkevich, and V. A. Komashko, Heteroepitaxial layers of niobium nitride on sapphire, Sov. Phys. Crystallogr. 25(4):504 (1980).
9. G. Oya and Y. Onodera, Transition temperatures and crystal structures of single-crystal and polycrystalline NbN films, J. Appl. Phys. 45(3):1389 (1974).
10. M. G. Lagally, Diffraction techniques, in: "Methods of Experimental Physics, Vol.22," R. L. Park and M. G. Lagally, eds., Academic Press, New York (1983), pp. 237-298.
11. B. A. Joyce, J. H. Neave, P. J. Dobson, and P. K. Larsen, Analysis of reflection high-energy electron-diffraction data from reconstructed semiconductor surfaces, Phys. Rev. B 29(2):814 (1984).
12. J. R. Gavaler, A. I. Braginski, M. A. Janocko, and J. Talvacchio, Epitaxial growth of high-T_c superconducting films, presented at the International Conference on the Materials and Mechanisms of Superconductivity, Ames, Iowa, May, 1985.
13. J. C. Villegier, L. Vieux-Rochaz, M. Goniche, P. Renard, and M. Vabre, NbN tunnel junctions, IEEE Trans. Magn. MAG-21(2):498 (1985).
14. R. B. van Dover, D. D. Bacon, and W. R. Sinclair, Superconductive tunneling into NbN deposited near room temperature, Appl. Phys. Lett. 41(8):764 (1982).
15. V. M. Pan, V. P. Gorishnyak, E. M. Rudenko, V. E. Shaternik, M. V. Belous, S. A. Koziychuk, and F. I. Korzhinsky, Investigation of the properties of niobium nitride films, Cryogenics 23(5):258 (1983).
16. M. Igarashi, M. Hikita, and K. Takei, Barrier/electrode interface structure and I-V characteristics of NbN Josephson junctions, in: "Advances in Cryogenic Engineering - Materials," vol. 30, Plenum Press, New York (1984), p. 535.
17. S. Celaschi, T. H. Geballe, and W. P. Lowe, Tunneling properties of single crystal Nb / Nb_2O_5 / Pb Josephson junctions, Appl. Phys. Lett. 43(8):794 (1983).
18. J. Talvacchio, J. R. Gavaler, A. I. Braginski, and M. A. Janocko, Artificial oxide barriers for NbN tunnel junctions, submitted to J. Appl. Phys.
19. J. H. Greiner, Oxidation of Pb films by rf sputter etching in an oxygen plasma, J. Appl. Phys. 45(1):32 (1974).
20. R. Herwig, Ion-beam oxidation of Nb-based Josephson junctions, Electron. Lett. 16:850 (1980).

21. A. W. Kleinsasser and R. A. Buhrman, High-quality submicron Nb tunnel junctions with reactive ion-beam oxidation, Appl. Phys. Lett. 37(9):841 (1980).
22. S. S. Pei and R. B. van Dover, Ion beam oxidation for Josephson circuit applications, Appl. Phys. Lett. 44(7):703 (1984).
23. J. Kwo, G. K. Wertheim, M. Gurvitch, and D. N. E. Buchanan, X-ray photoelectron study of surface oxidation of Nb/Al overlayer structures, Appl. Phys. Lett. 40(8):675 (1982).
24. J. Kwo, G. K. Wertheim, M. Gurvitch, and D. N. E. Buchanan, XPS and tunneling study of air-oxidized overlayer structures of Nb with thin Mg, Y, and Er, IEEE Trans. Magn. MAG-19(3):795 (1983).
25. A. I. Braginski, J. R. Gavaler, M. A. Janocko, and J. Talvacchio, New materials for refractory tunnel junctions: Fundamental aspects, presented at the Third International Conference of Superconducting Quantum Devices, Berlin, June, 1985.
26. D. A. Rudman, F. Hellman, R. H. Hammond, and M. R. Beasley, A15 Nb-Sn Tunnel Junction Fabrication and Properties, J. Appl. Phys. 55(10):3544-3553 (1984).
27. J. Talvacchio, A. I. Braginski, M. A. Janocko, and S. J. Bending, Tunneling and interface structure of oxidized metal barriers on A15 superconductors, IEEE Trans. Magn. MAG-21(2):521 (1985).
28. A. F. Marshall, F. Hellman, and B. Oh, Epitaxy of Nb_3Sn films on sapphire, in: "Layered structures, Epitaxy, and Interfaces," Materials Research Society, Pittsburgh (1985), p. 517.
29. J. M. Phillips, Recent progress in epitaxial fluoride growth on semiconductors, in: "Layered structures, Epitaxy, and Interfaces," Materials Research Society, Pittsburgh (1985), p. 143.
30. D. A. Rudman and M. R. Beasley, Oxidized amorphous-silicon superconductung tunnel junction barriers, Appl. Phys. Lett. 36(12):1010-1013 (1980).
31. H. Asano, K. Tanabe, O. Michikami, M. Igarashi, and M. Beasley, Fluoride barriers in Nb/Pb tunnel junctions, Jap. J. Appl. Phys. 24:289 (1985).
32. R. F. C. Farrow, P. W. Sullivan, G. M. Williams, G. R. Jones, and D. C. Cameron, MBE-grown fluoride films: A new class of epitaxial dielectrics, J. Vac. Sci. Technol. 19(3):415 (1981).
33. R. D. Blaugher, A. Taylor, and J. K. Hulm, The superconductivity of some intermetallic compounds, IBM J. of Res. and Dev. 6(1):116 (1962).
34. J. R. Gavaler, M. A. Janocko, and C. K. Jones, A15 Structure Mo-Re superconductor, Appl. Phys. Lett. 21(4):179 (1972).
35. F. J. Morin and J. P. Maita, Specific heats of transition metal superconductors, Phys. Rev. 129(3):1115 (1963).
36. A. Echarri, M. J. Witcomb, D. Dew-Hughes, and A. V. Narlikar, Dependence of the lower critical field on normal state resistivity in superconducting alloys, Philos. Mag. 18:1089 (1968).
37. V. S. Postnikov, V. V. Postnikov, and V. S. Zheleznyi, Superconductivity in Mo-Re system alloy films produced by electron beam evaporation in high vacuum, Phys. Status Solidi A 39:K21 (1977)

APPENDIX B

TUNNELING AND INTERFACE STRUCTURE OF OXIDIZED METAL BARRIERS ON A15 SUPERCONDUCTORS

J. Talvacchio,* A. I. Braginski,* M. A. Janocko*
Westinghouse R&D Center, Pittsburgh, PA 15235

and S. J. Bending+
Hansen Laboratories, Stanford University, Stanford, CA 94305

Abstract

A15-based tunnel junctions have been prepared with barriers of oxidized Al, Si, and Y. Properties of the superconductor/barrier interface which are crucial for low-leakage junctions were established by correlating XPS spectra of oxidized bilayers and RHEED patterns of the surface of each layer with tunneling characteristics. Comparisons were made between oxidized Al barrier properties for Nb and Nb_3Sn base electrodes. Some differences between evaporated and dc magnetron sputtered barriers have emerged.

Introduction

Recent work by Gurvitch and Kwo has correlated the physical properties of oxidized metal overlayers on Nb with electrical properties of the overlayers used as tunneling barriers.[1] Our objective has been to extend that type of study to A15-based tunnel junctions. Our choice of Al and Y as the focus of the study was based on Gurvitch and Kwo's evidence that Al and Y layers < 20 Å thick provide complete coverage of a Nb surface, and some requirements which are more important for A15-based junctions than for Nb. The use of high-T_c superconductors as counterelectrodes will probably require high temperature processing. Both Al_2O_3 and Y_2O_3 are stable oxides at temperatures of interest (< 1000°C) without suboxides. Yttrium and the rare earth elements which have a similar chemistry were considered because the diffusion rates of such massive atoms are lower.

The crystallinity of the tunneling barrier may be more important for A15 junctions than for Nb because atomic order in the first 50 Å (about one coherence length) of an A15 counterelectrode is more critical than for Nb with its longer coherence length.

Sample Preparation

Deposition of Nb_3Sn and V_3Si base electrodes was carried out in a multiple-chamber UHV system with facilities for deposition and in situ surface analysis. Sapphire substrates were clamped to a molybdenum block heated to 800 to 900°C as measured by a W-5% Re/W-26% Re thermocouple inserted in a cavity in the block. The molybdenum block was rotated at about 20 rpm in the case of evaporation or oscillated in front of the target at 20 cycles per minute in the case of dc magnetron sputtering. After the samples cooled to < 200°C, barrier layers of Al or Y were either sputtered or evaporated without removal from vacuum. Some variations in the oxidation procedure will be discussed but generally the samples were exposed to 100 millitorr of dry oxygen for an hour before removal from the system. They were kept in a controlled-humidity atmosphere (40%) during the 10 minutes required to paint on an insulating layer and load the samples for evaporation of a PbBi counterelectrode through an aperture mask.

The V_3Ga films were evaporated by one of us (SJB) at Stanford with a similar procedure but using silicon barriers oxidized in air.

Atomic Segregation at Oxidized A15 Surfaces

The native oxides of A15 superconductors usually form poor tunneling barriers.[2] Ihara et al. have shown qualitatively using X-ray Photoelectron Spectroscopy (XPS) that an atomic segregation of the constituents of an A15 compound occurred when the surface was oxidized.[3] Our data for Nb_3Sn, V_3Si, and V_3Ga are shown in Table 1. The compositions listed in Table 1 which were derived from XPS measurements were based on elemental sensitivities compiled by the analyzer manufacturer modified by our own measurements of elemental standards.

The layer thicknesses were calculated using the integrated area of each photoelectron peak following Carlson and McGuire for the structure shown in Figure 1.[4] Their equations were based on the assumption that each layer had a uniform thickness and was on a flat substrate. A photoelectron escape depth of λ = 20 Å was used for the tabulated data. The calculations have been repeated using λ = 16 Å for metallic layers and λ = 27 Å for oxide layers following Ermolieff et al. without any qualitative difference in the results.[5] Bulk densities were assumed in the calculation of layer thicknesses.

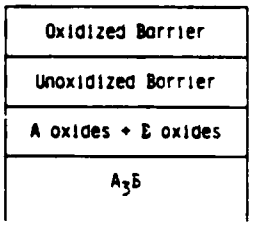

Figure 1 — The structure used to calculate layer thicknesses from XPS.

A greater limitation for our application of the Carlson and McGuire formulation was their restriction to photoelectron peaks with similar kinetic energies. Penn found that V_{2p} photoelectrons with a kinetic energy of 742 eV (Mg $K\alpha$ X-rays) has λ = 15 Å.[6] The other relevant photoelectrons have kinetic energies between 1000 eV and 1200 eV with λ = 18 to 21 Å. If this difference was important, the lowest layer which contained V should have shown the greatest attenuation. However, the first row of Table 1 shows that the number of V_{2p} photoelectrons detected even through a 100 Å barrier is sufficient to give a composition which agrees with the bulk composition from electron microprobe.

The entries in Table 1 for each A15 compound were ordered by increasing thickness of the oxidized A15 layer. The oxidation occurred either because there was

*Supported by ONR Contract No. N00014-82-C-0617.

*Supported in part by AFOSR Contract No. F49620-78-C-0031.

+Supported in part by DOE Contract No. DE-AT03-76ER71043 and ONR Contract No. N00014-83-K-0391.

Manuscript received September 10, 1984.

Table 1 – Surface Segregation of A15 Compounds

Compound A_3B	Sample #	Barrier Thickness (Å)	Oxidized A15		A15 Metal	
			Thickness (Å)	% B Oxide	at. % B (XPS)	at. % B (bulk
V_3Si	9-B5	100	0	--	24	27
	3-B5	37	2	100	30	30
	4-B5	20	9	100	80	35
	8-B2	0	73	62	47	29
	8-B4	0	> 100	72	--	29
Nb_3Sn	18-B5	50	0	--	21	21
	33-B6	26	4	48	31	26
	13-B4	0	33	39	23	23
V_3Ga	138-A10	20	0	--	23	23
	114-A1	25	0	--	22	21
	114-B1	25	11	45	22	29

no barrier or a very thin one, or in some cases because there was some exposure to oxygen before barrier deposition. The column which lists the percentage of B element oxide shows the extent of segregation which occurred during oxidation. It is the number density of B atoms in an oxide environment compared with the total number of A and B atoms which emit photoelectrons with a chemical shift characteristic of the oxide. By this definition, an A_3B compound which was completely oxidized would have an entry of 25%.

When V_3Si oxidized, SiO_2 formed first and a number of samples have also shown an increased silicon concentration in the metal underneath. There must have been a V-rich layer left behind which would be deep enough compared to the coherence length of 40 Å to affect tunneling properties. Sample 8-B4 had an oxide layer which was too thick to measure because it was dipped in water and left to dry in air.

The background pressure in the magnetron sputtering system where V_3Si samples were made was typically 1×10^{-8} torr with the pumping line throttled for introduction of argon. About 20 minutes were needed to return to this pressure after the base electrode was deposited. However, the sample block needed 30 minutes to cool to < 200°C and deposited films always showed 2 to 5 Å of surface oxide growth after that time. A liquid nitrogen-cooled quenching block was assembled which pressed against the edges of the sample block during the time between base electrode and barrier depositions to cut the cooling time to < 10 minutes. This procedure has led to an order of magnitude reduction in subgap currents. However, the V_3Si transition temperatures have been less than 15K with correspondingly low gap values. We were limited to deposition rates (25 Å/min.) which were probably too low for a material which getters as well as vanadium.

The segregation of Nb_3Sn was less dramatic than for V_3Si. Nb_2O_5 forms at the same time as SnO_2 but in a concentration less than 75%. In contrast to V_3Si, no change in the composition of the superconductor at the interface with its oxide was observed within the resolution of our measurements which is consistent with the fact that excellent tunnel junctions have sometimes been made with the native oxide of Nb_3Sn.[7] Nevertheless, we observed higher subgap currents in tunnel junctions with some base electrode oxidation due to exposure to humid air.

Figure 2 shows the current-voltage characteristic of an evaporated Nb_3Sn junction with 20 Å of Al_2O_3, 12 Å of Al, and no base electrode oxides. The transition temperature of this particular sample was about 0.1K wide at 17.5K. However, the width of the gap, 0.6 mV, was typical of our junctions and those made by Rudman and co-workers.[8] The midpoint of the Nb_3Sn gap, 3.25 meV, corresponded to $2\Delta/kT_c = 4.3$ which was also in agreement with data in reference 8. Although there was some leakage current even below the PbBi gap, the ratio of I(6 mV)/I(3 mV) = 60. Junctions which had similar XPS data had ratios from 35 to 80 which were comparable to Rudman's Nb_3Sn-based junctions with oxidized silicon barriers but with higher leakage below the PbBi gap and perhaps lower excess conductance below the sum of the gaps.[9]

Curve 747956-A

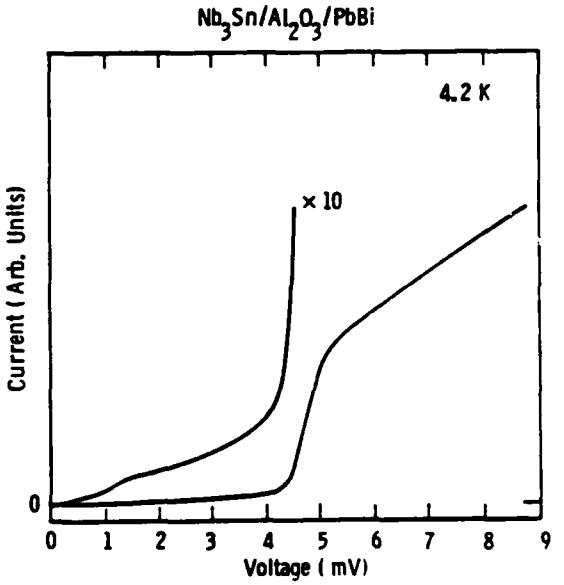

Figure 2 – Quasiparticle tunneling characteristic for a Nb_3Sn junction with an oxidized, evaporated Al barrier and a PbBi counterelectrode.

In contrast to the samples which underwent a standard oxidation, identical bilayers which were left for several days in humid air before counterelectrode deposition had barriers with 25 Å of Al_2O_3 and 15 Å of a mixture of niobium and tin oxides. Values of I(6 mV)/I(3 mV) were 3 to 5. Despite having a thicker barrier, there was no increase in the junction resistance above the sum of the gaps, R_n. Therefore, the additional oxidation affected the electrical properties of the barrier as well as the surface of the Nb_3Sn.

The V_3Ga samples had surface compositions similar to the bulk except for the sample with 11 Å of oxide growth. The oxide layer was deficient in vanadium oxide and the adjacent superconductor showed a small increase in Ga concentration. Junctions formed on samples 114-A1

and B1 had similar characteristics. However, the XPS measurements were made after the counterelectrode and insulator layers were stripped in acetic acid and acetone so oxidation of the V_3Ga probably occured only after the junctions were measured. The tunneling data will be published separately.

The importance of avoiding the deleterious effects of A15 oxidation is analogous to the same need for Nb-based junctions. We observed a degradation of tunneling characteristics when Al barriers were too thin to protect underlying Nb base electrodes or when some oxidation occurred before the Al was deposited in agreement with a number of others such as Wolf.[10] However, the mechanism which leads to a weakly superconducting surface layer in several A15 materials is an atomic segregation rather than the suboxide formation that occurs at a niobium/niobium oxide interface.

Tunneling Barrier Structure

XPS measurements have been useful but not sufficient indicators of junction quality. Some of our tunneling results have depended strongly on the crystallinity of the barrier which was a function of the base electrode structure and the deposition technique. Amorphous and crystalline oxide barriers have appeared to be identical by XPS analysis but consistently produced different tunneling results. Figure 3a is a Reflection High Energy Electron Diffraction (RHEED) pattern from the surface of 60 Å of Nb_3Sn evaporated on epitaxial-grade sapphire of unknown orientation at 900°C. Figure 3b shows that the pattern did not change except that the spots became sharper after 2000 Å were deposited. The single orientation which we have tentatively identified as (111) indicated that the film was very highly textured even after just 60 Å were grown. The probable reason we obtained such well-ordered material was that the pressure during evaporation was $< 10^{-9}$ torr.

Thin overlayers of Al or Y which were deposited on such highly textured films of either Nb or Nb_3Sn generally displayed RHEED patterns such as that shown in Figure 4a for a 30 Å thick Al layer deposited at 75°C on Nb_3Sn. The I-V curve in Figure 2 was from this type of structure. The RHEED pattern in Figure 4b was from a 40 Å polycrystalline Al layer deposited on a polycrystalline Nb base.

The type of RHEED patterns obtained and their relation to subgap tunneling currents for a number of base electrode/barrier configurations are summarized in Table 2. The ratio I(6 mV)/I(3 mV) is used as a measure of junction quality [I(4 mV)/I(2 mV) for Nb]. Patterns such as the one shown in Figure 4a are designated HT for highly textured. Polycrystalline patterns and patterns indicative of amorphous surface layers are labeled PC and AM, respectively. Overlayers formed on superconductors with HT surfaces had a diffraction pattern showing a single orientation but with spacings characteristic of the overlayer crystal structure. After oxidation there was still a single orientation but the pattern reflected the oxide's structure.

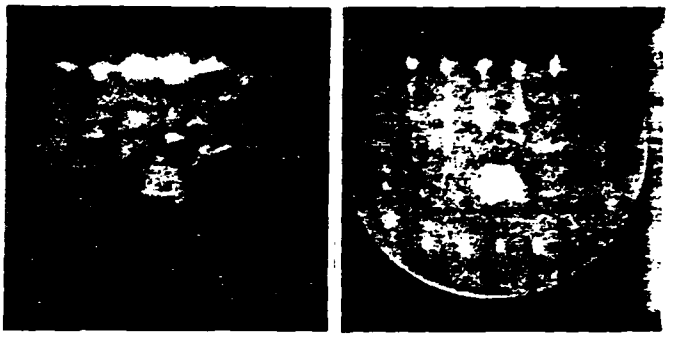

(a) 60 Å Nb_3Sn (b) 2000 Å Nb_3Sn

Figure 3 – (a) RHEED pattern of the surface of a highly-textured 60 Å thick Nb_3Sn film grown on epitaxial-grade sapphire. (b) RHEED pattern of the surface of the same film after 2000 Å were deposited.

Single-orientation Al barriers evaporated on Nb made poor tunneling barriers in a number of experiments although they worked well for Nb_3Sn and appeared from XPS measurements to be identical to sputtered barriers. On the other hand, sputtered Al barriers have worked well on Nb regardless of their structure. The surface of one group of evaporated Nb/Al bilayers was bombarded after oxidation with 600 eV argon ions for 15 minutes at 0.5 $\mu A/cm^2$. The Al_2O_3 became amorphous and the subgap currents were lower. There was no change in the XPS spectra due to the ion milling. A similar treatment of yttrium oxide barriers has not yet been tried.

The last columns of Table 2 compare the oxide barrier thickness from XPS with parameters fitted to the quantum mechanical tunneling theory derived by Simmons.[11] The ratio of the current to the voltage should be linear in the voltage squared if the low-voltage limit of Simmons' model is used. The tunneling current was fitted to a two-term polynomial function of voltage up to 0.4V. The

Table 2 – Relation between RHEED Patterns and Junction Quality

Base Material/ RHEED	Barrier before Oxidation/ RHEED	RHEED after Oxidation	I(6 mV)/ I(3 mV)	Oxide Thickness (Å)		Barrier Height, $\bar{\phi}$ (eV)
				XPS	S(Simmons)	
ev. Nb_3Sn/HT	ev. Al/HT	HT	30 to 80	20	16	1.4
	sp. Al/HT	HT	--*	20	--	--
ev. Nb/HT	ev. Al/HT	HT	2 to 5	18	--	--
	ev. Al/HT	AM*	15	18	27	1.0
	ev. Y/HT	HT	2 to 4	43	16	1.9
	sp. Al/HT	HT	30	18	14	2.4
sp. Nb/PC	sp. Al/PC	--	30 to 60	18	14	2.0

*Nb_6Sn_5 phase present in these samples.

*Ion-milled after oxidation.

AD-A163 053 THIN FILM TECHNOLOGY OF HIGH-CRITICAL-TEMPERATURE 2/2
SUPERCONDUCTING ELECTRO (U) WESTINGHOUSE RESEARCH AND
DEVELOPMENT CENTER PITTSBURGH PA J TALVACCHIO ET AL.
UNCLASSIFIED 11 DEC 85 85-9C9-TUDEV-R1 N00014-82-C-0617 F/G 9/5 NL

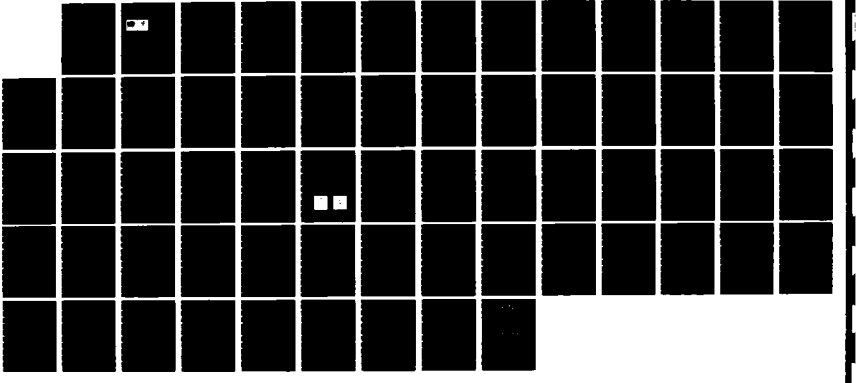

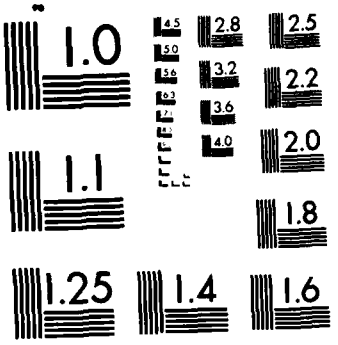

barrier height, $\bar{\phi}$, and barrier width, S, were calculated from the fitting parameters following Simmons. An indication of how well a rectangular barrier simulated real barriers is given in Figure 5 for a highly textured Al barrier on Nb_3Sn where a plot of I/V versus V^2 is shown to be a reasonably straight line. At voltages greater than 0.4V where the low-voltage limit no longer applies, the current rises faster than V^3. An asymmetry about zero bias was observed for all samples but was small enough that it will not be discussed here. Rowell found S ≈ 14 Å and $\bar{\phi}$ = 1.95 eV for Al_2O_3 barriers on Al.[12] Our samples had a range of barrier heights with values which were significantly higher for sputtered barriers than for evaporated barriers.

(a) Highly textured 30 A thick Al barrier

(b) Polycrystalline Al barrier

Figure 4 – (a) RHEED pattern of a highly-textured Al film 30 Å thick evaporated on Nb_3Sn. (b) RHEED pattern of a polycrystalline Al overlayer 40 Å thick with no preferred orientation.

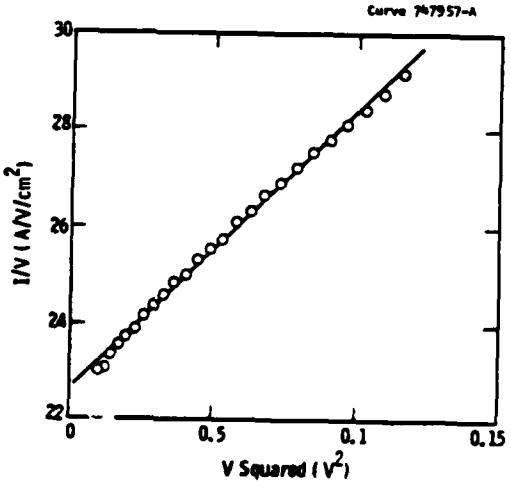

Figure 5 – I/V versus V^2 for a Nb_3Sn junction with an oxidized, evaporated Al barrier fitted by a straight line following Simmons' low-voltage limit for tunneling through a rectangular barrier.

For Al, the barrier widths from Simmons' model were slightly smaller than those measured by XPS. XPS measurements of barrier thickness taken with the detector at glancing angles to the sample surface indicated that the barriers may not have been of uniform thickness, particularly for sputtered overlayers.[13] Although the Simmons' model should have reflected the thinner parts of the barrier and the XPS data measured an average thickness, the differences were too small to confirm the glancing angle XPS. The samples with evaporated Al_2O_3 barriers which were milled with an ion beam to make them amorphous had a broad (27 Å), low (1.0 eV) barrier. Ruggiero and co-workers suggested that such a barrier shape indicates the presence of a degraded base electrode surface layer.[14] The samples with amorphous barriers had higher leakages than those with sputtered barriers but had no decrease in the size of the gap. The barrier width calculated for evaporated Y should be considered as a lower limit of the value which might be obtained for a low-leakage junction.

Conclusions

1. Atomic segregation of the components of A15 compounds upon oxidation causes a degradation of A15-based tunnel junctions.

2. Evaporated, highly textured Al overlayers produce low-leakage barriers on A15 Nb_3Sn. In contrast, Al evaporated on Nb results in high leakage currents.

3. Barriers formed by oxidation of Al evaporated on Nb_3Sn exhibit a barrier height lower than those of Al sputtered on Nb.

4. The crystallinity of Al sputtered on Nb does not affect the leakage current.

5. Although neither is sufficient by itself, XPS and RHEED indicate the quality of artificial tunneling barriers during fabrication on A15 base electrodes.

Acknowledgements

The authors want to acknowledge the assistance of K. Goodwill with V_3Si depositions and Mrs. M. B. Cross with preparation of this manuscript.

References

1. M. Gurvitch and J. Kwo, in Adv. in Cry. Eng. – Mat., 30, p. 509, 1984.
2. D. A. Rudman and M. R. Beasley, Appl. Phys. Lett., 36(12), p. 1010, 1980.
3. H. Ihara, Y. Kimura, H. Okumura, K. Senzaki, and S. Gonda, Adv. in Cry. Eng. – Mat., 30, p. 589, 1984.
4. T. A. Carlson and G. E. McGuire, J. Elec. Spec. and Related Phen., 1, p. 161, 1972.
5. A. Ermolieff, M. Girard, C. Raoul, C. Bertrand, and T. Minh-duc, presented at the 6th Symp. on Appl. Surface Anal., Dayton, Ohio, 1984.
6. D. R. Penn, Elec. Spec. and Related Phen., 9(1), p. 29, 1976.
7. D. A. Rudman, R. E. Howard, D. F. Moore, R. B. Zubeck, and M. R. Beasley, IEEE Trans., MAG-15(1), p. 148, 1979.
8. D. A. Rudman, F. Hellman, R. H. Hammond, and M. R. Beasley, J. Appl. Phys., 55(10), p. 3544, 1984.
9. D. A. Rudman, Ph.D. Thesis, Stanford Univ., 1982.
10. E. L. Wolf, J. Zasadzinski, J. W. Osmun, and G. B. Arnold, J. of Low Temp. Phys., Vol. 40(1,2), p. 19, 1980.
11. J. G. Simmons, J. Appl. Phys., 34, p. 238, 1963.
12. J. M. Rowell in Tunneling Phenomena in Solids, ed. E. Burstein and S. Lundqvist, Plenum Press, New York, 1969.
13. J. Talvacchio, A. I. Braginski, and M. A. Janocko, presented at March Mtg. of the APS, Detroit, 1984.
14. S. T. Ruggiero, G. B. Arnold, E. Track, and D. E. Prober, Proc. 17th Intl. Conf. on Low Temp. Phys., North-Holland, Amsterdam, 1984.

APPENDIX C

NEW MATERIALS FOR REFRACTORY TUNNEL JUNCTIONS: FUNDAMENTAL ASPECTS *

A. I. Braginski, J. R. Gavaler, M. A. Janocko,
and J. Talvacchio
Westinghouse R & D Center, Pittsburgh, Pennsylvania 15235

Introduction

The status in 1980 of material issues and related fabrication techniques for Josephson junction electronics was presented in a comprehensive background paper by Beasley and Kircher (1). Since that time the research and development activities in several countries have been focussed mostly on tunnel junctions with refractory-metal electrodes (niobium, alloy or compound) that are free of the thermal cycling instability. This instability, characteristic of Pb-alloy electrodes, was discussed in Ref.1. A concise 1984 review of progress in fabrication of tunnel junctions with refractory electrodes was given by Raider (2). He concentrated on niobium electrode junction problems, and provided a very complete list of references. The purpose of our paper is to review the fundamental material problems specific to tunnel junctions with high-critical-temperature refractory electrodes fabricated of materials such as niobium nitride and Nb- or V-based A15 structure compounds. The superconductor itself and the barrier material are addressed, while device and circuit fabrication by photolithographic and other techniques is not treated. The now more-familiar niobium-based junction material aspects (2) are referred to for comparison. We also report on our approach to the development of junction device technology. In this approach, the crystalline structure, composition and physical uniformity of films and substrates

* Supported in part by the AFOSR, Contract No. 49620-85-C-0043. Part of past work supported by ONR, Contract No. N00014-82-C-0617.

are investigated in situ by surface analytical methods, prior to the deposition of the subsequent layer(s) and usually without breaking the vacuum. The feasibility of all-epitaxial junctions is probed.

Important Physical Parameters

Superconductors

The superconductor electrical parameters most important to tunnel junction performance are: critical temperature [T_c], energy gap [Δ], superconducting coherence length [ξ_s] and penetration depth [λ]. The T_c within the coherence length from the barrier interface determines the maximum operating temperature: $T_{op} < T_c/2$, which is desired to be as high as possible. The energy gap is probed by the tunneling effect within the distance ξ_s from the barrier, and a high Δ value is desired in almost all applications. The coherence length sets the film-depth scale for tunneling, and should be as high as possible to minimize the deleterious effect on T_c and Δ of various phenomena occuring at or near the interface with the barrier. Gap degradation within ξ_s from the interface will invariably result in an increased subgap conductance. The magnetic field penetration depth should be the lowest possible, to minimize flux trapping in tunnel junctions, and to maximize the signal propagation velocity in superconducting transmission strip lines that connect the junction devices.

It is clear from the list of requirements given above that all high-T_c, high-κ, type II superconductors, which have intrinsically $\xi_s << \lambda$, suffer from a common and serious problem of short ξ_s and long λ. In the Ginzburg-Landau dirty limit: $\xi_s(0) \propto (\rho_n T_c)^{-1/2}$ and $\lambda(0) \propto (\rho_n T_c)^{1/2}$. Only to the extent that ξ_s and λ are dependent on the normal- state resistivity, ρ_n, can the ratio ξ_s/λ be maximized by fabricating the material close to the clean limit, with as long an electron mean free path as possible. The normal electron scattering by impurities, voids, grain boundaries, and crystalline disorder all conspire to make it a difficult task,

especially for the counterelectrode superconductor deposited on the barrier. Table 1 compares typical superconducting parameters of selected B1 and A15 materials with those of Nb and Pb. The ranges in T_c and $\Delta(4.2)$ values are delimited by typical and best experimental results obtained in polycrystalline thin base electrodes of a tunnel junction. The ranges in ξ_s and λ are delimited by either experimentally observed high and low resistivities (3) or a direct measurement of λ .

Table 1. Superconducting Parameters of Selected Materials

Material	T_c, K	$\Delta(4.2)$, meV	$\xi_s(4.2)$, nm	$\lambda(4.2)$, nm
NbN	14 to 16	2.4 to 3.0	4 to 7	600 to 300
Nb_3Sn	17 to 18	3.0 to 3.4	~ 3	90 to 60
Nb_3Ge	18 to 21	3.4 to 3.8	~ 3	?
V_3Si	15 to 16	2.5 to 2.6	~ 3	110 to 60
Mo-Re	12 to 15	1.7 to ?	20(bcc)	80 to 60
Nb	9 to 9.3	1.3 to 1.6	10 to 30	85
Pb	7.2	1.3	90 ?	40

Barriers

The rectangular barrier approximation is used here for the description of material properties (4). This approximation does not apply to barriers which are inhomogeneous or which vary in some way as the barrier thickness is traversed, but it does apply to most single material, uniform barriers investigated thus far. The barrier properties important to junction performance are: the average barrier height ($e\bar{\phi}$), its width (S), the leakage current below the gap voltage, the low frequency 1/f noise, and the specific capacitance. The average height is determined by the electron work function(s) of the two electrodes for the insulator used. For a given S, $e\bar{\phi}$ defines the tunneling resistance above the gap voltage, R_n, usually given as $R = R_nA$, where A is the junction area.

The insulating barrier width (S) is usually comparable to its physical thickness (s). Since the junction critical current, I_c, is an exponential function of S, and practical S values are in the range of 1 to 10 nm (at least for oxides), the control of s and S to attain narrow I_c tolerances is the single biggest challenge of current junction fabrication technologies. For low barrier height materials, the control of barrier thickness may not need to be as precise. Both $e\bar{\phi}$ and S can be obtained by fitting the experimental I-V data to Simmons' theoretical low (intermediate) voltage equation (4).

Mechanisms of the subgap leakage and 1/f noise, that originate in the barrier itself, are presently under intense investigation and are not yet fully understood. The most frequent sources of leakage are resistive microshorts, typical of a thin barrier layer with a highly nonuniform thickness. Conducting microchannels are also attributed to defects producing electron states localized within the barrier and/or at its interfaces. In some cases, these states can trigger the resonant tunneling mechanism (5,6). It was proposed most recently that the low frequency noise is also correlated with the single defect states (7), and the resulting leakage. A barrier quality factor (Q) can thus be defined as the ratio of junction currents at specified voltages above and below the gap. Finally,the specific capacitance or the dielectric constant of the insulator is a material property that depends upon the chemistry, crystallinity and morphology.

Most of the recent systematic barrier studies concentrated on "native" oxides formed by oxidizing the Nb base electrode. For reasons discussed below, however, junctions of high-T_c compounds are and will be fabricated, in most cases, with artificial i.e. deposited barriers. Elemental overlayers of low-$e\bar{\phi}$, amorphous silicon (a-Si), hydrogenated a-Si:H, and crystalline Ge can be deposited to form relatively thicker, or low-R_n barriers (8,9). Higher-$e\bar{\phi}$, thin insulator barriers can be deposited either directly in their final form, as oxides (10), nitrides (11) and fluorides (12), or as elemental Si (13) or metallic overlayers (14) subsequently

subjected to a surface oxidation treatment. In this last case an unoxidized elemental/metallic proximity underlayer is usually allowed to remain after the oxidation process. If not, the base can become partly oxidized.

Table 2 shows examples of experimentally determined properties of different low-leakage ($Q > 10$) barriers on NbN base electrode, and with either Pb-alloy or NbN counterelectrode. A few examples of the effect of alternative base superconductors are also included. The resistance and barrier height

Table 2. Examples of Barrier Properties

Base/ Barrier Material	Resistance (Ω-cm^2)	Barrier Thickness (nm)	Barrier Height (eV)	Specific Capacitance (μF/cm^2)	Reference
Pb (Alloy) Counterelectrode					
NbC_xN_y/native oxide	10^{-6} to 10^{-5}	1.9	<< 0.25	(10)	
NbN/native oxide	10^{-4} to 10^{-3}	1.9	0.25	(10)	
NbN/Al_2O_3	10^{-3} to 10^{-2}	1.8	0.8	(6)	(15)
NbN/MgO	10^{-1} to 10^{+0}	2.5	1.0	(5)	(16)
NbN/Y_2O_3	10^{+2}	4.1	0.4	?	
NbN Counterelectrode					
NbN/native oxide	2×10^{-6}	1.9	?	10	(17)
NbN/SiO_2 (18)	10^{-8} to 10^{-2}	< 5	1.2	2	(18)
NbN/Al_2O_3	10^{-3} to 10^{-2}	2.4	0.4	(6)	
NbN/MgO	10^{-3} to 10^{-2}	2.3	0.5	(5)	
NbN/Nb_2O_5/MgO (10)	2 to 5 $\times 10^{-6}$	0.7	?	8	(10)
NbN/α-Si [/Nb] (19)	10^{-6} to 10^{-5}	4 to 5	0.1	4	(19)
NbN/Ge [/Nb] (9)	10^{-6} to 10^{-5}	3 to 6	?	2 to 5	(9)
Pb (Alloy) Counterelectrode					
Nb/Al_2O_3	10^{-2} to 10^{-1}	1.6	2.0	(6)	
NbN/Al_2O_3	10^{-3} to 10^{-2}	1.8	0.8	(6)	
Nb_3Sn/Al_2O_3	10^{-1} to 10^{+1}	2.0	1.2	(6)	

data are derived from our measurements, except where a reference is indicated in the first column. Specific capacitances in brackets are estimates, usually based on Fiske steps determinations by various authors. The variation of resistance over eight orders of magnitude reflects the effect of barrier height and the thickness variation, the latter typically within a factor of 2 to 3.

Fundamental Material Problems

General film properties such as density, crystallinity, morphology and smoothness, and thermal expansion compatibility with the substrate and other layers, are of obvious importance to the junction fabrication, independent of the material type used. Many fundamental problems, however, are strongly related to surface and interface effects in the thin film superconductor and the barrier layer. We intend to concentrate on these, especially when specific to compound superconductors. We begin, however, with a look on the "bulk" compositional and phase homogeneity problem since it is specific to compound or alloy superconductors. We then proceed with other questions, as they emerge in the base electrode/barrier/counterelectrode fabrication sequence.

Superconductor Homogeneity

During the deposition of binary and multicomponent systems, fluctuation of the atomic species ratio is occuring in time and space thus leading to local variations in the film composition and properties, on both gross and fine scales, that are not eliminated by interdiffusion. The consequence for a tunnel junction is a broadening of the gap width in the I-V characteristic, and an increase in the conductance above the gap of the other electrode. Within the bulk phase stability field of high-T_c A15 (A_3B, where A is Nb or V, and B = Sn, Al, Ga, Ge, Si) or B1 (AB, where A is Nb and B the sum of nonmetallic components: N, CN, or OCN) phases, the T_c and Δ decrease by 10 to 15% per each atomic percent deviation from stoichiometry toward higher A/B values. When the preset

atomic ratio fluctuates toward too low A/B values, the boundary of superconducting phase stability is usually traversed and a second phase(s) precipitates. The presence of such precipitates in the film surface is likely to cause surface roughness leading to perforations in the barrier overlayer that are prone to short the junction, as observed for Nb_6Sn_5 precipitates in Nb_3Sn (20).

Typical apparatus- and process-related causes of the fluctuation are: the limited sensitivity and accuracy of the deposition rate control when depositing from separate atomic sources, or a broadly defined inhomogeneity of a composite source. The first effect can be dominant when co-evaporating A15 compounds from elemental electron-beam (e-beam) sources. The best result to date is the ± 1 at.% control attained through the use of Hammond's sophisticated e-gun feedback loop control (21). More typical is ± 3 to 5 at.%. Composite sources such as powder-metallurgical, arc-melted or segmented A15 sputtering targets may lead to film composition variations of many at.%. The homogeneity of sputtered deposits is relatively best when obtained by reactive sputtering from an elemental target. This consideration clearly favors reactively sputtered NbN over co-sputtered A15 films. Independent of these and other apparatus and process-related inhomogeneity causes, off-stoichiometric Nb_3Sn (22), V_3Si (23), and metastable A15's such as Nb_3Ge exhibit local inhomogeneities due to not yet understood thermodynamic instability effects.

While it is not always possible to attribute the gap broadening in high-T_c tunnel junctions to a specific, dominant cause, and effects such as the gap anisotropy may also be contributing, the best reported gap widths at 4.2K are: 0.5 to 0.7 mV in "phase locked" Nb_3Sn (20,24), or V_3Si (13) and, typically, over 1 mV in Nb_3Ge (25). These data contrast with < 0.3 eV in NbN-base junctions (8,26), and < 0.1 mV in Nb-base junctions (27). We refer to junctions without any pronounced proximity effect that could obscure the broadening (28). The contrast is seen in Fig. 1, which compares I-V characteristics of "the very best" Nb_3Ge (25,29), with those of Nb_3Sn and NbN-base junctions. At this time the only

Curve 750276-A

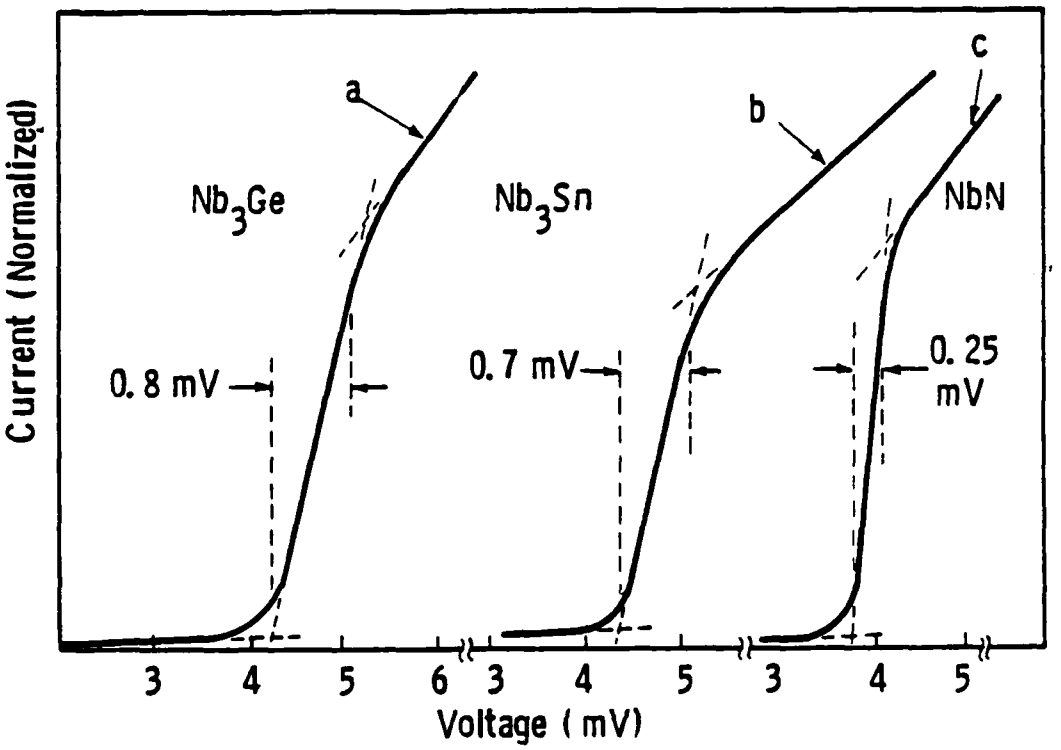

Fig. 1 Comparison of a quasiparticle I-V characteristic of "best" Nb_3Ge [after Kihlstrom (25), see also Michikami et al (29)] with those of typical Nb_3Sn and NbN: (a) $Nb_3Ge/SiO_x/Pb$, (b) $Nb_3Sn/Al_2O_3/Pb$, (c) $NbN/Al_2O_3/Pb$-Bi.

obvious course toward the A15 homogeneity improvement is through better control of co-deposition rates and other process parameters, most notably the substrate wafer temperature uniformity (25). Future research into A15 phase stability may shed more light on intrinsic limitations of A15 film homogeneity.

Surface atomic segregation

The x-ray photoelectron spectroscopy (XPS) study by Ihara et al (30), followed by our own work (24), has shown conclusively that the room-temperature surface oxidation of binary A15 compounds results in an atomic surface segregation such that atoms having a stronger affinity to oxygen migrate preferentially to the surface where they form oxides. Consequently, the layer underneath can be enriched in the other constituent beyond the A15 phase stability limit, as shown schematically in Fig. 2a. A major degradation of the energy

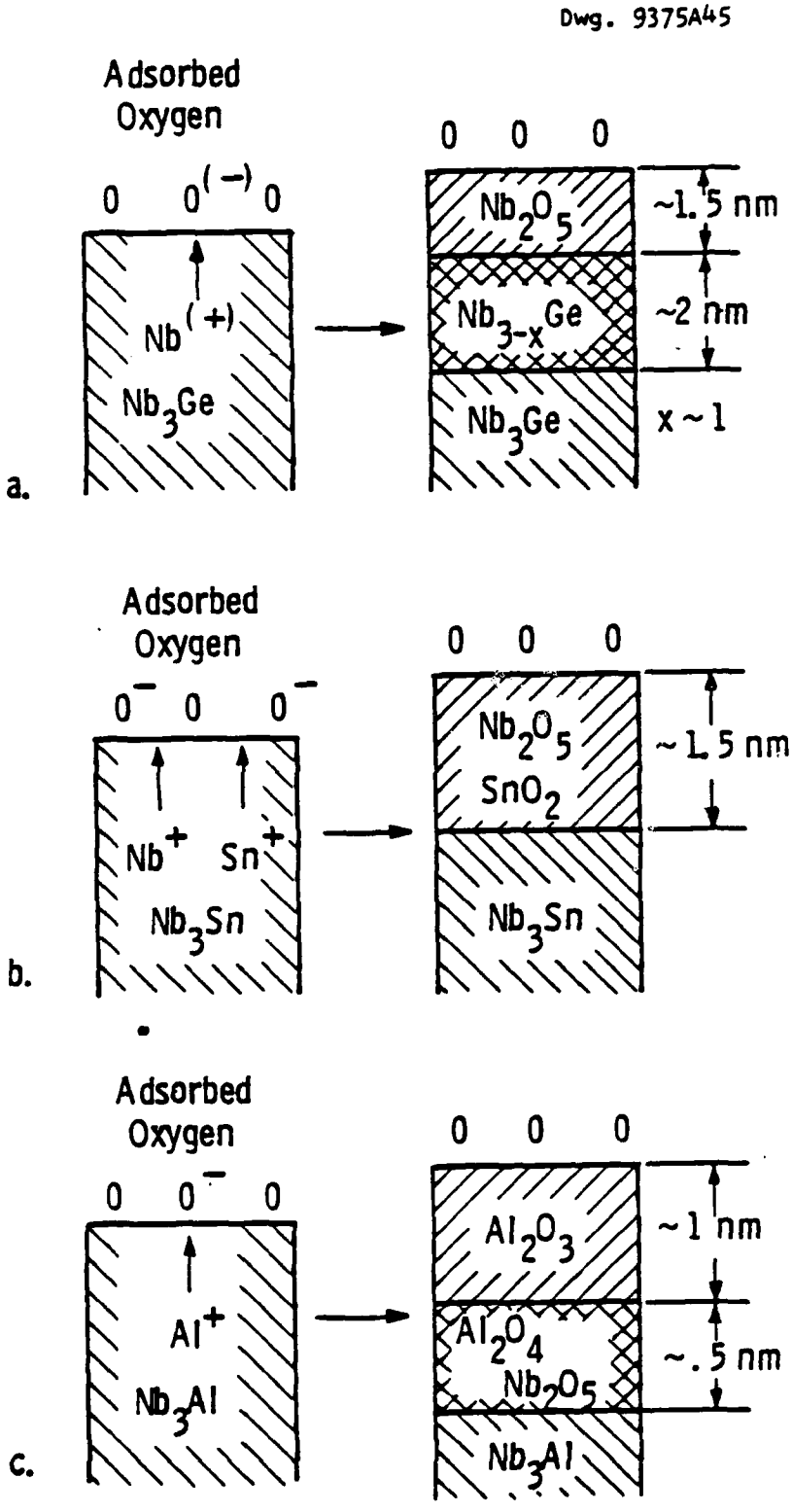

Fig. 2 Schematic diagrams of surface segregation cases derived from XPS results [after Ihara et al (30)].

gap and/or a formation of a proximity layer may thus result within the depth comparable to the coherence length. The use of a native oxide barrier would not be desirable in such a case. The effect of surface segregation can be explained by the Mott-Cabrera oxidation theory (31). According to the observations of Ihara et al, the extent of the segregation depends upon the difference in oxygen affinities (ionization potentials) of the constituent atoms. Strongest segregation was observed in V_3Si and Nb_3Ge. Much less pronounced segregation was seen in Nb_3Sn (Fig. 2b) and V_3Ga (24). A special case seemed to be that of Nb_3Al (Fig.2c) where a double (segregated) layer of oxides formed without any measurable segregation in the superconducting underlayer (30), so that a native oxide barrier could be contemplated here. Segregation may also be prevented or reduced by an intermediate compound layer formed on an A15 surface by reactive cleaning prior to oxidation (29). Generally, however, the segregation effect makes the formation of artificial, possibly non-oxide barriers in A15- base junctions very desirable. In contrast, no surface segregation is observed in NbN upon oxidation. The nitrogen escapes and a (predominantly) Nb_2O_5 layer remains. A native Nb-oxide barrier on NbN is, in fact, perfectly viable, although its low resistance, high capacitance, and a residual lower oxide underlayer make an artificial barrier preferable in most cases. We also found no surface segregation in Mo-Re alloys that crystallize in both α-Mo and A15 structures with T_c's up to 13 to 15K (32). According to our XPS data, however, almost no surface oxide forms on this superconductor, so that the use of an artificial barrier appears necessary (33).

Wetting and uniformity of coating

Excellent uniformity of the base electrode coating with an artificial barrier overlayer, 1 to 10 nm thick, is necessary to prevent the occurrence of pinholes capable of shorting the junction. Rowell et al showed that an extremely thin aluminum overlayer sputtered on clean Nb at ambient temperature and thermally oxidized, modifies the resulting barrier properties from "Nb-oxide-like" to "Al_2O_3-like" (14). Thicknesses below 1 nm, down to two monolayers, were found effec-

tive. Gurvitch and Kwo (27) interpreted this as an evidence of excellent Nb surface "wetting" by Al in accord with Miedema's interfacial energy model for a solid/liquid interface (34). Figure 3 shows direct XPS spectra evidence that upon oxidation a 1 to 4 nm thick Al overlayer suffices to fully suppress the formation of Nb-oxides underneath Al_2O_3, and possibly even scavenge oxygen from the Nb (35). Gurvitch and Kwo also obtained similar tunneling and XPS results for oxidized overlayers of Mg, Y and Er on clean Nb (36). Others obtained good tunneling characteristics with overlayers of oxidized a-Si on clean A15's (13,20), a-Si and a-Si:H on Nb and NbN (8,19), Ge on NbN (9) and oxidized Lu on A15 (37). Calculations based on (34) show indeed that the overlayer's tendency to wet Nb (and V) decreases in the order: Si, Ge, Al, Mg and Y but the differences in the interfacial energy are fairly small, and could be insignificant. Qualitatively, this may also be true for Nb- or V-containing compound surfaces although no model calculations exist for the compound/metal or compound/compound interface.

It should be recognized, however, that wetting is very strongly dependent upon the cleanliness of the wetted surface (34), and, therefore upon the deposition method and its parameters. Ultra-high-vacuum (UHV) conditions, as well as other means promoting the uniformity of coating, should be benefical. For example, the results quoted above for Al, Mg, and Y were obtained by sputtering on substrates rotating or oscillating with a period much shorter than the time of one monolayer deposition. Such substrate motion is clearly improving the uniformity of the barrier, and may be critical for small sputtering sources, at typical background vacuum levels of 10^{-6} to 10^{-5} Pa. Another effect of possible significance is that of grain boundaries in the wetted base, and the crystallinity of the wetting metal. Miedema's model assumes a liquid, best approximated by an amorphous overlayer. Angle-dependent XPS analysis makes it possible to estimate either the overlayer's thickness fluctuation, on a perfectly smooth substrate, or the roughness of the substrate with a smooth overlayer. Grundner has modeled both cases for the XPS-measured thickness, s, as a function of θ, the angle

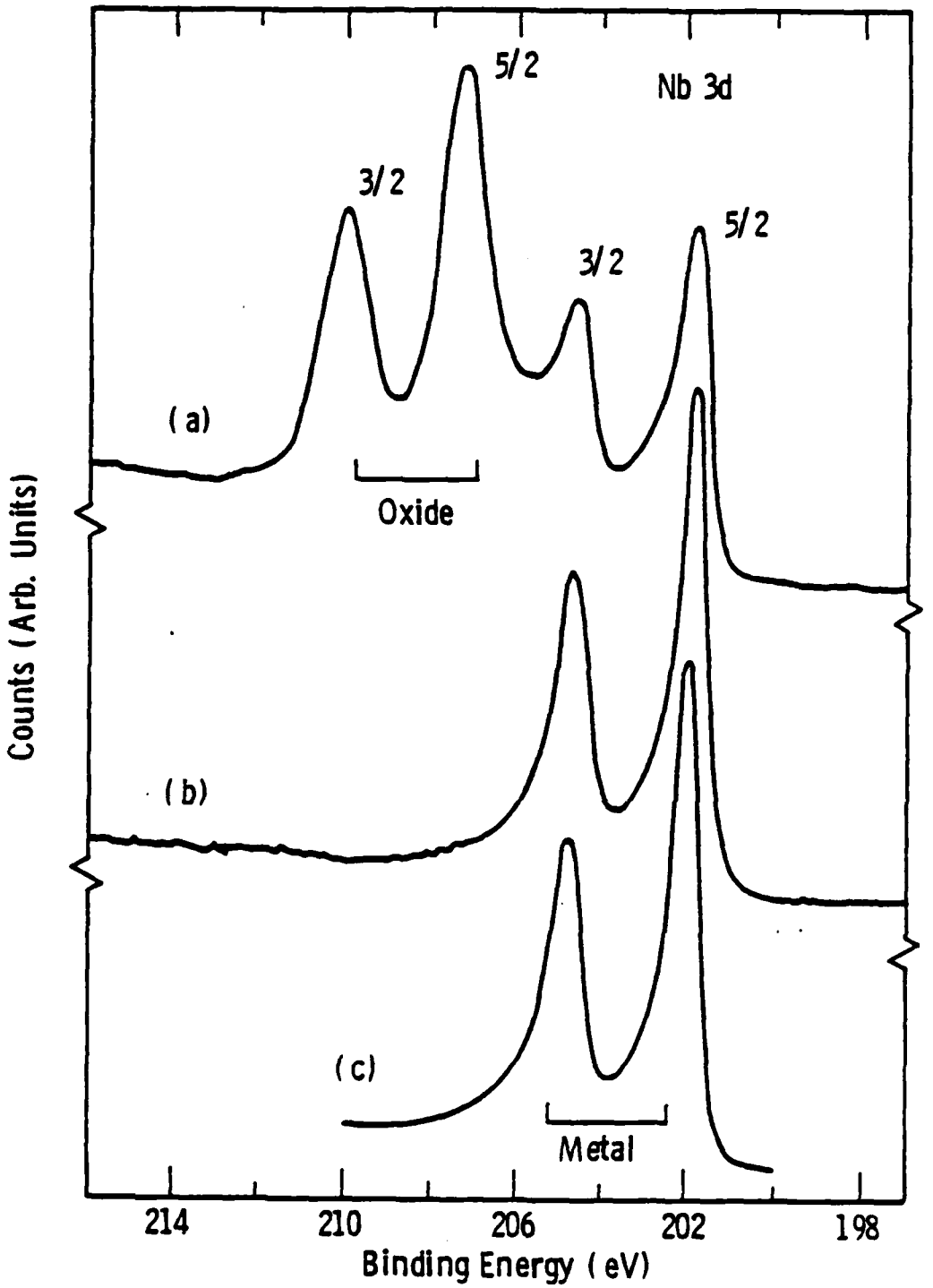

Fig. 3 The XPS spectra of Nb: (a) air-oxidized polycrystalline Nb, (b) air-oxidized Nb/Al; Al is .9 to 3.8nm thick, (c) clean polycrystalline Nb [after Kwo et al (35)]

between normal to the film and the electron energy spectrometer (38). A perfectly smooth overlayer on a smooth substrate gives s independent of θ. Roughness increases s at low $\theta < 45$, and decreases at high $\theta \to 90$. Thickness variation produces only the latter effect. Unfortunately, the signatures of these two effects can be convoluted when both are present. We thus determined the thickness fluctuation in a sputtered thin layer of the best-wetting, amorphous Si sputtered by Graybeal on an amorphous Mo-Ge thin film of extreme smoothness inferred from the electrical resistivity data (39). The XPS estimate, inferred from the thickness vs. θ dependence shown in Fig. 4, indicated that the amplitude of the fluctuation was comparable to the Si-film thickness. Thin Si, Al, and Y barrier overlayers sputtered or evaporated on polycrystalline V_3Si, Nb_3Sn, V_3Ga and Nb all showed larger

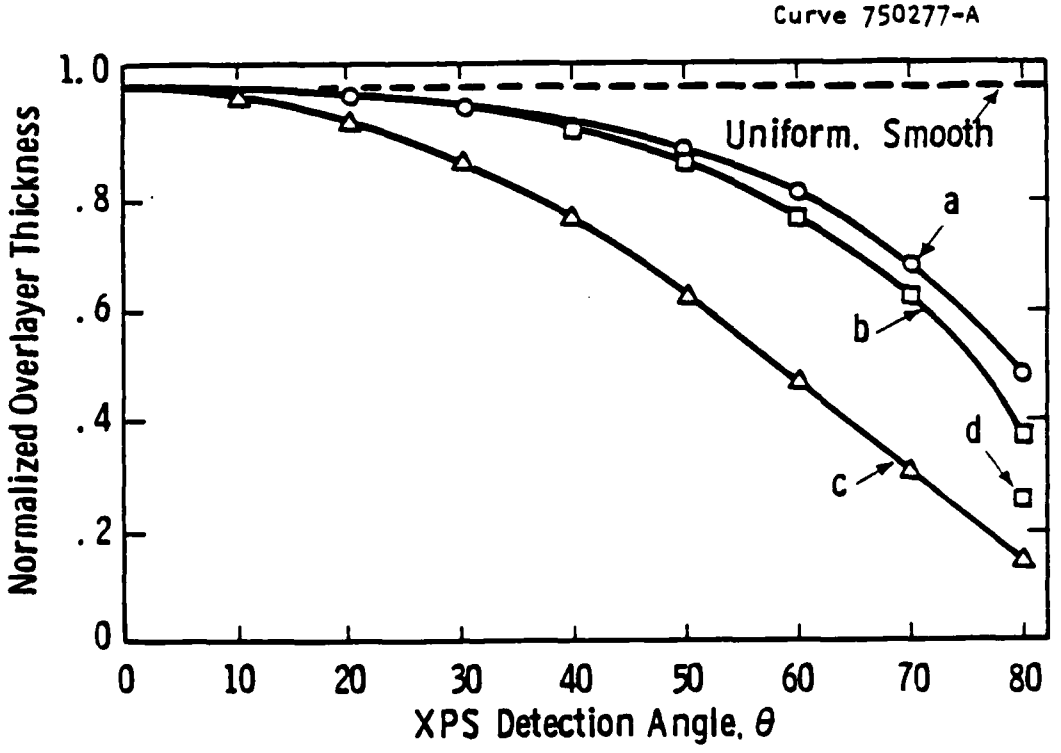

Fig. 4 Overlayer thickness vs XPS detection angle: (a) calculation for a Gaussian distribution of thickness, = 1, (b) Si overlayer on MoGe base prepared by Graybeal, (c) Al overlayer on polycrystalline, 300 nm thick Nb base, (d) Al overlayer on single crystal Nb film.

thickness fluctuations and/or base roughness. Within this group, the least effect was seen in overlayers on single crystal, atomically smooth Nb films thus indicating that roughness of the polycrystalline base was indeed obscuring the overlayer thickness variation. Although the XPS results could give only an upper bound to this variation, the Si/Mo-Ge XPS experiment has shown convincingly that overlayer barriers are not uniform in thickness. Consequently, tunneling could be largely determined by the thinnest regions. Would their thickness approach zero then the junction will either be shorted by pinholes or defined, in part, by the native oxide of the base, with a resulting inhomogeneous, "patchy" barrier. Indeed, in the case of oxidized Al-overlayers we observe a high incidence of shorts in junctions with Mo-Re base that does not oxidize. In contrast, with Pb-Bi counterelectrodes, the same overlayers on NbN give a nearly 100% yield of high-quality junctions. The Mo-Re thus serves as a test vehicle for the overlayer uniformity. The importance of optimizing the thin overlayer uniformity by process parameters such as the partial pressure of impurities during deposition, the size of the source (target), substrate motion, and also its temperature, is critical for junctions with narrow I_c tolerances.

Interface diffusion and reactions

For artificial barriers, strong bonds between the base electrode and the overlayer are necessary to make wetting possible (34). An excessive interdiffusion, and a chemical reaction, however, will degrade the energy gap in the base and may also result in a deteriorated barrier. The latter is perhaps less of a problem for oxidized metal overlayers, as the interdiffusion occurs between the base and the metallic proximity underlayer left after the oxidation, without necessarily affecting the oxide itself. Kwo *et al* inferred from XPS thickness data that a part of the Al- or Mg-overlayer deposited on Nb at an ambient temperature was "lost" by thermally activated diffusion along the Nb-base grain boundaries (35,27). The loss was, indeed, much reduced on coarse-grained Nb. Our XPS measurement of oxide (Al_2O_3) and Al-underlayer thickness on a Nb single crystal film

heated at 10^{-7} Pa (Fig. 5) showed no measurable loss of Al, thus no bulk diffusion, up to 400-500 C, and no change in the oxide thickness up to 750 C. This illustrates the sturdiness of the oxide, and suggests that such barriers could be compatible with high-temperature processing, necessary for Al5-counterelectrode junctions. In contrast, in-situ XPS of thermal Nb_2O_5 on Nb showed that heating to 850 C in 10^{-8} Pa eliminates the oxide entirely.

Curve 750275-A

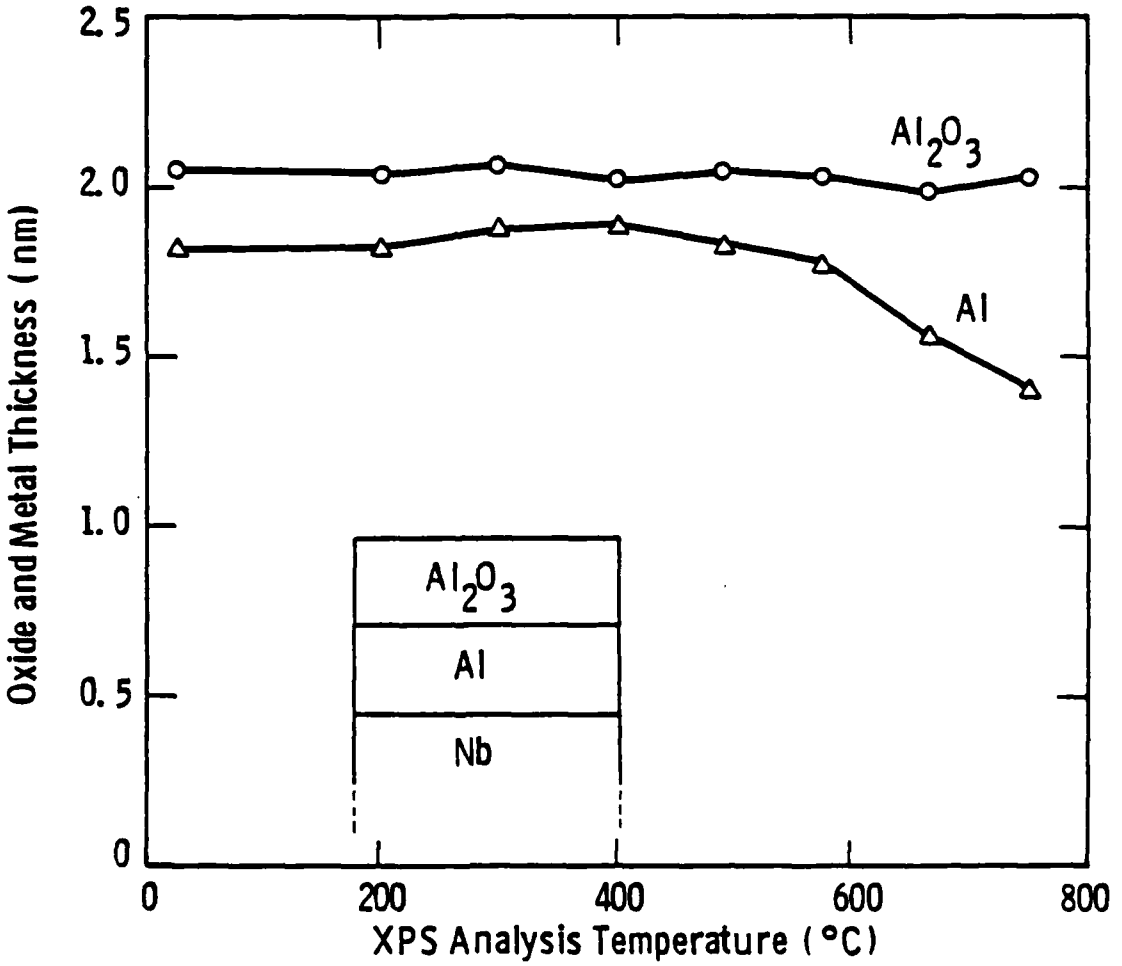

Fig. 5 Thickness of partly oxidized Al overlayer on single crystal Nb vs the XPS analysis temperature.

No deterioration of the energy gap in Nb with in-diffused Al or Mg was observed, due to the long coherence length of Nb (27). We observed, however such a deterioration in NbN (short ξ_s) with Mg-overlayers. Figure 6 compares our typical

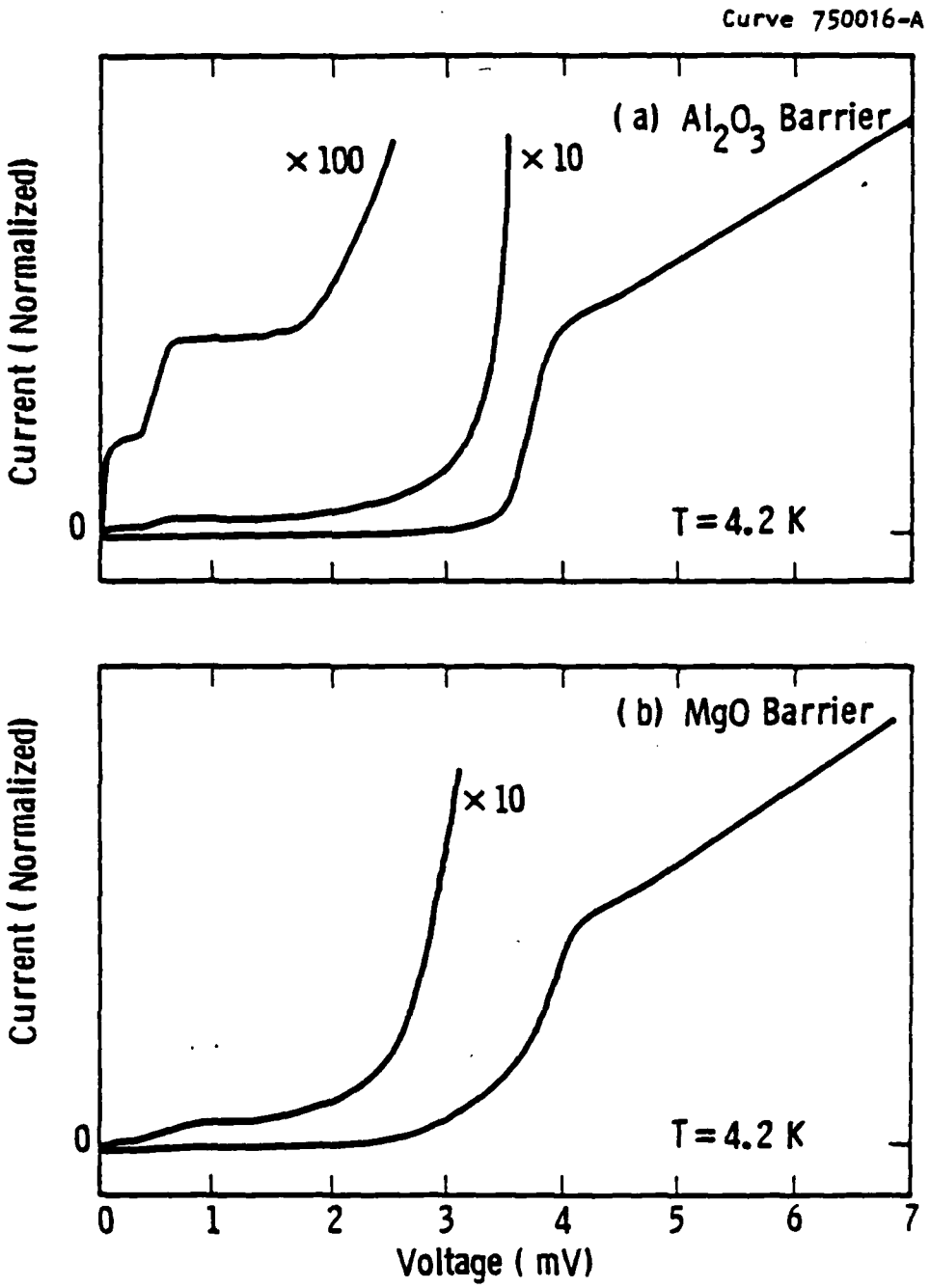

Fig. 6 Comparison of quasiparticle I-V characteristics of NbN-base junctions with Pb-Bi counterelectrode: (a) Al/Al_2O_3 barrier, (b) Mg/MgO barrier.

quasiparticle I-V characteristics of NbN/Al/oxide/Pb-Bi and NbN/Mg/oxide/Pb-Bi junctions fabricated at room temperature. The high subgap leakage current in the latter is not due to the barrier itself, since the I-V slope is nearly zero at

zero bias. That the magnesium either diffuses into or reacts with NbN at a rate higher than that of Al, was confirmed by XPS. The Mg-peak in XPS spectra of NbN/Mg/MgO disappeared upon heating in-situ to 300 C, leaving only MgO and NbN (Fig. 7) while in NbN/Al/Al_2O_3 no loss of Al was observed. Atomic radius of Al (0.14 nm) is smaller than that of Mg (0.16 nm), and Al is soluble in Nb while Mg is not (40). Hence, a chemical reaction is more probable than the physical interdiffusion. Van Vechten and Liebman discussed a reaction of Al with NbN to form AlN as likely to degrade the NbN gap (41). A reaction of metallic Mg with NbN to form MgN is even more feasible thermodynamically. To avoid it, the deposition of oxide is preferable, as indicated by the most recent results by Shoji et al who fabricated all-NbN junctions with rf-sputtered MgO barriers (10). It is not clear, however, whether the uniformity of coverage could be as good for oxide deposits as it is for metallic overlayers. Generally, the interdiffusion will be reduced for metallic overlayers having a large atomic radius, r. Lack of solid state solubility is also desirable. Yttrium meets both these criteria. We thus compared by XPS the metallic overlayer loss vs temperature for Al (r = 0.14 nm) and Y (r = 0.18 nm) on polycrystalline Nb and V_3Si. Figure 8 shows no loss of Y at room temperature and a lesser loss than that of Al at 250 C. The Y-oxide barrier may thus become especially attractive for high-temperature fabrication of A15 junctions. On the other hand, however, Kroger et al showed that Ge and Si, having smaller atomic and ionic radii, can be chemical-vapor-deposited (CVD) on NbN at temperatures up to 800 and 600 C, respectively, without "obvious signs of reaction" (9). Alternative approaches to the interface diffusion and/or reaction problem are, therefore, feasible.

Barrier oxidation, hydroxides

Grundner, Halbritter, and others performed extensive studies of thermal (room temperature) native oxide formation on polycrystalline niobium using XPS as the main experimental tool (42,43). Phenomenologically, the essence of their results is that, underneath the surface Nb_2O_5, an underlayer of lower oxides is forming by oxygen diffusion into niobium.

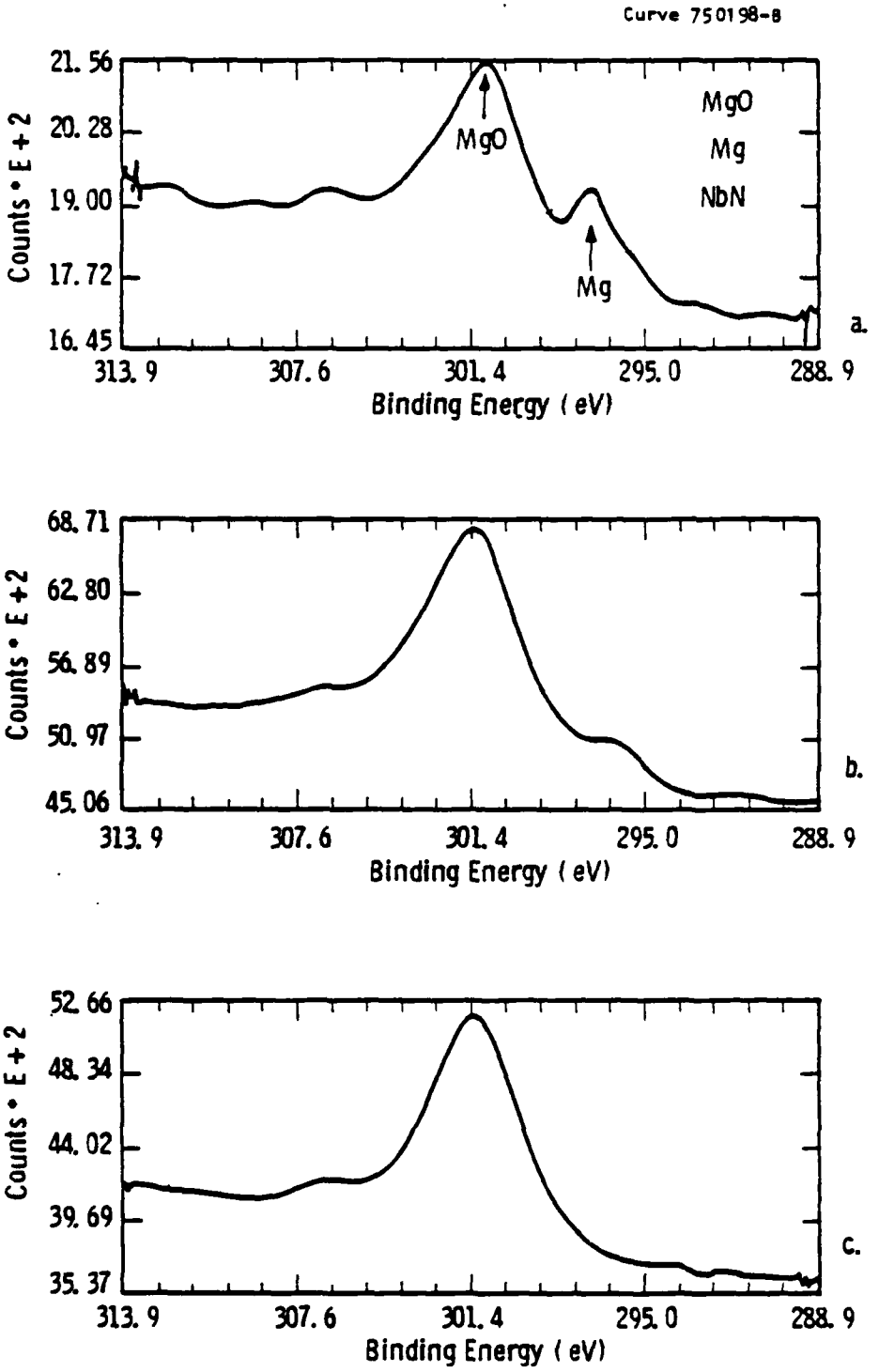

Fig. 7 XPS spectra of Mg/MgO (Auger KLL electrons) on NbN: (a) ion-beam oxidized Mg overlayer, (b) after an additional ion-beam treatment, (c) after heating to 300 C.

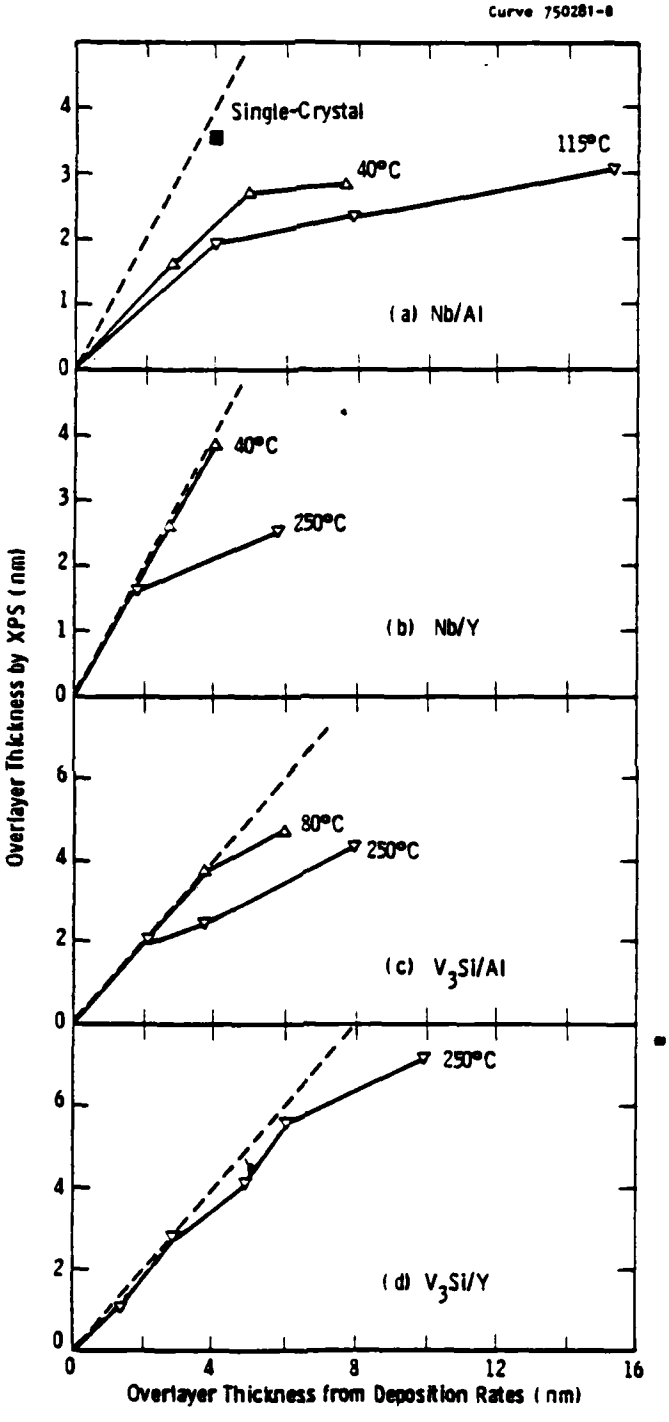

Fig. 8 Diffusion of metallic al and Y overlayer into Nb and V_3Si at various temperatures: in the absence of diffusion the overlayer thickness determined by XPS equals that inferred from deposition rate.

The self-limited oxide thickness is 6nm, lower oxides add another 2 nm. Underneath this crust oxygen dissolves in Nb over the range comparable to the Nb coherence length. The proximity layer thus formed under the Nb_2O_5 barrier degrades the energy gap and increases the subgap conductance. A comparative XPS study of thermal oxide formation on Nb and NbN between 20 and 200 C (44) has shown (Fig. 9) that in NbN the Nb_2O_5 thickness saturates at about 2 nm, and the lower oxide/suboxide underlayer at 1 nm, only 15 to 20% of ξ_s. The final product of NbN oxidation is also much less dependent upon the presence of surface impurities than are oxides on

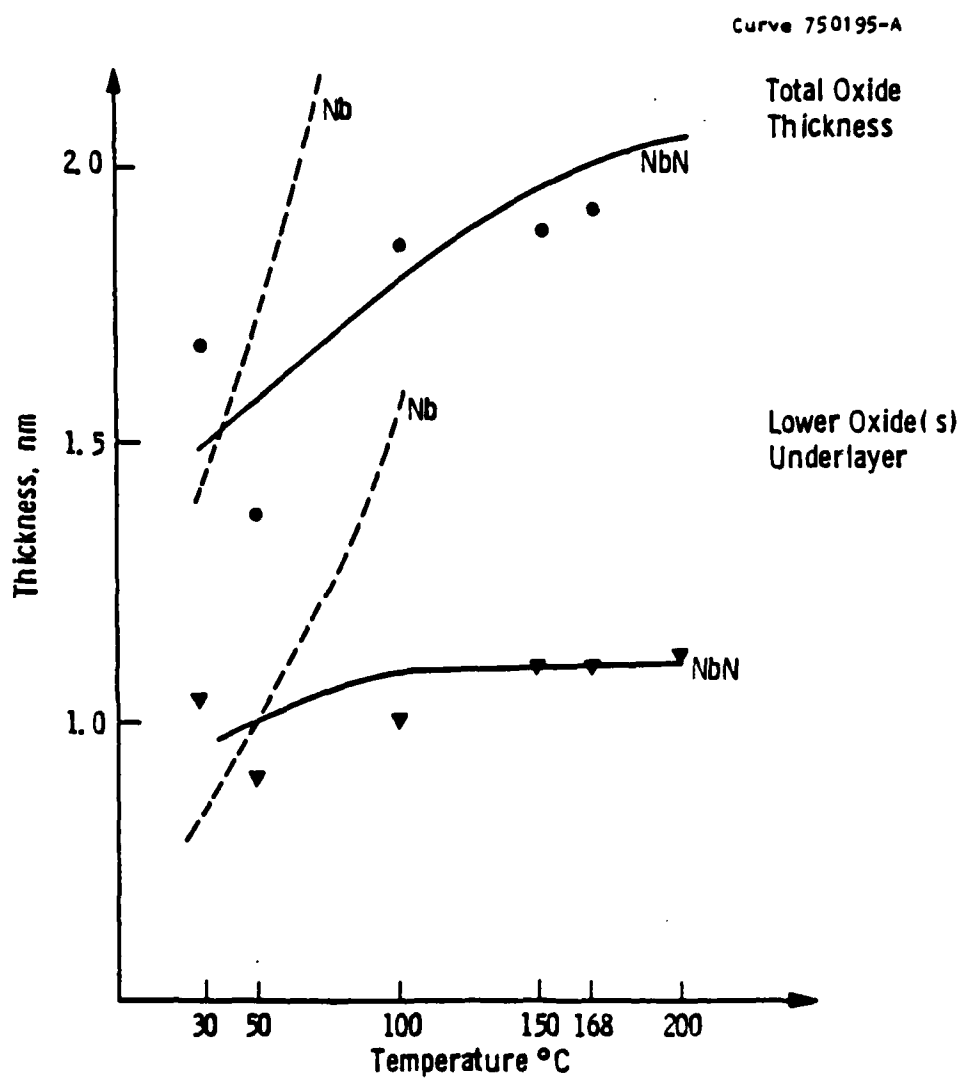

Fig. 9 Thermal oxide thickness on Nb and NbN (determined by XPS) vs temperature of formation [after Ermolieff et al (44)].

metallic Nb. Native oxide barriers on NbN are, therefore, easier to fabricate reproducibly than those on Nb. The degradation of NbN, due to the thin underlayer, is slight, although noticeable. Most recently, the phase composition of that underlayer was identified by Halbritter and Darlinski (45). Note that the high quality amorphous Nb_2O_5 barriers produced on Nb by the Greiner rf-plasma process (46), and largely free of the lower oxide/suboxide underlayer, were grown on a diffusion barrier of NbCO that was created first, due to the presence of C-impurities during plasma pre-cleaning (2). Similarly, the best native barriers on A15's were formed by Michikami et al using rf-plasma oxidation of a mixed fluoride surface layer created by reactive plasma cleaning with CF_4 that preceded the rf-plasma oxidation (29), and apparently prevented the A15 surface from segregating upon oxidation.

Thermal growth of oxides on metal overlayers of Al, Mg, Y etc. is self-limiting, in agreement with the Cabrera-Mott theory. The overlayers thus passivate upon reaching an equilibrium oxide thickness determined by the oxidation parameters, especially temperature and humidity. Table 3 shows examples of these passivation thicknesses and corresponding tunneling resistances for Al, Mg and Y that we oxidized in dry oxygen at room temperature.

Table 3. Saturated Surface-Oxide Growth

Material	Oxide Thickness (nm)	Junction Resistance (Ω-cm^2)
NbN	1.9	10^{-4} to 10^{-3}
Al	2.0	10^{-3} to 10^{-2}
Mg	3.2	10^{-1} to 10^{0}
Y	4.3	10^{2}

The tendency to form hydroxides upon oxidation in humid air is specific to metallic overlayers of metals such as Al, Mg, and especially Y or other rare earths. According to (47) the presence of hydroxide is necessary to plug pinholes in Y_2O_3 barriers. This point has not yet been confirmed by others. Moisture also increases the oxide growth rate and passivation thickness, making the process control difficult. For example, ambient humidity should not exceed 50 to 55% to form good junctions with air-oxidized Al barriers (27). These barriers appear to contain the Al-hydroxide. The effect of hydroxides on the barrier properties and interaction with the counterelectrode is not well known and understood. It deserves further investigation for the sake of ex-situ junction fabrication technologies, while it is of no consequence for the in-situ trilayer formation where the oxidation can be carried out in controlled, dry O_2 atmosphere.

Ruggiero et al reported recently a decrease in barrier height with increasing S that appears specific to thermally oxidized barriers, native and artificial (48). They explained this dependence in terms of metal oxidation theory (31). Since the mechanism of growth is changing with thickness from an initial, field-aided (nonlinear) ionic diffusion to the much slower, thermally activated (linear) process, the quantum-mechanical properties of the barrier change accordingly. For barriers of nonuniform thickness the $e\bar{\phi}$ vs S dependence will attenuate the dominance of the thinnest regions thus producing an averaging effect. Another consequence is a wide range of $e\bar{\phi}$ data for a given electrode/barrier/electrode sandwich, and the need to quote S as a reference parameter. No thickness dependence of $e\bar{\phi}$ is expected, however, in deposited-oxide barriers.

In the case of oxidized Al we recently observed a simultanous increase in $e\bar{\phi}$ and S of a thermally pre-oxidized barrier upon subjecting it to an additional ion-beam oxidation process (49). This suggests that ion-mobility enhancement by bombardment makes the oxide more uniform. Kinetic energies of a few hundred eV can, however, be high enough to facilitate interdiffusion and/or chemical reactions at the base/barrier

interface, especially in the thinnest barrier regions. An indication of an enhanced reaction between NbN and Mg to form Mg-nitride was inferred from the subgap conductance in NbN/Mg/MgO/Pb-Bi junctions. Ion-beam oxidation systematically resulted in a higher subgap conductance than that in junctions with thermal barriers while the zero-bias value was unchanged (49). No such effect was seen in NbN/Al/Al_2O_3/Pb-Bi junctions.

Barrier Crystallinity

Most literature data on low-leakage oxide and Schottky tunnel junction barriers identify these as amorphous, although supporting electron diffraction evidence is scarce. Amorphous thin layers are expected to form when the density of nucleation centers is high, and atomic surface mobility low during the deposition or oxidation. Amorphous or fine-crystalline base electrode/metallic overlayer, surface impurities, co-presence of two or more atomic species in that overlayer (50), and a low formation temperature, all promote amorphicity. A notable exception in the junction barrier literature is that of polycrystalline Ge on NbN that yielded very low subgap conductance (9). In an inelastic electron tunneling (IETS) study Liehr compared amorphous and microcrystalline oxidized Al-barriers (51). The oxide formed as amorphous or crystalline, depending upon the Al-crystallite size. The IETS spectra were obtained using the Pb counterelectrode. Crystalline barriers exhibited a significantly reduced Pb work-function (barrier height), higher leakage and noise. Liehr ascribed these to a higher ionic mobility, possible localized states at the Fermi surface, and stoichiometry defects (free Al-atoms). Halbritter analyzed Liehr's data in terms of localized states at the Al-oxide/Pb interface causing resonant tunneling (52). This analysis suggests that all crystalline oxide barriers might have undesirable electronic properties. On the other hand, we have been fabricating low-leakage-current (Q up to 100) junctions such as Nb_3Sn/Al/oxide/Pb-Bi, NbN/Al/oxide/Pb-Bi, and NbN/Mg/oxide/Pb-Bi with polycrystalline, often highly textured oxides (24,49), characterized by in-situ RHEED. High leakage, when observed, was usually traceable to the overlayer thickness

nonuniformity rather than crystallinity. The presence of grain boundaries in polycrystalline oxides could however facilitate ionic diffusion of the refractory counterelectrode metal through the barrier, and thus the formation of shorts, as discussed in the next section. The problem of barrier crystallinity clearly deserves further studies. The technological rationale for crystalline barriers will be given below.

The barrier/counterelectrode interface

The literature of all-refractory junctions includes several reports on shorts created when depositing a niobium counterelectrode on the native Nb-oxide barrier. The practical solution found was to deposit a very thin, probably discontinuous layer of a less reactive metal, Cu (53) or Au (2,54) separating the oxide from Nb. No need for an analogous approach has been reported for Nb_2O_5/NbN, a-Si/Nb, a-Si/-NbN, and Al_2O_3/Nb. It is generally recognized, however, that low-leakage junctions with a refractory base and soft (Pb) alloy counterelectrode are much easier to fabricate than those with refractory counterelectrodes, and that the difficulties can be traced to interactions occuring at the barrier/counterelectrode interface. The mechanisms of these interactions are still rather obscure. Nevertheless, some evidence exists of surface chemical reactions, diffusion through the barrier, and damage due to energetic particles. The IETS represents here a particularly useful diagnostic tool. A clear signature of reaction between adsorbate $Al_2O_3.H_2O$ or $Al(OH)_3$ barrier surface and Cu (counterelectrode) that is unfeasible thermodynamically in the bulk was obtained in IETS vibrational spectra where peaks characteristic of $Cu(OH)_2$ were identified, as shown in Fig. 10 (55). The $Cu(OH)_3$ heat of formation is -450 KJ/mole, compared with -1980 and -1276 KJ/mole for the hydrated oxide and hydroxide, respectively. For the Pb-counterelectrode the hydroxide peaks are barely discernible in Fig. 10. Niobium is much more electropositive than Cu so that an analogous reaction with an oxide/hydroxide barrier surface is even more likely. In fact, the formation of a Cu/Nb or Au/Nb couple representing a high electrochemical potential barrier was proposed as

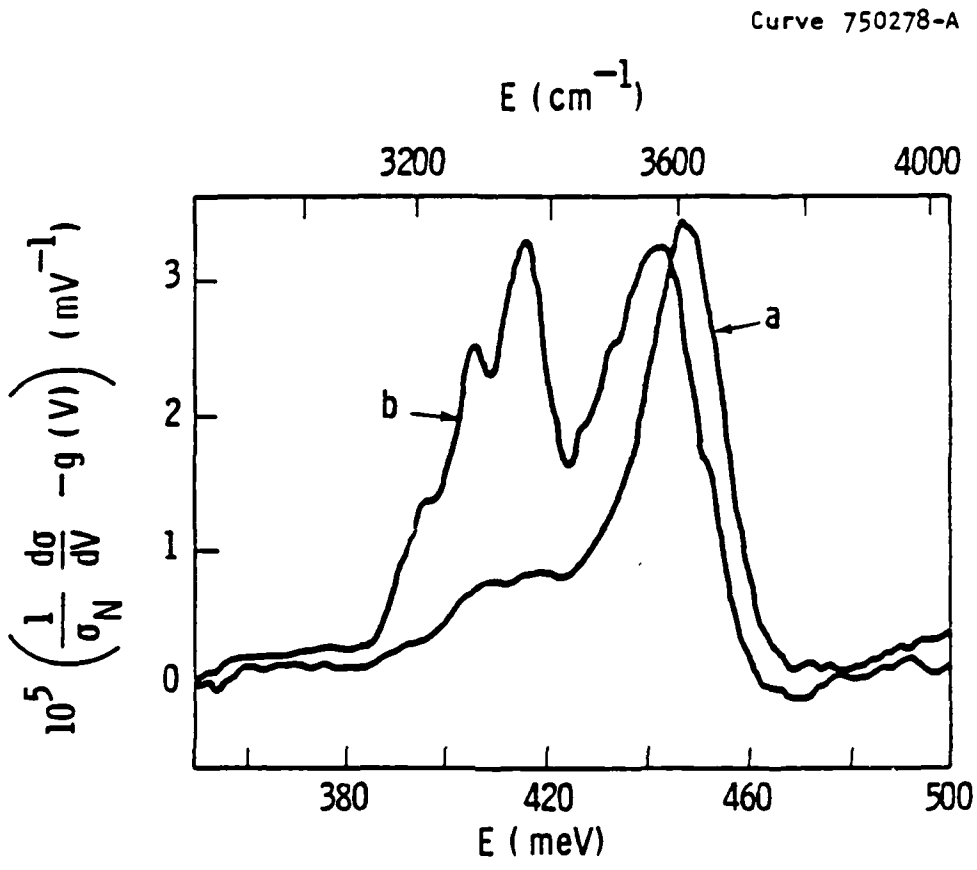

Fig. 10 Inelastic electron tunneling spectra of: (a) $Al/Al_2O_3/Pb$, and (b) $Al/Al_2O_3/Cu$. Vibrational mode peaks in the normalized conductance derivative between 400 and 420 meV are characteristic of $Cu(OH)_3$; smooth polynomial background g(V) is subtracted [after Konkin and Adler (55)].

an explanation of Cu or Au "patchy" layer effectiveness in preventing shorts in Nb-counterelectrode junctions (54). A Nb-compound counterlectrode should be less reactive than Nb itself. We verified this in our experiments with $NbN/Al_2O_3/NbN$ junctions by replacing NbN-counterelectrode with Nb. On identical ion-beam-oxidized barriers low-leakage junctions were obtained with NbN while Nb resulted in shorts. Niobium stripped to Nb^{+5} by the barrier surface adsorbate (oxygen) may also readily diffuse through the barrier. The IETS vibrational mode peak intensity is proportional to the barrier volume so that it provides a very direct measure of its effective thickness. Spectra of Al/Ethylene/M junctions, where M is a metal, indicated that the intensity of the

characteristic 360 meV peak is proportional to the ionic radius of M, as shown in Fig. 11 (56). The counterelectrode-diffusion into the barrier was thus demonstrated convincingly. The Nb^{+5} radius is 0.069 nm, and by extrapolating the plot of Fig. 11 to this value one expects an effective ethylene barrier under Nb that is an order of magnitude thinner than that under the Pb-electrode, a dramatic difference.

Curve 750280-A

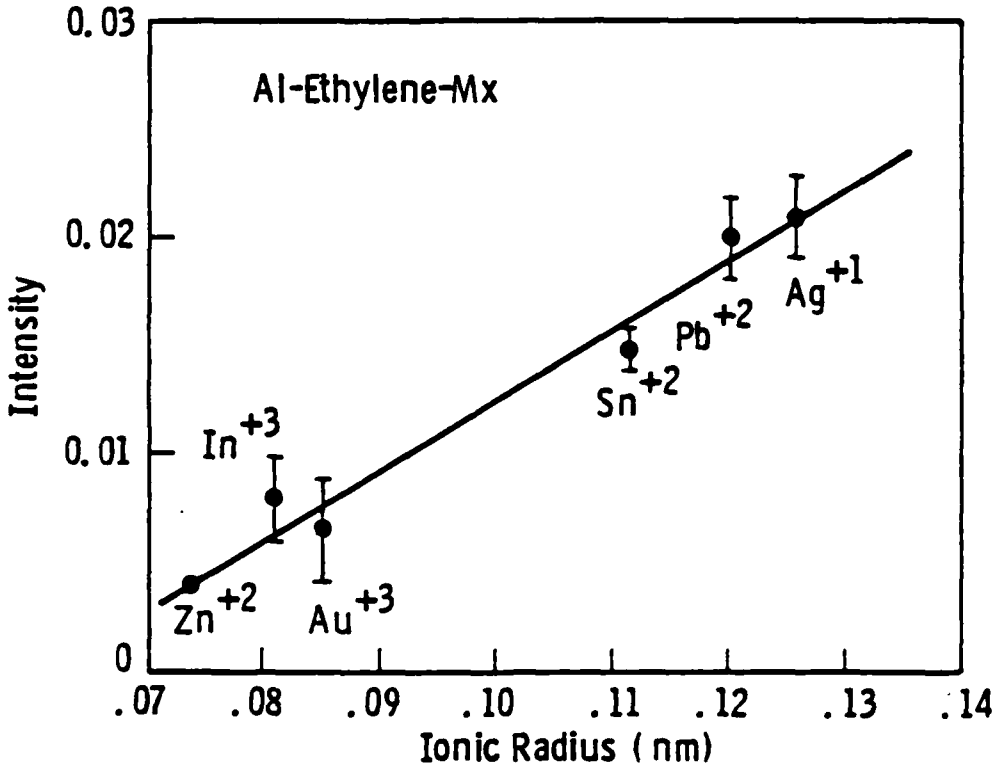

Fig. 11 The intensity of IETS vibrational mode ethylene peaks vs the ionic radius of the counterelectrode metal M [after Magno et al (56)].

Thermally activated diffusion through the barrier is enhanced if grain boundaries are present. In Liehr's experiments quoted above, the in-situ fabricated and tested $Al/Al_2O_3/Pb$ junctions with crystalline barriers invariably shorted upon thermal cycling to only 50 K, while those with a-Al_2O_3 could be cycled up to 500 K (51). To minimize the interdiffusion and occurence of shorts in thin barriers, two extremes are, therefore, recommended: either an amorphous or a single--

crystal barrier.

The kinetic energy of the deposited counterelectrode atomic or ionic species will assist the interdiffusion and mixing with the barrier. In thermalized magnetron sputter-deposition, at practical target-to-substrate distances, the energy distribution cutoff is typically of the order of a few eV (57). The presence of a low fraction of more energetic particles cannot, however, be excluded. From this point of view, evaporation of refractory counterelectrodes is preferable since the kinetic energies involved are well below 1 eV. For NbN, however, reactive sputter-deposition is almost universally employed. A magnetron gun system, either dc or rf, should be used in this case as it minimizes the bombardment of the substrate by energetic particles.

The effects reviewed above can "consume" the upper part of the barrier. The thinnest regions are at risk to be consumed entirely, thus resulting in shorts.

Counterelectrode Gap Degradation

Counterelectrode energy gap values approaching those of bulk superconductors have not been attained, except in the most recent work by Shoji et al (10), and yet unpublished study by Yamashita (58). These exceptions will be discussed later.

Interactions at the barrier/counterelectrode interface, that have been discussed above, can degrade the counterelectrode energy gap over a depth scale comparable to that of barrier degradation. In B1 and A15 compounds that depth may represent a fraction of the coherence length. Consequently, the gap voltage may be reduced, the subgap conductance increased, and proximity effect features in the I-V characteristic accentuated. Systematic studies of the counterelectrode degradation problem have not been published to date. We believe, however, that the dominant effect is that of crystalline structure and morphology of the counterelectrode near the interface, rather than electrochemistry. This belief is based on the T_c dependences upon the film thickness. Measurements by many authors, and our own data for Nb_3Ge films on sapphire substrates, show that in A15 films the bulk T_c value is attained only at thicknesses exceeding the coher-

ence lengths (Table 1) by an order of magnitude or more. For Nb and NbN the bulk T_c is practically attained within 2 to 4 coherence lengths, depending upon the substrate (59). This is illustrated in Fig. 12 where T_c/T_c bulk is plotte vs. the normalized thickness of polycrystalline film, x/ξ_s. The T_c decrease at $x < \xi_s$ is theoretically expected (60) and of no consequence here. The plots are, in fact, limited to $x/\xi_s > 1$. The different behavior of A15's, exemplified by

Curve 750279-A

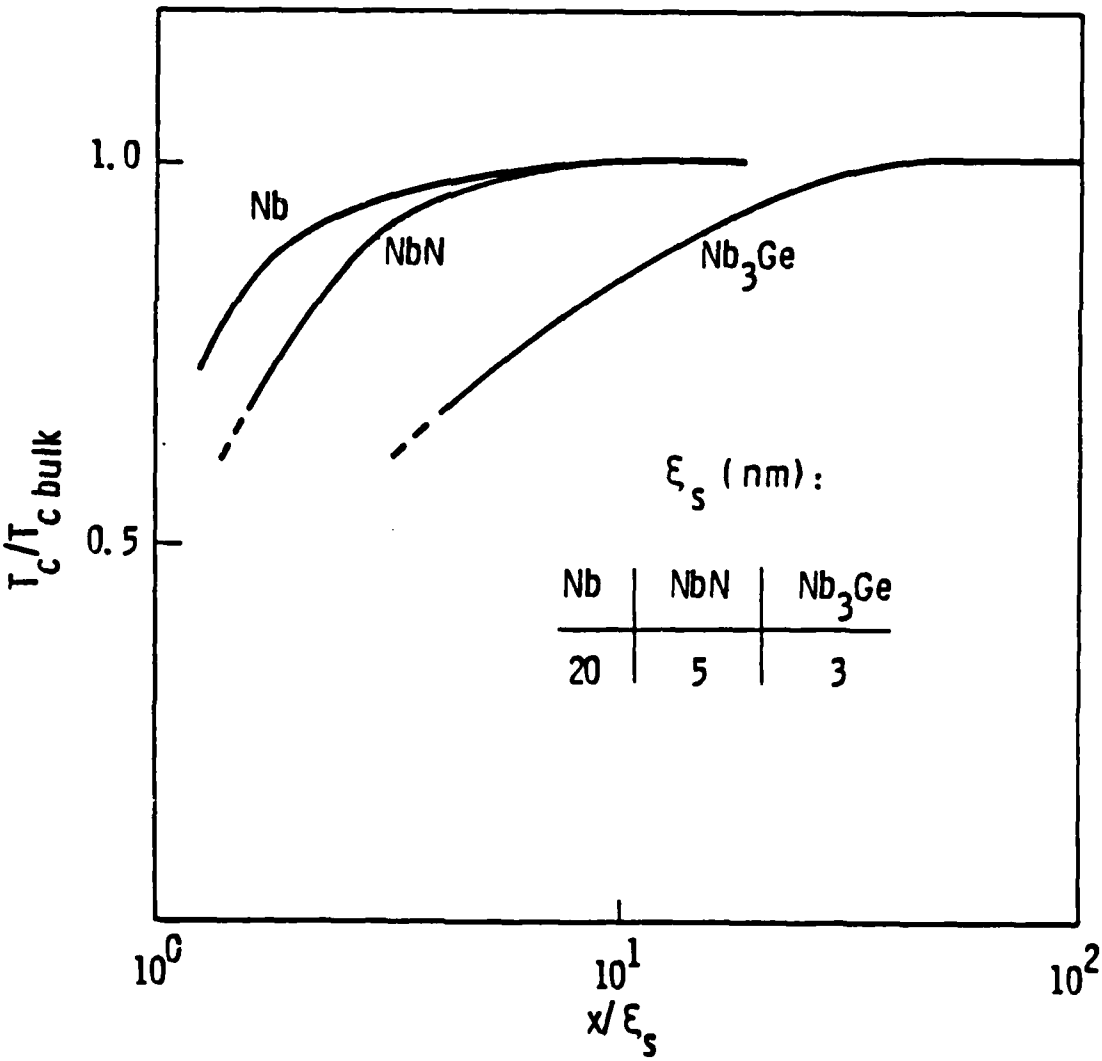

Fig. 12 Normalized critical temperature vs normalized film thickness [Nb on Si data after Kodama et al (59), NbN on Si and Nb_3Ge on sapphire- our data].

Nb_3Ge, can only be explained by their T_c's susceptibility to crystalline disorder. It is well known, for example, that upon disordering by fast-neutron irradiation all high-T_c A15's degrade dramatically at doses that hardly alter the T_c of NbN or Nb (61,62). That the T_c degradation in thin films is due to disorder is proven by the fact that epitaxial deposition of very thin films, $x \rightarrow \xi_s$, results in T_c's approaching the bulk value. This was shown for Nb_3Ge and also for Nb (63,59). Epitaxy, if feasible, thus offers a radical solution to the counterelectrode gap degradation. Experience shows that both single-crystal and polycrystalline epitaxy can be effective.

In non-epitaxial films, additional degradation may also be due to the film morphology. High number density of 3 nm voids (low density regions) is a standard feature of very thin films when the nucleation density is high and the adatom surface mobility low (64). The voids are separating 1-3 nm clusters of dense deposit. At low deposition temperatures this microstructure will persist near the substrate /film interface even if the film grows thicker. The energy gap of an aggregate of clusters smaller than ξ_s, and weakly connected, is lower than that of a bulk superconductor. This problem is not likely to occur in epitaxial, especially single-crystalline counterelectrodes, where the described morphological features are absent.

The high gap voltages of Yamashita's NbN counterelectodes are explained by epitaxy on textured MgO barriers (58). Shoji *et al* obtained slightly lower gap voltages, up to 2.4-2.5 mV, when depositing NbN counterelectrodes on amorphous MgO barriers (10). We believe that short-range order in MgO, undetected by reflection high energy electron diffraction (RHEED), was sufficient in this case to induce polycrystalline, ordered (*i.e.* epitaxial) growth of NbN. In our opinion, epitaxial layered film structures represent the most promising approach to high-gap counterelectrode fabrication, and thus to a technology of tunnel junctions capable of operating at temperatures up to $T_{op} = 10$ K with NbN electrodes, and even higher with A15 *e.g.* Nb_3Ge electrodes. It is not clear yet, whether polycrystalline epitaxy will be sufficient, or

single-crystal layered structures required. In either case, this approach provides a rationale for investigating the properties of crystalline barriers.

Epitaxial Growth of Electrodes and Barriers

We are conducting a systematic study of epitaxial growth of junction electrodes and barriers, with the goal to develop a technology of epitaxial B1 and A15 tunnel junctions. Use is made of an ultra-high-vacuum (UHV) deposition and surface analysis system designed especially for this purpose, and analogous to molecular-beam-epitaxy (MBE) systems (65). In addition to standard effusion cells, it is equipped with four electron gun sources (nine hearths), and four magnetron-sputter-guns in a separate chamber. The UHV environment of < 10^{-8} Pa permits evaporation/co-evaporation of refractory metals and compounds at low rates, < 0.1 to 1 nm/min, that facilitate epitaxy, without incorporating many impurities. The near-surface structure of a deposited films can be analysed by RHEED, and low energy electron diffraction (LEED) prior to depositing a subsequent layer, and without breaking the vacuum. The near-surface film phases, composition, impurities, and overlayer thicknesses can be determined by XPS and, to lesser extent, Auger electron spectroscopy (AES).

We found that in the UHV environment many metals and compounds of interest tend to grow epitaxially, even on substrates of different structure that offer an only very approximate match of atomic positions and spacings (66). This can be explained by a low nucleation rate, and high adatom surface mobility on clean single crystal substrate surfaces. Our present results can be summarized as follows:

1. Epitaxial growth of NbN occurs on MgO single crystal (111) and (100) surfaces, on polycrystalline MgO and on sapphire of several orientations (67,68). Epitaxy helps stabilize the B1 phase closer to stoichiometry, so that the T_c of NbN (and its energy gap near the substrate) is higher than on non-epitaxial substrates. In a given set of experimental conditions, and with a deposition temperature of 300 C, the 50 nm thick (111) NbN films on (111) MgO exhibited a

T_c of 16.3 K, approximately 15 K on polycrystalline MgO, and only 13 K on $(11\bar{2}0)$ sapphire. Homoepitaxial growth on polycrystalline, textured NbN resulted in a T_c of 16.5 K in 50 nm films grown at a temperature of only 90 C. This shows the importance of a close lattice parameter match that eliminates the T_c-reducing strains and dislocations present in mismatched films.

2. Epitaxial growth of A15 Nb_3Sn and Nb_3Ge occurs on (1120) and (0001) sapphire surfaces. An example is shown in Fig. 13, where RHEED patterns of (100) Nb_3Sn show order after only 6 nm of growth i.e. within approximately two coherence lengths from the interface with $(11\bar{2}0)$ sapphire. The quality of the single crystal, 200 nm thick film is shown by the narrow X-ray rocking curve width of 0.4 degrees. Single crystal (111) and (100) Nb_3Ge films were grown on (111) and (100) stoichiometric Nb_3Ir with a perfect lattice parameter match.

3. A five-layer all-epitaxial structure was fabricated that exhibited tunneling characteristics. Starting with $(11\bar{2}0)$ sapphire, and (110)Nb base electrode, a $Nb/Al/Al_2O_3/Al/Nb$ sandwich was deposited with the structure of every layer determined by in-situ RHEED. The oxide was formed by oxidiz-

a b

Fig. 13 RHEED patterns of (100)Nb_3Sn on $(11\bar{2}0)$ sapphire: (a) 6 nm thick, (b) 200 nm thick.

ing the first, 3 nm thick Al-overlayer. A diffraction pattern similar to that of Al indicated that the oxide was very thin. The Nb-counterelectrode retained the (110) orientation of the base. The epitaxial barrier was extremely leaky, however, so that a high sum-gap voltage of approximately 3 mV could only be guessed.

In view of our results, the need to investigate epitaxial and single-crystal barriers is understandable. Already at this stage, the feasibility of high-T_c epitaxial B1 and A15 electrodes appears assured. Finding barriers that would exhibit a sufficient crystalline match, and the required tunneling characteristics represents a problem. So far, the only plausible candidate is MgO for NbN junctions, although the lattice parameter mismatch is 4% in this case. No such candidate material has yet been found for A15 junctions.

Fabrication and Material Alternatives

The selective review of material problems specific to high-T_c refractory electrodes leads us to a discussion of fabrication and material alternatives that we consider crucial.

The first alternative is that of low vs. high processing temperature, T_p, to be used in the whole fabrication sequence. A low T_p, close to ambient, offers the advantage of a relatively easy control of the previously discussed,adverse physico- and electrochemical effects that are particularly troublesome with thin metal oxide barriers. In this respect, especially important is the possibility of forming amorphous or microcrystalline barriers that are sufficiently uniform. An additional advantage resides in the flexibility of patterning. For example, lift-off photoresist can be used to pattern the counterelectrode in ex-situ fabrication sequences. The disadvantage of low T_p is the impossibility to attain the highest $T_c, \Delta, \xi_s/\lambda$ and also T_{op} via epitaxy. To date, the low-T_p alternative has been chosen by virtually all workers in the field, although Kroger et al

indicated the feasibility of high T_F for NbN/Ge/Nb junctions (9). Niobium nitride, and specifically the NbN/MgO/NbN configuration are particularly attractive for low temperature fabrication, as they permit one to exploit epitaxy, at least to some extent.

The use of high-T_F's appears inescapable if one wants to fabricate high-T_c A15 counterelectrodes or attain the best superconducting parameters of NbN. It is doubtful whether oxide barriers could be employed in this case. Elemental or other, especially molecular compound barriers, however, could be considered.

A related alternative is, therefore, that of thin, large-barrier-height oxides vs composite, low $e\bar{\phi}$ barriers, and tailored barriers discussed at this Conference (69). Historically, oxide barriers were used, as thermal, native oxide barriers formed spontaneously on many base electrodes, and the Greiner plasma process provided later a high degree of control of properties, i.e. narrow tolerances of I_c. With the advent of artificial barriers, however, different approaches to control of properties should be considered. The advantage of thin, artificial oxide barriers is chiefly the very low subgap conductance, demonstrated in several material systems. The disadvantage resides in the difficulty of controlling I_c and R_n to narrow tolerances, unless a Greiner-type process is used (either plasma or ion-beam oxidation). In this case, a relatively thick metal underlayer must be included in the design, not only to protect the base but also to allow a safety margin for the oxidation process. This is undesirable, as the junction $I_c.R_n$ product initially decreases exponentially with the increasing proximity layer thickness (70). Also, a metallic underlayer, and the plasma process itself, do not promote epitaxy of the counterelectrode.

Thus far, the most successful example of a practical, low-$e\bar{\phi}$ barrier is that of composite SiO_x/ a-Si:H/SiO_x, and Ge/SiO_x investigated by the former Sperry group (8,9,19). The role of a few monolayers of oxide is limited here to plugging the pinholes in the amorphous or crystalline, low resistance layer that can thus be made relatively thick (Table 2), with

its I_c and R_n easier to control. An intriguing property reported on the amorphous Zr-fluoride on Nb base is that, in spite of a relatively high $e\bar{\phi} = 0.5$ eV, it exhibited a very long wave-function decay length (6.5 nm vs. typically 0.2 nm in oxides) (12). Consequently, the R_n increase with thickness was very gradual, and the fabrication of thicker barriers possible. It is probable that this barrier was in reality a NbF_x/ZrF_4 composite, where the ultrathin Nb-fluoride, formed in the CF_4 cleaning process, plugged pinholes in ZrF_4. We have observed an analogous situation with the Nb_2O_5/CaF_2 barrier on NbN. In this case the thin native oxide effectively plugged pinholes in CaF_2 (66). Examples, discussed earlier, of using carbide or fluoride protective layers (2,29) amounted to composite barriers with a native oxide as the main material. Once a protective layer is in place, however, a degree of freedom is obtained in the selection of barrier materials with a variety of desired electrical and electrochemical properties, and without worries about the nonuniformity of coverage. So far, this freedom has been exercised only very timidly. We believe that an alternative route superior to the thorny path towards thin, uniform, single-material thin barriers resides in composite, multilayered, mostly non-oxide barriers that do not have to be very thin, and in which each layer is consciously assigned a separate role. Protecting electrodes and the barrier against adverse electrochemical effects can be separated from tailoring the electrical (also novel) characteristics within required tolerances.

It is conceivable, that even the role of epitaxially seeding a polycrystalline, high-T_c-counterelectrode could be assigned to a separate, very thin layer. Only the single-crystal epitaxy approach appears incompatible with the composite barrier concept. Too little is known to decide that it will be impossible.

The choice of best electrode material, B1 (NbN) vs. A15, is only a function of the feasibility of alternatives discussed above. High T_F, interface protection, and polycrystalline epitaxy may make the use of A15 counterelectrodes possible and advantageous in the future.

We hope that through this discussion of technological alternatives we have indicated promising directions for research that may result in high-T_{op} tunnel junctions, and can also contribute to the quest for three-terminal, superconducting devices.

Conclusions

1. Today, the best potential technology is that of all-niobium nitride tunnel junctions with amorphous or microcrystalline barriers, processed at low temperatures and possibly exploiting polycrystalline epitaxy.
2. Longer range barrier research should concentrate on composite, mostly non-oxide barriers that will be electrochemically compatible with electrodes, and will permit flexibility in tailoring of junction characteristics.
3. Longer range electrode material research should concentrate on A15 compounds, especially Nb_3Sn, Nb_3Al and Nb_3Ge, and their growth by polycrystalline and single-crystal epitaxy on non-A15 substrates which could be suitable for barrier use. Single-crystal B1 electrodes also deserve attention.
4. Main problem areas for research are: barrier physics, and pnysics and electrochemistry of surfaces and interfaces.

References

1. Beasley, M. R. and C. J. Kircher. 1981. In: Superconductor Materials Science (S. Foner and B. B. Schwartz, eds.). Plenum Press, p. 605.

2. Raider, S. I.. 1985. IEEE Trans. on Magnetics MAG-21, 110.

3. Orlando, T. P., E. J. McNiff, S. Foner and M. R. Beasley. 1979. Phys. Rev. B 19, 4545.

4. Simmons, J. G.. 1963. J. Appl. Phys. 34, 1793.

5. Halbritter, J.. 1982. Surf. Sci 122, 80. Also: 1985. IEEE Trans. on Magnetics MAG-21, 858, and this Conference.

6. Bending, S. J. and M. R. Beasley. 1985. Phys. Rev. Lett. 55, 324.

7. Rogers, C. T. and R. A. Buhrman. 1984. Proc LT-17 (U. Eckern, W. Weber and H. Wuehl, eds.) North-Holland, p. EP14.

8. Smith, L. N., J. B. Thaxter, D. W. Jillie and H. Kroger. 1982. IEEE Trans. on Magnetics, MAG-18, 1571. Also: H. Kroger, L. N. Smith, D. W. Jillie and J. B. Thaxter. 1983. Ibid. MAG-19, 783.

9. Kroger, H., D. W. Jillie, L. N. Smith, L. E. Phaneuf, C. N. Potter, D. M. Shaw, E. J. Cukauskas and M. Nisenoff. 1984. Appl. Phys. Lett. 44, 562.

10. Shoji, A., M. Aoyagi, S. Kosaka, F. Shinoki and H. Hayakawa. 1985. Appl. Phys. Lett. 46, 1098. Also: this Conference.

11. Gavaler, J. R.. 1985. (Westinghouse R&D Center). Unpublished results.

12. Asano, H., K. Tanabe, O. Michikami, M. Igarashi and M. R. Beasley. 1985. Jap. J. Appl. Phys. 24, 289.

13. Moore, D. F.. 1978. Dissertation, Stanford Univ. Also: D. A. Rudman and M. R. Beasley. 1981. Appl. Phys. Lett. 36, 1010.

14. Rowell, J. M., M. Gurvitch and J. Geerk. 1981. Phys. Rev. B, 24, 2278.

15. Gurvitch, M., M. A. Washington, H. A. Huggins and J. M. Rowell. 1983. IEEE Trans. on Magnetics MAG-19, 791.

16. Based on the dielectric constant of bulk MgO and the measured thickness.

17. Shoji, A., S. Kosaka, F. Shinoki, M. Aoyagi and H. Hayakawa. 1983. IEEE Trans. on Magnetics MAG-19, 827.

18. Shinoki, F., A. Shoji, S. Kosaka, S. Takada and H. Hayakawa. 1981. Appl. Phys. Lett. 38, 285.

19. Jillie, D. W., H. Kroger, L. N. Smith, E, J, Cukauskas and M. Nisenoff. 1982. Appl. Phys. Lett. 40, 747.

20. Rudman, D. A.. 1982. Dissertation, Stanford Univ. G. L. Rept. No. 3509, p. 72. Also: 1984. D. A. Rudman, F. Hellman, R. H. Hammond and M. R. Beasley, J. Appl. Phys. 55, 3544.

21. Hammond, R. H.. 1978. J. Vacuum Sci. Tech. 15, 382.

22. Hellman, F. A., A. F. Marshall and T. F. Geballe. 1985. Bull. Am. Phys. Soc. 30, 607.

23. Greggi, J. and J. R. Gavaler. Ibid., 608.

24. Talvacchio, J., A. I. Braginski and M. A. Janocko. 1985. IEEE Trans. on Magnetics MAG-21, 521.

25. Kihlstrom, K. E.. 1982. Dissertation, Stanford Univ., G. L. Rept. No. 3467. Also: Kihlstrom, K. E., R. H. Hammond, J. Talvacchio and T. H. Geballe. 1982. - J. Appl. Phys. 53, 8907.

26. Igarashi, M., M. Hikita and K. Takei. 1984. In: Adv. - Cryo. Eng. (A. F. Clark and R. P. Reed, eds.) 30, p. 535.

27. Gurvitch, M. and J. Kwo. Ibid. p. 509.

28. Arnold, G. B.. 1978. Phys. Rev. B18, 1076: E. L. Wolf and G. B. Arnold. 1982. *Phys. Repts.* 91, 31.

29. Michikami, O., K. Tanabe, Y. Kato and H. Takenaka. - 1985. IEEE Trans. on Magnetics MAG-21, 528.

30. Ihara, H., Y. Kimura, H. Okumura, K. Senzaki and S. Gonda. 1984. In: Adv. Cryo. Eng. (A. F. Clark and R. P. Reed eds.) 30, p. 589.

31. Fromhold, A. T., jr. 1976. Theory of Metal Oxidation, Vol. 1. North-Holland Publ. Co., N.Y.

32. Gavaler, J. R., M. A. Janocko and C. K. Jones. 1974. In: Low Temperature Physics - LT13 (K. D. Timmerhaus, W. J. Sullivan and E. F. Hammel, eds.), Plenum Co., 3, p. 559.

33. Talvacchio, J., M. A. Janocko and A. I. Braginski. 1985. Bull. Am. Phys. Soc. 30, 280.

34. Miedema, A. R. and F. J. A. den Broeder. 1979. Z. Metallkunde, 70, 14.

35. Kwo, J., G. K. Wertheim, M. Gurvitch and D. N. E. Buchanan. 1982. Appl. Phys. Lett. 40, 675.

36. Kwo, J., G. K. Wertheim, M. Gurvitch and D. N. E. Buchanan. 1983. IEEE Trans. on Magnetics, MAG-19, 795.

37. Umbach, C. P., A. M. Goldman and L. E. Toth. 1982. Appl. Phys. Lett. 40, 81.

38. Grundner, M. 1977. Proc 3rd Int. Conf. Solid Surf. (Dobrozemsky et al. eds.) Vol. 2, p. 2237. Also: 1977. Nuclear Center Karlsruhe (KfK) Rept. 2565.

39. Graybeal, J. M. and M. R. Beasley. 1984. Phys. Rev. B 29, 4167.

40. Shunk, F. A. 1969. Constitution of Binary Alloys, Second Supplement, McGraw-Hill Book Co., p. 189.

41. Van Vechten, D. and J. F. Liebman. 1985. J. Vac. Sci. Tech. A 3, 1881.

42. Grundner, M. and J. Halbritter. 1984. Surf. Sci. 136, 144, and references therein.

43. Sanz, J. M. and S. Hofmann. 1983. J. Less Common Met. 92, 317.

44. Ermolieff, A., M. Girard, C. Raoul, C. Bertrand and T. Minh Duc. 1984. Presented at the 6th Symp. on Appl. Surface Analysis, Dayton, Ohio (unpublished).

45. Halbritter, J. 1985. Unpublished research report (Nuclear Center Karlsruhe).

46. Greiner, J. H. 1971. J. Appl. Phys. 42, 5151.

47. Ronay, M. and E. E. Latta. 1983. Phys. Rev. B 27, 1605.

48. Ruggiero, S. T., G. B. Arnold, E. Track and D. E. Prober. 1984. IEEE Trans. on Magnetics MAG-21, 850.

49. Talvacchio, J, J. R. Gavaler, A. I. Braginski and M. A. Janocko. 1985. Submitted to J. Appl. Phys.

50. Schneider, U., J. Geerk and H. Rietchel. 1984. Proceedings of LT-17 (U. Eckern, A. Schmid, W. Weber and H. Wuhl, eds.), North-Holland, p. 489.

51. Liehr, M. 1982. Dissertation, Aachen Univ., (unpublished). Also: M. Liehr and S. Ewert. 1982. Z. Phys. B - Condensed Matter 52, 95.

52. Halbritter, J. 1984. Private communication.

53. Hawkins, G. and J. Clarke. 1976. J. Appl. Phys. 47, 1616.

54. Bain, R. J. P. and G. B. Donaldson. 1985. Trans. IEEE on Magnetics MAG-21, 543.

55. Konkin, M. K. and J. G. Adler. 1983. J. Phys. Chem. 87, 2477.

56. Magno, R., M. K. Konkin and J. G. Adler. 1977. Surf. Science 69, 437.

57. Meyer, K., I. K. Schuller and C. M. Falco. 1981. J. Appl. Phys. 52, 5803.

58. Yamashita, T. 1985. To be published in Adv. Cryo. Eng. (Proceedings of the 1985 CEC-ICMC, Boston, August 1985).

59. Kodama, J., M. Itoh and H. Hirai. 1983. J. Appl. Phys. 54, 4050.

60. Cooper, L. N. 1961. Phys. Rev. Lett. 6, 689.

61. Sweedler, A. R., C. L. Snead and D. E. Cox. 1979. In: Treatise on Materials Science and Technology, 14,(T. Luhman and D. Dew-Hughes, eds.). Academic Press, p. 349.

62. Dew-Hughes, D. and R. Jones. 1980. Appl. Phys. Lett. 36, 856.

63. Gavaler, J. R., A. I. Braginski, M. Ashkin and A. T. Santhanam. 1980. In: Superconductivity in d- and f-band Metals (H. Suhl and M. B. Maple, eds.) Academic Press, p. 25.

64. Messier, R., A. P. Giri and R. A. Roy. 1984. J. Vac. Sci. Technol. A2, 500.

65. Talvacchio, J., M. A. Janocko, J. R. Gavaler and A. I. Braginski. 1985. Submitted to Adv. Cryo. Eng. 32,

66. Gavaler, J. R., A. I. Braginski, M. A. Janocko and J. Talvacchio. 1985. In: Materials and Mechanisms of Superconductivity (E. Wolf, ed.). In press.

67. Gavaler, J. R., J. Talvacchio and A. I. Braginski. 1985. Submitted to Adv. Cryo. Eng. 32,67.

68. Gavaler, J. R., J. Greggi and J. Schreurs. 1984. In: Proceedings of LT-17(U. Eckern, A. Schmid, W. Weber and H. Wuhl, eds), p. 115.

69. Klapwijk, T. M., this Conference.

70. Gallagher, W. J.. 1981. Physica 108B, 825.

APPENDIX D

Artificial oxide barriers for NbN tunnel junctions[a)]

J. Talvacchio, J. R. Gavaler, A. I. Braginski, and
M. A. Janocko

Westinghouse R & D Center, Pittsburgh, Pennsylvania 15235
(Received

Superconducting tunnel junctions have been prepared with NbN base electrodes, oxidized Al or Mg tunnel barriers, and NbN or Pb counterelectrodes. The tunnel barriers were formed either by thermal oxidation at room temperature or by subjecting the thin overlayers of Al or Mg to a low-energy ion beam in an argon-5% oxygen background. High-quality junctions with Pb counterelectrodes were produced by either method. However, for junctions with NbN counterelectrodes deposited at room temperature, the thermal oxidation resulted in shorts and the ion-beam oxidation resulted in low-leakage junctions. XPS measurements of the NbN/artificial-oxide bilayers showed that the ion-beam treatment increased the aluminum oxide thickness by the minimum detectable increment, approximately 0.2 nm, and increased the MgO thickness by 1 nm. The superconducting energy gap inferred for NbN counterelectrodes was typically half as large as the gap of the NbN base. Limitations on the values of NbN counterelectrodes grown on these barriers were established by measuring the energy gap of films as thin as 7.5 nm.

INTRODUCTION

Interest in superconducting tunnel junctions with NbN electrodes stems from the desirability of operating circuits based on Josephson junctions at a temperature greater than 10K. Shoji et al. have reported that Josephson currents in NbN / rf-sputtered MgO / NbN junctions were greater than zero at temperatures up to 15K.[1] A comparison will be made in this paper between two additional methods of forming Al_2O_3 and MgO barriers for NbN junctions: thermal oxidation and ion-beam oxidation of thin overlayers of Al and Mg.

The oxidized Al and Mg tunnel barriers have potential benefits as substrates for growth of the counterelectrode when compared with the native oxide and amorphous silicon barriers which have also been used successfully in junctions measured at 4.2K.[2-6] One advantage is that both Al_2O_3 and MgO are refractory materials which may be able to withstand higher counterelectrode deposition temperatures. In addition, MgO is a suitable substrate for polycrystalline epitaxial growth of NbN. A study of the growth of NbN on (100) and (111) single-crystal MgO substrates has established the epitaxial relationship.[7,8] The critical temperatures of thin films of NbN (< 50 nm) grown on polycrystalline MgO are systematically higher than for films grown on sapphire or silicon.[8]

The artificial-oxide barriers were formed by depositing a thin metallic overlayer followed by oxidation rather than

depositing the oxide directly by electron-beam evaporation or rf sputtering. The rationale was to achieve a more uniform coverage by the overlayer due to the tendency of one metal to wet another.[9] It was also assumed that the oxide thickness would be more uniform since the oxidation of Al and Mg metal surfaces are self-limiting. The oxidation process should mitigate the effects of any pinholes in the overlayer by forming the native oxide of NbN in the pinholes.

An advantage of an artificial barrier over the native oxide is that it may be useful with other high-T_c superconductors. During the deposition of an rf-sputtered artificial oxide barrier, oxygen from the sputtering target or added to the sputter gas to achieve a stoichiometric insulating layer can oxidize the surface of the base superconductor before the base is covered by a barrier. The usefulness of the composite native-oxide / artificial-oxide barrier which results is limited to superconductors which do not form a degraded surface layer upon oxidation. In particular, the A15 compounds exhibit an atomic segregation at a surface exposed to oxygen.[10,11]

The use of an Ar-O_2 ion beam to oxidize tunnel barriers has been reported by several groups for native-oxide barriers on Nb base electrodes.[12-14] In that case, the ion-beam oxidation was needed to produce low-leakage junctions, with Pb-alloy counterelectrodes, which could not be formed using a thermal oxide of Nb. In this work, however, the thermal oxides of Al and Mg formed excellent tunnel barriers with Pb counterelectrodes. The motivation for using ion-beam oxidation was to test whether the thickness or thickness uniformity of the oxides could be modified.

SAMPLE PREPARATION

With the exception of Pb counterelectrodes evaporated in a separate system, the samples described in this paper were all made by dc magnetron sputtering in one of the chambers of an oil-free 4-chamber deposition and analysis facility described elsewhere.[15] X-ray Photoelectron Spectroscopy (XPS) and Reflection High-Energy Electron Diffraction (RHEED) measurements, ion milling, oxidation in a partial pressure of oxygen, and sputtering were all performed without exposing the sample to air. However, the samples were exposed to air after barrier formation to change aperture masks for counterelectrode cross-strips. There is no a priori reason to believe that similar results would not be obtained if the entire NbN / overlayer (oxide) / NbN trilayer was deposited in situ and a process analogous to the Selective Nb Etching Process (SNEP) was used to define the junctions areas.[16]

The sequence of sputtered layers and oxidation steps was as follows: Si substrate / 5.0 nm Mg / thermal oxidation / 50 to 100 nm NbN / 3.0 to 8.0 nm Al or Mg / thermal oxidation / (ion-beam oxidation) / mask change / NbN. The importance of the MgO underlayer is examined in Ref. 8. The NbN base electrode was deposited at 300°C. The differences between barriers formed by thermal and ion-beam oxidation versus those formed just by thermal oxidation of the Al or Mg overlayer is the primary focus of this paper and will be explained in detail.

The thermal oxidation was performed at room temperature. After transferring the samples in vacuum to an adjacent chamber, 100 millitorr of O_2 was bled into the chamber and pumped out 15 minutes later. Based on XPS measurements of the thickness of the

thermal oxide, no further oxide growth occurred in the subsequent 10 to 15 minute exposure to air while an aperture mask was mounted on the samples for counterelectrode deposition.

The samples which were subjected to ion bombardment were oxidized thermally first. This was done to establish a minimum thickness for the oxide with the intent that exposure to a low energy Ar-5% O_2 ion beam would increase the thickness. The ion milling was done in an Ar + O_2 pressure of 5×10^{-5} torr at an energy of 200 V. The current density was only 100 nA/cm^2 so milling times were up to 1 hour.

Figures 1a and 1b show the Al_{2p} photoelectron peaks from a NbN film with an Al overlayer after thermal oxidation and after ion-beam oxidation, respectively. The peak intensity at a binding energy with a chemical shift characteristic of photoelectrons emitted from Al_2O_3 increased relative to the unshifted metallic Al peak after the ion-beam treatment. However, the Nb_{3d} photoelectron intensity also increased after ion milling. A calculation of layer thicknesses based on peak intensities, the assumption of smooth, uniform layers of Al_2O_3 and Al on top of NbN, and an escape depth of 2.0 nm, showed that the oxide thickness increased by about 0.2 nm. The oxide thickness after thermal oxidation was 2.1 nm and the unoxidized Al thickness was 1.7 nm. After the ion milling, the oxide was 2.3 nm thick, but the unoxidized layer thickness was only 0.5 nm. There was no evidence of any Nb oxides either before or after ion milling.

The absolute accuracy of the thickness measurements depended on the validity of the assumptions listed above. In particular, all thicknesses scaled with the value used for the photoelectron

escape depth. However, the relative accuracy from one measurement of a NbN / Al / Al_2O_3 multilayer sample to another was about 0.1 nm, just small enough leave no doubt that the increase in oxide thickness due to the ion-beam treatment was real.

The effect of the process was similar to that achieved by Greiner who formed native-oxide barriers on Nb and Pb with an argon-oxygen rf-induced plasma which simultaneously oxidized and sputtered the surface.[17] The significant differences were our use of an artificial barrier and of in-situ XPS to determine an end point for the process.

RESULTS AND DISCUSSION

A. Junctions with barriers formed by thermal oxidation

Typical quasiparticle I-V characteristics measured at 4.2K for NbN / thermally oxidized Al or Mg / Pb tunnel junctions are shown in Fig. 2. The Josephson current was not measured because the junctions had large areas, typically 0.005 cm^2, which result in self-shielding. The quality of the junctions, normally expressed in terms of V_m, can be determined by considering the ratio of the current measured at 5 mV to the current measured at 2.5 mV, i(5)/i(2.5). The ratio i(5)/i(2.5) was typically 100 and as large as 110 for oxidized Al barriers and as large as 40 for oxidized Mg barriers. An estimate of V_m at 2.5 mV can be made from the theoretical i_cR_N product.[18] Depending on the thickness of a possible proximity layer, V_m expressed in mV is 0.5 to 1.0 times i(5)/i(2.5). The proximity layer evident as a "knee" at the gap voltage in Fig. 2 is probably due to the 0.5 to 1.0 nm layer of unoxidized Al or Mg detected by XPS. The thickness of the Al

or Mg layer could be decreased to reduce the thickness of the unreacted layer.

A conservative estimate of V_m at 2.5 mV for the junctions with thermally oxidized Al is 60. A comparison of Figures 2a and 2b shows that the junctions with oxidized Mg barriers have a lower V_m due to a smearing of the NbN gap voltage rather than higher leakage at zero bias. Van Vechten and Liebman have proposed that Al and NbN react at the interface to form AlN.[19] While we have no evidence for such a reaction for Al, the same mechanism could explain the excess conductance above the Pb gap for junctions with oxidized Mg barriers. An alternative explanation is that Mg has diffused into the grain boundaries of the NbN to a greater extent than did Al. Kwo et al. have identified the role of grain boundary diffusion even at room temperature for the Nb / Al and Nb / Mg systems.[20] The unoxidized Mg layer protected by the thermal oxide disappeared when a test sample was heated to 300°C leaving only MgO and NbN detectable by XPS. An NbN / Al / Al_2O_3 sample showed no loss of Al at that temperature.

The superconducting gap energy inferred for NbN from Fig. 2(a) was $\Delta_{NbN} = 2.45 \pm .05$ meV. The resistive T_c of the film was 13.3-12.8K. The highest T_c of any polycrystalline films made at 300°C was 15K. The ratio, $2\Delta / k_B T_c$, was typically 4.3.

The resistances of tunnel junctions with artificial barriers formed by thermal oxidation are compared with the resistance of native oxide barriers in Table 1. The resistance of tunnel barriers using the native oxide decreased sharply when carbon was introduced into the NbN by adding methane to the sputter gas, but the resistance of artificial-oxide barriers did not change.[8] The

values reported in Table 1 are for the case where no methane was used. Oxidized Al barriers were approximately one order of magnitude higher in resistance than the native oxide barriers and oxidized MgO was three orders of magnitude higher.

The barrier width and height were calculated by modeling the barrier as a rectangular potential following Simmons and fitting the conductance to a quadratic function of voltage in the range of 0.1 to 0.4 V.[21] The values shown in Table 1 for the fitted barrier width agree with the thickness of the oxide calculated from XPS peak intensities to within 0.7 nm. The higher resistance of the artificial oxide barriers compared with the native oxide was due to a greater barrier height rather than an increased width. The barrier heights and, therefore, the junction resistances for thermal oxides of Al grown on Nb or Nb_3Sn were higher than for the Al_2O_3 barriers on NbN, with barrier heights ranging between 1.0 and 2.0 eV depending on the crystal structure of the oxide.[11]

A number of different counterelectrode materials were deposited on the NbN / Al (thermal oxide) and NbN / Mg (thermal oxide) bilayers. NbN counterelectrodes were formed by reactive sputtering at room temperature both at the same sputtering conditions as the base and at a higher total pressure of the sputtering gas for better thermalization of the sputtered atoms. Nb was sputtered and evaporated with the bilayers held at room temperature, and evaporated with the bilayers cooled to 77K. All of these attempts resulted in junctions which were shorts up to currents of 100 to 200 mA at which point the samples heated beyond their transition temperature. The variety of physical

deposition parameters which were studied without altering the outcome suggested that there was a chemical reduction of the barriers, probably at the thinnest spots, which shorted the electrodes.

B. Junctions with barriers formed by ion-beam oxidation

The I-V characteristics of reference junctions, that is, junctions with Pb counterelectrodes, for the ion-beam oxidized barriers are shown in Fig. 3. For ion-beam oxidized Al, $i(5)/i(2.5) = 90$ at 4.2K, so the leakage was negligibly higher than for junctions with thermal oxide barriers. The ion-beam oxidized Mg barriers, however, had high leakage currents and $i(5)/i(2.5) = 6$. RHEED patterns showed that the thermal oxides of both Al and Mg were composed of randomly-oriented polycrystalline material. The crystallinity of the oxidized metallic overlayers was in contrast to the result of Shoji et al. who found that much thinner layers of rf-sputtered MgO were amorphous.[1] After ion-beam oxidation, the sharp ring patterns became more diffuse although several rings were still resolved. An effect of the disorder introduced into the polycrystalline Al_2O_3 by ion-beam oxidation was an increase in the junction resistance by more than an order of magnitude. An order of magnitude increase in resistance might appear to be consistent with the increase in oxide thickness of 0.2 nm observed by XPS, but the increase occurred because both the average barrier height and width increased slightly (Table 1).

Figure 4 shows the I-V curve of a NbN / ion-beam oxidized Al bilayer with a NbN counterelectrode deposited at room tempera-

ture. The ratio i(5)/i(2.5) = 17. The analogous junctions with ion-beam oxidized Mg barriers had i(5)/i(2.5) = 3 with most of the subgap conductance due to a spread in the gap voltage rather than leakage at zero bias.

The barrier widths inferred from the curvature of the I-V characteristics and the oxide thicknesses measured directly by XPS were much greater than the thickness of 0.7 nm of rf-sputtered MgO used by Shoji et al.[1] The product of the junction resistance and area was between $1x10^{-6}$ and $5x10^{-6}$ Ω-cm^2 for junctions made by Shoji et al., three orders of magnitude lower than the values in Table 1 obtained with ion-beam oxidation, and consistent with the difference in thickness.

C. NbN counterelectrode deposition on oxide barriers

Although junctions such as the one shown in Fig. 4 were sufficient to demonstrate the properties of the ion-beam oxidized barriers, the gap voltage of the counterelectrode was only about half of the gap voltage of the base electrode. In this section, we consider the limitations of the value of the gap energy of NbN counterelectrodes grown on polycrystalline MgO. Since it has a B1 structure, MgO should be a more favorable barrier than Al_2O_3 for high gap values of counterelectrodes. Some limit below bulk values of the energy gap can be expected due to low-temperature deposition and the short coherence length of NbN, 4 to 5 nm.

The tunnel junctions shown in Fig. 5 were made with Pb counterelectrodes on four different types of NbN films to evaluate the homogeneity of the films rather than the properties of the barrier. All four NbN films were deposited on a 20 nm

underlayer of MgO. The junction in Fig. 5a was made on a 50 nm thick film deposited at room temperature. The sharp gap, 0.2 meV wide, indicated that the NbN film was homogeneous. Comparison with the energy gap of a film of the same thickness grown at 300°C (Fig. 5b), shows that the gap voltage can be raised by 0.6 mV with the 300°C substrate temperature. Preliminary measurements on tunnel junctions with a NbN counterelectrode deposited at 300°C showed that the ion-beam oxidized barriers remain intact but the resistance of the junctions were too low to measure the full I-V curve.

The tunnel junction formed on a 7.5 nm film, which is also shown in Fig. 5b, had a broader gap, 0.4 meV, and a lower gap, 1.9 meV, than the junctions on the 15 nm or 50 nm films. The thickness approximates the first 1 to 2 coherence lengths of a counterelectrode deposited at 300°C on an MgO barrier so the gap energy represents an upper limit to the energy gap of a NbN counterelectrode unless higher temperatures or new sputtering parameters are used. The junction characteristics in Fig. 5b show that the gap voltage does not continue to increase for films thicker than 15 nm.

CONCLUSIONS

The effectiveness of either thermally oxidized or ion-beam oxidized Al or Mg barriers has been demonstrated for NbN-based tunnel junctions with Pb counterelectrodes. The deposition of refractory counterelectrodes on the thermal oxides resulted in shorted tunnel barriers.

Ion-beam oxidation has enabled the use of NbN coun-

terelectrodes by increasing the oxide thickness and perhaps forming an oxide of more uniform thickness. The junctions with oxidized Al barriers have lower subgap conductances than comparable MgO barriers for thermal oxidation or ion-beam oxidation, and with either Pb or NbN counterelectrodes, probably due to the greater tendency of unoxidized Mg to diffuse into the base electrode. Nevertheless, polycrystalline MgO barriers have the advantage of providing a suitable substrate for the epitaxial growth of a NbN counterelectrode.

ACKNOWLEDGMENTS

The authors would like to thank H. C. Pohl for his assistance with thin film deposition and characterization.

The artificial oxide barriers, used with superconductors other than NbN, were developed in part under Office of Naval Research contract No. N00014-82-C-0617.

REFERENCES

a) Supported in part by Air Force Office of Scientific Research Contract No. F49620-83-C-0035.

1. A. Shoji, M. Aoyagi, S. Kosaka, F. Shinoki, and H. Hayakawa, Appl. Phys. Lett. 46(11), 1098 (1985).

2. A. Shoji, S. Kosaka, F. Shinoki, M. Aoyaki, and H. Hayakawa, IEEE Trans. Mag. MAG-19(3), 827 (1983).

3. E. J. Cukauskas, W. L. Carter, S. B. Qadri, and E. F. Skelton, IEEE Trans. Mag. MAG-21(2), 505 (1985).

4. Masaru Igarashi, Makoto Hikita, and Koji Takei, in Advances in Cryogenic Engineering - Materials, Vol. 30, edited by A. F. Clark and R. P. Reed (Plenum, New York, 1984), p. 535.

5. J. C. Villegier, L. Vieux-Rochaz, M. Goniche, P. Renard, and M. Vabre, IEEE Trans. Mag. MAG-21(2), 498 (1985).

. F. Shinoki, A. Shoji, S. Kosaka, S. Takada, and H. Hayakawa, Appl. Phys. Lett. 38(4), 285 (1981).

7. G. Oya and Y. Onodera, J. Appl. Phys. 45(3), 1389 (1974).

8. J. R. Gavaler, J. Talvacchio, and A. I. Braginski, to be published in Advances in Cryogenic Engineering - Materials, Vol. 32, edited by A. F. Clark and R. P. Reed (Plenum, New York, 1986).

9. J. Kwo, G. D. Wertheim, M. Gurvitch, and D. N. E. Buchanan, Appl. Phys. Lett. 40(8), 675 (1982).

10. H. Ihara, Y. Kimura, H. Okumura, K. Senzaki, and S. Gonda, in Adv. in Cryogenic Engineering - Materials, Vol. 30, edited by A. F. Clark and R. P. Reed (Plenum, New York, 1984), p. 589.

11. J. Talvacchio, A. I. Braginski, M. A. Janocko, and S. J. Bending, IEEE Trans. Mag. MAG-21(2), 521 (1985).

12. A. W. Kleinsasser and R. A. Buhrman, Appl. Phys. Lett. 37(9), 841 (1980).

13. R. Herwig, Electron. Lett. 16, 850 (1980).

14. S. S. Pei and R. B. van Dover, Appl. Phys. Lett. 44(7), 703 (1984).

15. J. Talvacchio, M. A. Janocko, A. I. Braginski, and J. R. Gavaler, to be published in Advances in Cryogenic Engineering - Materials, Vol. 32, edited by A. F. Clark and R. P. Reed (Plenum, New York, 1986).

16. M. Gurvitch, M. A. Washington, H. A. Huggins, and J. M. Rowell, IEEE Trans. Mag. MAG-19(3), 791 (1983).

17. J. H. Greiner, J. Appl. Phys. 45(1), 32 (1974).

18. M. Gurvitch and J. Kwo, in Advances in Cryogenic Engineering - Materials, Vol. 30, edited by A. F. Clark and R. P. Reed (Plenum, New York, 1984), p. 509.

19. D. Van Vechten and J. F. Liebman, J. Vac Sci. Techno. A 3 (1985).

20. J. Kwo, G. K. Wertheim, M. Gurvitch, and D. N. E. Buchanan,

IEEE Trans. Mag. MAG-19(3), 795 (1983).

21. J. G. Simmons, J. Appl. Phys. 34, 238 (1963).

Table 1

Tunnel junction resistance and barrier thickness.
The ratio i(5)/i(2.5) is an indicator of junction quality.

Barrier Material/ Formation	Resistance (Ω-cm^2)	Barrier Thickness by XPS (nm)	Fit to Simmons' Model		i(5)/ i(2.5)
			Barrier Thickness	Barrier Height (eV)	
Pb Counterelectrode					
Al_2O_3/Thermal	0.001 to 0.01	2.1	1.8	0.8	100
MgO/Thermal	0.1 to 1	2.9	2.2	1.0	40
Nb_2O_5/Thermal	0.0001 to 0.001	1.9	2.6	0.25	110
Al_2O_3/Ion Beam	0.1	2.3	1.9	1.0	90
MgO/Ion Beam	0.1	4.0	--	--	6
NbN Counterelectrode					
Al_2O_3/Ion Beam	0.001 to 0.01	2.3	2.4	0.4	17
MgO/Ion Beam	0.001 to 0.01	4.0	2.3	0.5	3

FIGURE CAPTIONS

Fig. 1 The normalized XPS spectra for Al_{2p} photoelectrons (a) after thermal oxidation and (b) after ion-beam oxidation showing the relative decrease of Al and increase of Al_2O_3 due to the ion-beam treatment.

Fig. 2 Typical quasiparticle I-V characteristics for NbN / thermally oxidized overlayer / Pb tunnel junctions. Fig. 2(a) is for an oxidized Al overlayer and (b) is for an oxidized Mg overlayer.

Fig. 3 Typical I-V curves for NbN / ion-beam oxidized overlayer / Pb tunnel junctions. Fig. 3(a) shows the characteristics for an Al overlayer and Fig. 3(b) shows the characteristics for an Mg overlayer.

Fig. 4 The quasiparticle I-V characteristics of a NbN / ion-beam oxidized Al / NbN tunnel junction. The NbN counterelectrode was deposited at room temperature.

Fig. 5 The quasiparticle I-V curves for tunnel junctions with a thin NbN base electrode deposited on MgO at (a) room temperature and (b) 300°C. The junction characteristics show that the NbN films deposited at 300°C have a higher gap voltage than films grown at room temperature. Films with a thickness of 7.5 nm have a lower and broader gap voltage than comparable films 15 nm or 50 nm thick.

Curve 750017-A

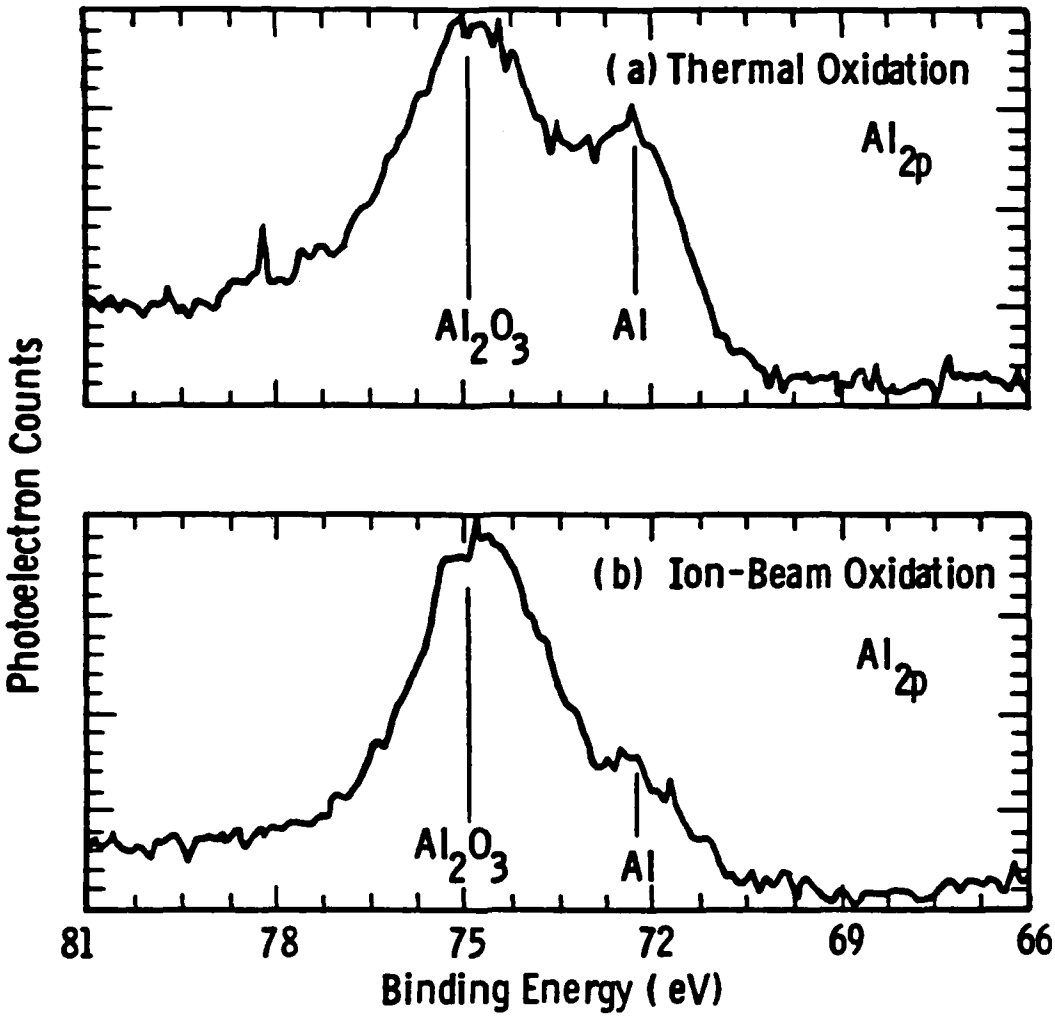

. Talvacchio
.t.d. - jd 6-20-85

Fig. 1

Curve 750017

Curve 750016-A

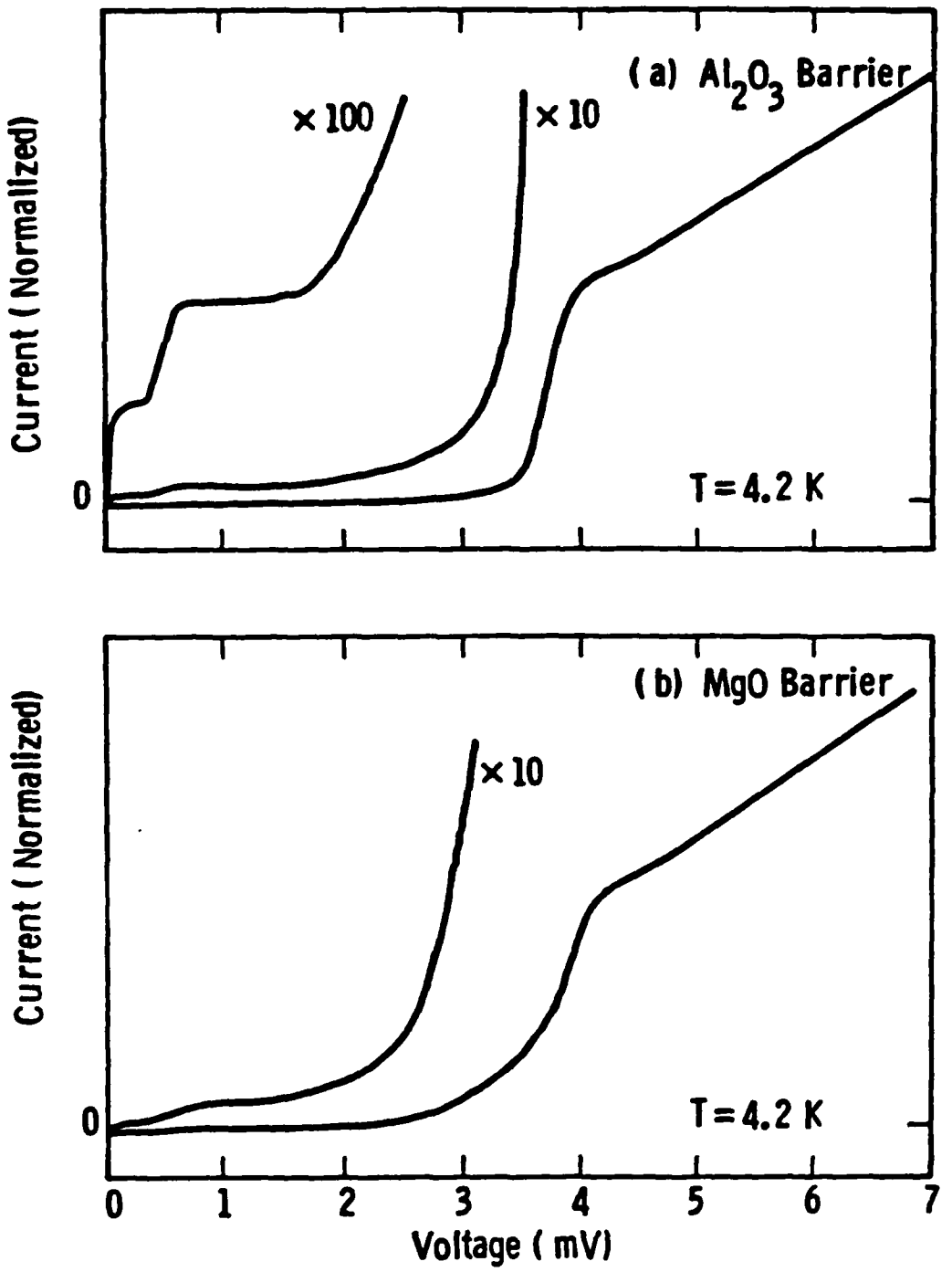

J. Talvacchio
c.t.d.- jd 6-20-85

Fig. 2

Curve 7500

Curve 750013-A

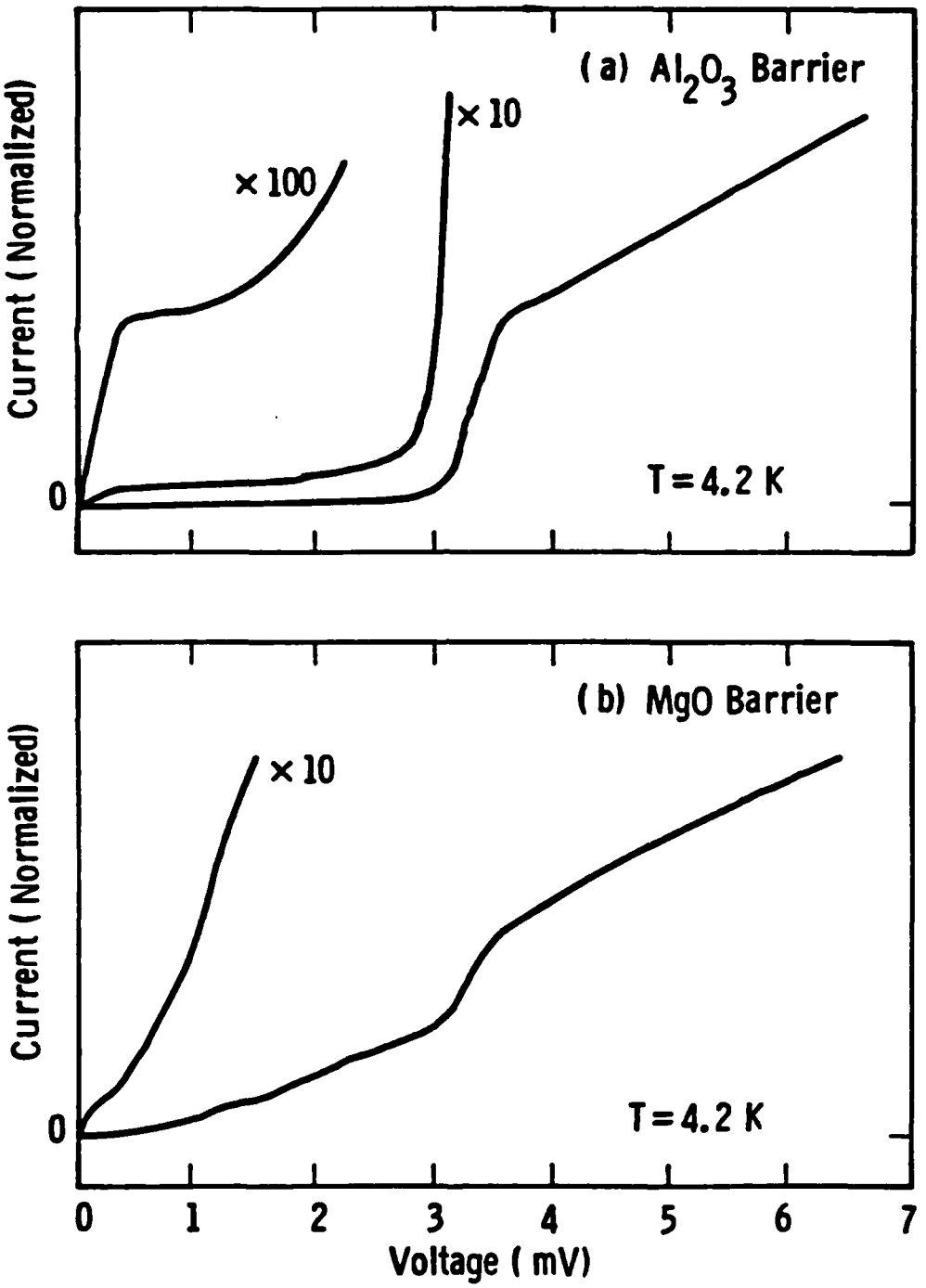

J. Talvacchio
c.t.d. - jd 6-20-85

Fig. 3

Curve 750013

Curve 750014-A

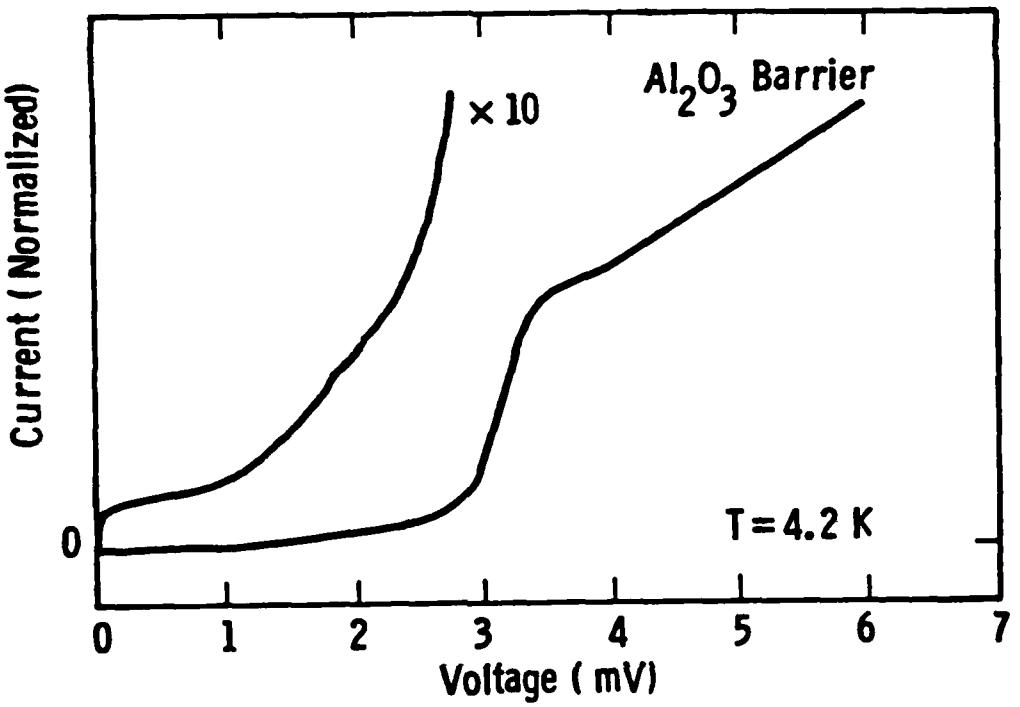

J. Talvacchio
c.t.d. - jd 6-20-85

Fig. 4

Curve 75001

Curve 750015-A

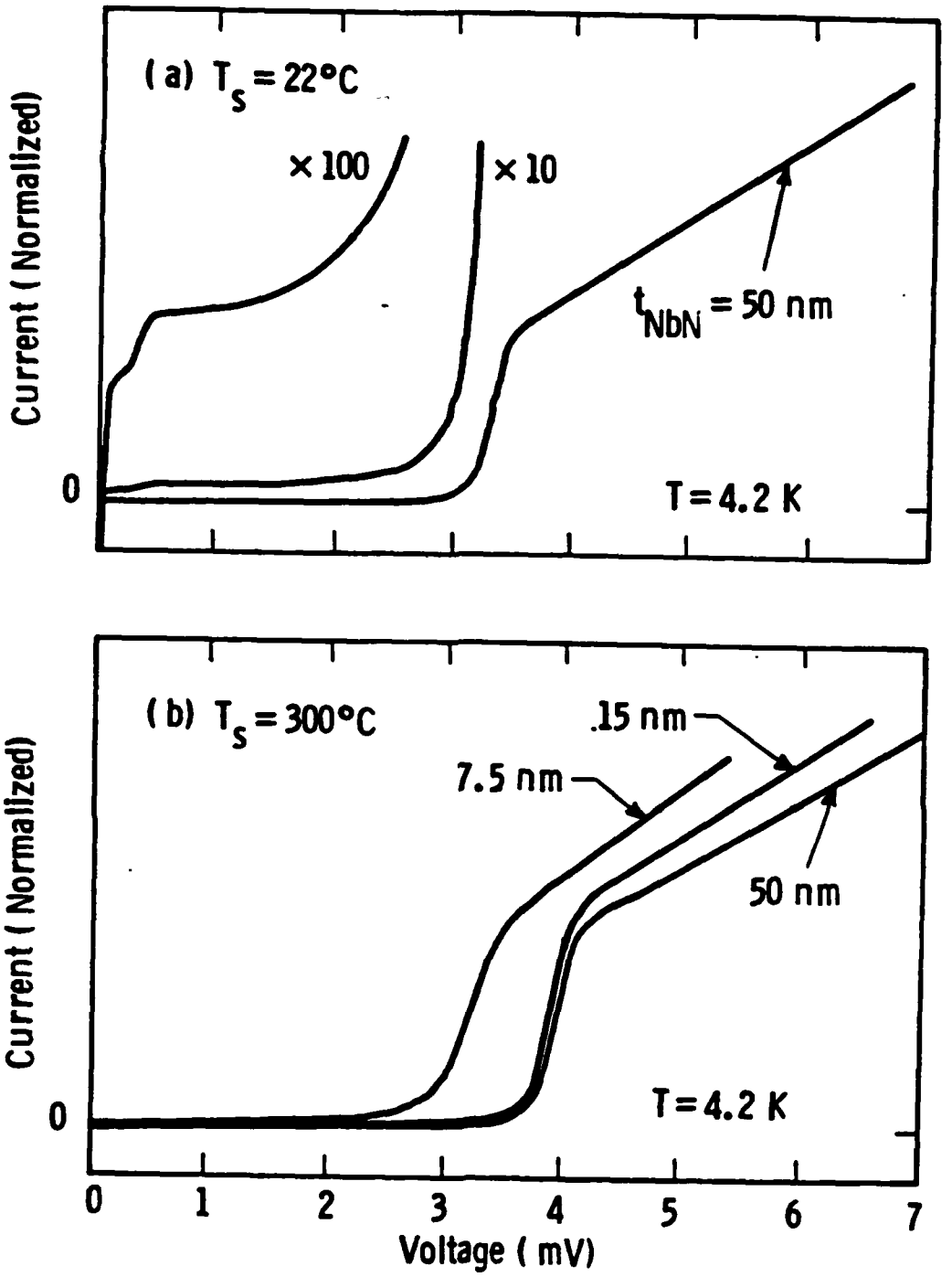

J. Talvacchio
c.t.d.- jd 6-20-85

Fig. 5

Curve 750015

END

FILMED

2-86

DTIC